1-1-2009

Kinematic properties of early-type galaxy haloes using planetary nebulae

L. Coccato
Max-Plank-Institut für Extraterrestrische Physik

O. Gerhard
Max-Plank-Institut für Extraterrestrische Physik

M. Arnaboldi
European Southern Observatory

P. Das
Max-Plank-Institut für Extraterrestrische Physik

N. G. Douglas
Kapteyn Astronomical Institute

See next page for additional authors

Recommended Citation

L. Coccato, O. Gerhard, M. Arnaboldi, P. Das, N. G. Douglas, K. Kuijken, M. R. Merrifield, N. R. Napolitano, Aaron J. Romanowsky, E. Noordermeer, M. Capaccioli, A. Cortesi, F. De Lorenzi, and K. C. Freeman. "Kinematic properties of early-type galaxy haloes using planetary nebulae" *Monthly Notices of the Royal Astronomical Society* (2009): 1249-1283. https://doi.org/10.1111/j.1365-2966.2009.14417.x

Mon. Not. R. Astron. Soc. **394,** 1249–1283 (2009) doi:10.1111/j.1365-2966.2009.14417.x

Kinematic properties of early-type galaxy haloes using planetary nebulae⋆

L. Coccato,[1]† O. Gerhard,[1] M. Arnaboldi,[2,3] P. Das,[1] N. G. Douglas,[4] K. Kuijken,[5] M. R. Merrifield,[6] N. R. Napolitano,[7] E. Noordermeer,[6] A. J. Romanowsky,[8,9] M. Capaccioli,[10,11] A. Cortesi,[6] F. De Lorenzi[1] and K. C. Freeman[12]

[1]*Max-Plank-Institut für Extraterrestrische Physik, Giessenbachstraße, D-85741 Garching bei München, Germany*
[2]*European Southern Observatory, Karl-Schwarzschild-Straße 2, D-85748 Garching bei München, Germany*
[3]*INAF, Osservatorio Astronomico di Pino Torinese, I-10025 Pino Torinese, Italy*
[4]*Kapteyn Astronomical Institute, Postbus 800, 9700 AV Groningen, the Netherlands*
[5]*Leiden Observatory, Leiden University, PO Box 9513, 2300RA Leiden, the Netherlands*
[6]*School of Physics and Astronomy, University of Nottingham, University Park, Nottingham NG7 2RD*
[7]*INAF-Observatory of Capodimonte, Salita Moiariello, 16, 80131, Naples, Italy*
[8]*UCO/Lick Observatory, University of California, Santa Cruz, CA 95064, USA*
[9]*Departamento de Física, Universidad de Concepción, Casilla 160-C, Concepción, Chile*
[10]*Dipartimento di Scienze Fisiche, Universitá Federico II, Via Cinthia, 80126, Naples, Italy*
[11]*INAF-VSTceN, Salita Moiariello, 16, 80131, Naples, Italy*
[12]*Research School of Astronomy & Astrophysics, ANU, Canberra, Australia*

Accepted 2008 December 18. Received 2008 December 18; in original form 2008 September 15

ABSTRACT

We present new planetary nebulae (PNe) positions, radial velocities and magnitudes for six early-type galaxies obtained with the Planetary Nebulae Spectrograph (PNS), along with derived two-dimensional velocity and velocity dispersion fields, and the α parameters (i.e. the number of PNe per unit luminosity). We also present new deep absorption-line long-slit kinematics for three galaxies in the sample, obtained with the FOcal Reducer and low dispersion Spectrograph (FORS2) at the Very Large Telescope (VLT).

We extend this study to include additional 10 early-type galaxies with PNe radial velocity measurements available from the literature, including previous PNS studies, in order to obtain a broader description of the outer-halo kinematics in early-type galaxies. These data extend the information derived from stellar absorption-line kinematics to typically several and up to 8 effective radii.

The combination of photometry, absorption-line and PNe kinematics shows (i) a good agreement between the PNe number density distribution and the stellar surface brightness in the region where the two data sets overlap; (ii) a good agreement between PNe and absorption-line kinematics; (iii) that the mean rms velocity profiles fall into two groups, with part of the galaxies characterized by slowly decreasing profiles and the remainder having steeply falling profiles; (iv) a larger variety of velocity dispersion radial profiles; (v) that twists and misalignments in the velocity fields are more frequent at large radii, including some fast rotator galaxies; (vi) that outer haloes are characterized by more complex radial profiles of the specific angular momentum-related λ_R parameter than observed within 1 R_e; (vii) that many objects are more rotationally dominated at large radii than in their central parts and (viii) that the halo kinematics are correlated with other galaxy properties, such as total B band and X-ray

⋆Based in part on observations made with the William Herschel Telescope operated by the Isaac Newton Group in the Spanish Observatorio del Roque de los Muchachos on the island of La Palma, of the Instituto de Astrofísica de Canarias, and on observations collected at the European Southern Observatory, Chile, Program: 76.B-0788(A).

†E-mail: lcoccato@mpe.mpg.de

luminosity, isophotal shape, total stellar mass, V/σ and α parameter, with a clear separation between fast and slow rotators.

Key words: galaxies: elliptical and lenticular, cD – galaxies: general – galaxies: haloes – galaxies: kinematics and dynamics.

1 INTRODUCTION

The dynamics of galaxies provide fundamental information on their origin and evolution. Our knowledge of the kinematics and dynamics of early-type galaxies is mainly based on measurements of the first four moments of the line-of-sight velocity distribution (LOSVD) from stellar absorption lines. These measurements are generally confined to within 1–2 effective radii (R_e) and can be obtained with long slits or integral-field units. Detailed LOSVD measurements for early-type galaxies (e.g. Bender, Saglia & Gerhard 1994; Fisher 1997; Pinkney et al. 2003; Emsellem et al. 2004) have provided us with a general picture of their dynamics. The higher-order moments are needed to obtain good constraints on the anisotropy and mass distribution (Gerhard 1993; Merritt 1993). Most of the studied objects appear to be isotropic or slightly radially anisotropic systems (Kronawitter et al. 2000; Cappellari et al. 2006). Some galaxies have revealed the presence of cold stellar discs whose kinematics stand out only after 1–1.5 R_e (Rix, Carollo & Freeman 1999).

Kinematics of early-type galaxies are related to their isophotal shape. Deviations of the isophotes from a perfect ellipse are parametrized by the amplitude a_4 of the $\cos 4\theta$ term in a Fourier expansion of the isophote radius in polar coordinates (e.g. Bender, Doebereiner & Moellenhoff 1988). Observational evidence (e.g. Bender 1988; Kormendy & Djorgovski 1989) implies that *discy* ellipticals ($a_4 > 0$) have significant rotation with $V/\sigma \geq 1$ and may generally be axisymmetric; *boxy* ellipticals ($a_4 < 0$) exhibit no rotation, have a range of values of V/σ including strongly anisotropic systems ($V/\sigma \ll 1$), may be triaxial and are in general more massive than discy ellipticals. These relations between isophotal shape and galaxy kinematics motivated Kormendy & Bender (1996) to revise the Hubble classification scheme for early-type galaxies using the a_4 parameter, which is related to intrinsic galaxy properties rather than the apparent ellipticity, which is related to the galaxy's orientation on the sky.

A related modification to this scheme has been recently proposed by Emsellem et al. (2007), taking advantage of the advent of integral-field units. These allow for two-dimensional maps of the LOSVD moments typically out to $1R_e$ (Emsellem et al. 2004). Early-type galaxies have been divided into two distinct classes: *slow* and *fast* rotators, according to the stellar angular momentum they possess per unit of mass. The two classes have different dynamical properties: slow rotators appear to be more massive systems, nearly round with a significant kinematic misalignment, implying a moderate degree of triaxiality, and span a moderately large range of anisotropies; fast rotators appear to be rather flattened systems, without significant kinematic misalignments, nearly axisymmetric and span a larger range of anisotropies (Cappellari et al. 2007).

In parallel, the arrival of large photometric surveys such as the Sloan Digital Sky Survey has consolidated findings of a bimodal colour distribution in local galaxies (e.g. Baldry et al. 2006), differentiating between a *blue cloud* of mostly star-forming spiral galaxies and a *red sequence* of mostly non-star-forming early-type galaxies.

Some of the main aims of galaxy formation studies are to understand the mechanisms that allow galaxies to evolve from the blue cloud to the red sequence, and to differentiate between processes that form early-type galaxies that are fast or slow rotators. Numerical simulations suggest that red-sequence galaxies are formed by mergers of galaxies in the blue cloud, followed by a quenching of the star formation (e.g. Cattaneo et al. 2006; Faber et al. 2007; Kang, van den Bosch & Pasquali 2007; Romeo et al. 2008). The less-luminous fast rotators with discy isophotes are preferentially formed through a series of minor mergers with less massive companions. On the other hand, the more-luminous slow rotators with boxy isophotes are thought to form through a violent major merger between galaxies of similar mass (e.g. Naab, Burkert & Hernquist 1999; Naab & Burkert 2003), or through multiple or hierarchical mergers (Weil & Hernquist 1996; Burkert et al. 2008).

These formation mechanisms are complicated further by the presence or absence of gas during the merger event, which plays a fundamental role in the final kinematic structure of the merger remnant (e.g. Barnes & Hernquist 1996; Naab, Jesseit & Burkert 2006; Ciotti, Lanzoni & Volonteri 2007). Mergers producing red-sequence galaxies dominated by rotation appear to be gas-rich (*wet*), while gas-poor (*dry*) mergers produce red-sequence galaxies dominated by random motions (e.g. Bournaud, Jog & Combes 2005; Cox et al. 2006; Naab et al. 2006).

However, observations show that many of the most massive early-type galaxies were already in place by $z \sim 2$ (van Dokkum et al. 2004; Treu et al. 2005), and the evolution of the galaxy luminosity function since redshifts of $z \sim 1$ argues against a significant contribution of recent dissipationless dry mergers to the formation of the most massive early-type galaxies in the red sequence (Scarlata et al. 2007). Therefore, it is clear that the processes forming elliptical galaxies are not yet completely understood.

Numerical simulations of galaxy formation in a cosmological context predict particular radial profiles for the total and dark matter distributions (e.g. Dekel et al. 2005; Naab et al. 2007), for the V/σ ratio (e.g. Abadi, Navarro & Steinmetz 2006), the angular momentum, orbital distribution and isophotal shape (e.g. Naab et al. 2006), depending on which cosmology or merger type is assumed. The evaluation of these quantities from observations through dynamical models is fundamental to probe galaxy formation theories, numerical simulations and cosmological scenarios. Unfortunately, the picture is complicated by the presence of unknown variables such as the three-dimensional shape of the galaxy and the orbital distribution. Therefore, only detailed information on the LOSVD out to large radii can help to disentangle possible scenarios in galaxy formation.

In spiral galaxies (or generally in gas-rich systems), the distribution of dark matter can be determined by measuring the kinematics of neutral or ionized gas, which can be easily observed at large distances from the centre. This allowed, for instance, the discovery of the presence of dark matter in galaxies in the 1970s. Only a few early-type galaxies contain large gas rings with which the mass distribution can be traced out to several R_e (e.g. Bertola et al. 1993;

Oosterloo et al. 2002; Weijmans et al. 2008). In the large majority of ellipticals or lenticulars, the mass determination is more difficult because absorption lines from a stellar spectrum can be measured with a sufficient signal-to-noise ratio only up to 2 effective radii. Studies based on integrated light spectra provide evidence for dark matter only in a fraction of ellipticals, with the inferred mass profiles being nearly isothermal to the limit of the data and the dark matter contributing ∼10–50 per cent of the mass within R_e (e.g. Kronawitter et al. 2000; Gerhard et al. 2001; Thomas et al. 2007). For other systems, absorption-line data are not extended enough to provide conclusive evidence for dark matter (see e.g. the detailed recent analysis of De Lorenzi et al. 2008, 2009). The apparent dichotomy may be related to the fact that the logarithmic gradient of the mass-to-light ratio correlates with luminosity (Napolitano et al. 2005), suggesting a link between the structural parameters and the total mass of ellipticals.

In order to extend the kinematic information for early-type galaxies to larger radii, alternative kinematic tracers have been identified to compensate for the rapid fall-off in the stellar light at radii larger than $2R_e$, such as globular clusters and planetary nebulae (PNe). In particular, a lot of effort has been focused on PNe in the last decade: they are generally believed to trace the main stellar population of elliptical galaxies, and their relative bright [O III] emission line allows them to be easily detected at large radii from the centre, making them an ideal tool for kinematic studies.

A dedicated instrument was installed at the William Herschel Telescope: the Planetary Nebulae Spectrograph (PNS; Douglas et al. 2002). In the last seven years, our team has undertaken a long-term observational campaign aimed at measuring the kinematics of a selected sample of ellipticals and S0s, with the principal aim to quantify the dark matter content in those systems. An initial sample of round (E0–E2) and bright ($B \leq 12.5$) galaxies has been selected, and later enlarged to include more flattened objects (≤E5) and S0s. A series of papers has been published, presenting the initial results of the PNS survey on early-type galaxies and their dynamical analysis (Romanowsky et al. 2003; Douglas et al. 2007; Noordermeer et al. 2008; De Lorenzi et al. 2009; Napolitano et al. 2009).

To provide a general overview of the outer kinematics ($R \geq 1.5$–$2R_e$) of early-type galaxies and fundamental constraints on formation scenarios, we have used the literature to collect all the existing PNe kinematics in ellipticals and S0s, amounting to 10 objects in total. This includes galaxies previously observed with the PNS as well as galaxies observed by other authors using different telescopes and techniques.

In this paper, we also present new PNe measurements for six galaxies obtained with the PNS. We will refer to them as *sample A*, while we will divide the other 10 galaxies from the literature into *sample B* (six galaxies with more than 80 PNe radial velocity measurements) and *sample C* (four galaxies with less than 80 PNe radial velocity measurements) in the rest of the paper. The total sample consists of 16 galaxies, and their principal characteristics are summarized in Table 1. In Section 2, we present the PNS observations. In Section 3, we compare the PNe spatial distribution to the stellar surface brightness. In Section 4, the smoothed two-dimensional velocity and velocity dispersion fields are derived and compared to the corresponding stellar kinematic data. In Section 5,

Table 1. Sample galaxies.

Name	Type	D (Mpc)	cz (km s^{-1})	B_T	R_e (arcsec)	PA (°)	N_{PNe}	R_{LAST} (arcmin)	Log L_X Log (erg s^{-1})	Reference
(1)	(2)	(3)	(4)	(5)	(6)	(7)	(8)	(9)	(10)	(11)
NGC 821*	E6	22.4 ± 1.8	1735	11.72	39	25	123(4)	6.8	40.33	
NGC 3377*	E5	10.4 ± 0.4	665	11.07	41	35	151(3)	10.0	<39.60	
NGC 3608*	E2	21.3 ± 1.4	1253	11.69	40	75	87(5)	6.8	40.01	
NGC 4374*	E1	17.1 ± 0.9	1060	10.01	53	135	450(7)	6.9	40.83	
NGC 4564*	E6	13.9 ± 1.1	1142	12.05	22	47	49(1)	7.5	<39.85	
NGC 5846*	E0	23.1 ± 2.1	1714	10.91	53	70	123(1)	6.0	41.65	
NGC 1023*	S0	10.6 ± 0.8	637	10.08	46	87	183(20)	10.8	39.6	Noordermeer et al. (2008)
NGC 1344	E5	18.4 ± 2.5	1169	11.24	46	165	194(3)	6.7	<39.48	Teodorescu et al. (2005)
NGC 3379*	E1	9.8 ± 0.5	889	10.18	47	70	186(5)	7.2	39.54	Douglas et al. (2007)
NGC 4494*	E1	15.8 ± 0.8	1344	10.55	53	0	255(12)	7.6	40.10	Napolitano et al. (2009)
NGC 4697	E6	10.9 ± 0.7	1236	10.07	66	70	535(0)	6.6	40.12	Méndez et al. (2001)
NGC 5128	S0	4.2 ± 0.3	547	7.30	255	35	780	8.4	40.10	Peng et al. (2004)
NGC 1316	S0	20.0 ± 1.6	1793	9.40	109	50	43	4.3	40.87	Arnaboldi et al. (1998)
NGC 1399	E1	18.5 ± 1.4	1447	10.44	42	110	37	8.3	41.63	Saglia et al. (2000)
NGC 3384	S0	10.8 ± 0.7	704	10.75	50	53	68	2.4	<39.52	Tremblay et al. (1995)
NGC 4406	E3	16.0 ± 1.0	-244	9.74	91	130	16	4.0	42.05	Arnaboldi et al. (1996)

Notes. Col. 1: name of galaxy. Galaxies marked with * have been observed with the PNS. Col. 2: morphological type of galaxy according to the NED. Col. 3: distance of galaxy from Tonry et al. (2001) derived using the surface brightness fluctuations method. Distance moduli are shifted by −0.16 mag to take into account the new Cepheid zero-point of Freedman et al. (2001) as done by Jensen et al. (2003). Col. 4: galaxies' heliocentric systemic velocity listed in NED. Col. 5: total B magnitude corrected for extinction and redshift listed in RC3. Col. 6: effective radii given by Blakeslee et al. (2001). Col. 7: galaxy photometric position angle as given by RC3, except for NGC 1399 (Saglia et al. 2000), NGC 3379 (Capaccioli et al. 1990) and NGC 4494 (Napolitano et al. 2009). Col. 8: total number of PNe with measured radial velocities. In parentheses, we give the number of sources excluded by the friendless algorithm (not included in the listed total PNe number), for those galaxies for which we applied our adaptive kernel smoothing technique (see Section 4.2). Col. 9: maximum distance of the PNe detections from the galaxy centre. Col. 10: logarithmic X-ray bolometric luminosity according to O'Sullivan, Forbes & Ponman (2001), except for NGC 1023, whose X-ray luminosity was converted from 0.5–2 keV measurements of David et al. (2006) to bolometric luminosity following the prescription of O'Sullivan et al. (2001). Col. 11: reference for the PNe data. Galaxies with new PNe catalogues presented in this paper (*sample A*) are grouped on the top of the table. Galaxies whose PNe data are available in the literature are divided in *sample B* (with more than 80 PNe radial velocities, central part of the table) and *sample C* (with less than 80 PNe radial velocity measurements, lower part of the table).

Table 2. PNe catalogue for galaxies in *Sample A*.

Name (PNS-EPN) (1)	RA (hh:mm:ss) (2)	Dec. (deg:mm:ss) (3)	$V_\odot$ (km s^{-1}) (4)	m_{5007} (mag) (5)
NGC 821-001	02:08:01.6	+10:58:52.4	1670 ± 21	28.8
NGC 821-002	02:08:05.5	+10:58:45.2	1703 ± 21	28.1
NGC 821-003	02:08:06.7	+11:02:03.4	1742 ± 20	27.7
NGC 821-004	02:08:10.4	+11:00:00.4	1725 ± 21	28.6
NGC 821-005	02:08:13.0	+10:58:22.4	1823 ± 22	29.7
NGC 821-006	02:08:14.0	+10:57:13.7	1781 ± 21	28.7
NGC 821-007	02:08:15.8	+10:59:22.3	1669 ± 21	28.3
NGC 821-008	02:08:16.1	+10:59:20.0	1832 ± 21	28.3
NGC 821-009	02:08:16.2	+10:56:31.0	1629 ± 21	28.7
NGC 821-010	02:08:16.4	+11:00:17.5	1681 ± 21	28.8
..				
NGC 5846-124	15:06:46.9	+01:34:32.2	1971 ± 22	28.1

Notes. This is a sample: the complete table is published as Supporting Information in the online version of this article. PNe catalogues are also available at http://www.strw.leidenuniv.nl/pns. Col. 1: PNe name according to the IAU standards (PNS-EPN-<GALAXY NAME>-<SEQUENTIAL NUMBER>). Col. 2: right ascension (J2000). Col. 3: declination (J2000). Col. 4: radial velocity in the heliocentric reference system. Col. 5: apparent m_{5007} magnitude. Magnitudes have an error of ±0.4 mag.

we provide notes on the individual galaxies. In Section 6, we discuss the general kinematic properties of early-type galaxies at large radii obtained from the combination of stellar and PNe kinematics for all the galaxies in the sample, and we close with a summary of our work in Section 7.

2 OBSERVATIONS AND DATA REDUCTION

For galaxies in *sample A*, we present new PNe positions, radial velocities and magnitudes, obtained as part of the PNS elliptical galaxy survey. For these *sample A* galaxies, data reduction, PNe identification, radial velocity and magnitude measurements are performed using the procedures described in Douglas et al. (2007). Catalogues with positions, velocities and magnitudes of PNe in galaxies of *sample A* are shown in Table 2. Heliocentric systemic velocities derived from PNe are in agreement within the error bars with the values tabulated in either de Vaucouleurs et al. (1991, hereafter RC3) or NASA/IPAC Extragalactic Data base (NED) catalogues. Instrumental magnitudes are shifted in order to match the bright cut-off of the luminosity function with the expected apparent magnitude $m' = M^*_{5007} + 25 + 5 \log D$, where D is the distance in Mpc given in Table 1 and $M^*_{5007} = -4.48$ is the absolute magnitude of the cut-off according to Ciardullo et al. (1989b).

The number of PNe detected using the PNS is over 100 for the majority of the galaxies, with a remarkable number of 457 objects for NGC 4374. This is a major improvement when compared to the results of previous techniques and instruments (typically <50 detections). In the following sections, we use only PNe whose velocities are within 3σ of the mean velocity of their neighbours, according to the 'friendless algorithm' described in Merrett et al. (2006).

3 PNE SPATIAL DISTRIBUTION

Fig. 1 shows the spatial distribution of the PNe in *sample A* galaxies. For the PNe positions in the galaxies of *samples B* and *C*, we refer to the references listed in Table 1.

The first property of the PNe spatial distribution we would like to investigate is whether or not the number density of the PNe follows the stellar surface brightness. This has already been tested for many galaxies in the sample (see reference list in Table 1), finding generally a good agreement between the surface brightness and PNe counts.[1]

From Fig. 1, we see that to a first approximation the two-dimensional distribution of PNe is symmetric. NGC 821 and 4564 are possible exceptions in that they may show an excess of PNe at large radii on their SE side. Unfortunately, the number of PNe in those regions is too small to determine whether the asymmetry in the distribution is statistically significant.

In the following sections, we present a comparative study between PNe number density and stellar surface brightness for the galaxies in *samples A* and *B*. For the galaxies in *sample C*, the PNe samples are too small to perform this analysis.

In Section 3.1, we describe the stellar surface brightness, and in Section 3.2 we compare it to the radial PNe number density.

3.1 Photometric data of the stellar component

Radial profiles of the stellar surface brightness, position angle, ellipticity ϵ and a_4 shape parameter were obtained from the combination of different data sets in the literature. Mean values are shown in Table 3 together with the sources of the photometry.

Usually, we considered *Hubble Space Telescope* (*HST*) photometry in the innermost 4–5 arcsec, ground-based observations for $r > 10$–11 arcsec and their average values in between.

From the ϵ and a_4 radial profile, we derived their characteristic values by averaging the values within the range 2 $\mathrm{FWHM_{seeing}} < R < 1.5\ R_e$ as done in Bender et al. (1988), Peletier et al. (1990) and Hao et al. (2006). As weights in the average procedure, we use the ratios F/E where F is the flux measured at that position and E is the error in the (ϵ or a_4) measurement. Errors in $\langle\ \epsilon\rangle$ and $\langle\ a_4\rangle$ are computed by measuring the scatter of the measurements in the same spatial region.

The surface brightness radial profiles μ were fitted with (i) a Sérsic profile and (ii) a $R^{1/4}$ plus exponential disc profile, using the robust Levenberg–Marquardt method implemented by Moré, Garbow & Hillstrom (1980). The actual computation was done using the MPFIT algorithm implemented by C. Markwardt under the IDL environment.[2] We would like to note that the aim is not to study in detail the photometric components of the galaxies, but instead to obtain a general description of the mean radial profile of the stellar light. In the cases where *HST* data were not available, we excluded the innermost 1 or 2 arcsec from the fit, to reduce possible contamination due to seeing effects. Results of the fit are shown in Table 3.

[1] In some cases, this could be complicated by population effects. For example, Sambhus, Gerhard & Méndez (2006) found a subpopulation of bright PNe in NGC 4697, which are geometrically and kinematically peculiar. To discover such effects in the PN distribution requires both a large PN sample and accurate PN magnitudes, depending on how clear the signature is. Here, we only consider how well the entire PN population agrees with the surface photometry.

[2] The most recent version of the MPFIT algorithm can be found at http://cow.physics.wisc.edu/~craigm/idl/fitting.html.

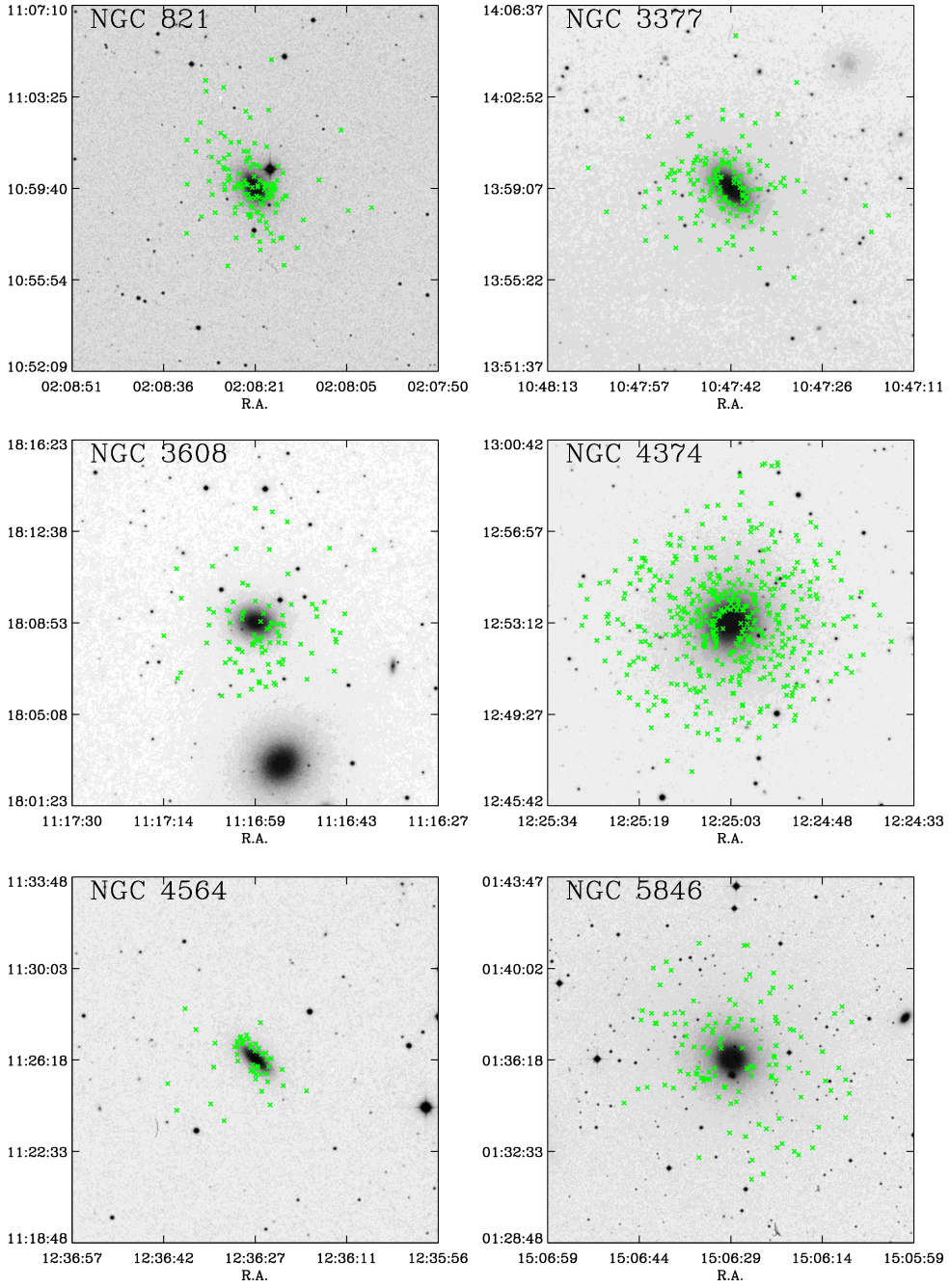

Figure 1. Digitized Sky Survey (DSS) images of galaxies in *sample A* with the PNe positions marked as green crosses. The field-of-view is 13 × 13 arcmin. North is up and east is left.

3.2 Comparison between PNe spatial distribution and surface brightness profiles

In order to compare the stellar surface brightness and the PNe number density, we have to take into account the incompleteness in the PNe detections, e.g. the number of undetected PNe because of their low signal-to-noise ratio. The noise in the field has four main contributions: the sky surface brightness (constant all over the field), the detector readout noise (constant all over the field), the galaxy background (variable over the field) and the presence of foreground stars (variable over the field).

To measure how these four noise sources affect the PNe detection and correct the PN number counts we proceed as follows.

(i) We first generate artificial images, which mimic the sky and CCD readout noise in our observations, and then populate them with simulated point-like sources of different magnitudes.

(ii) We compute the planetary nebulae luminosity function (PNLF) of the simulated objects in the artificial images. In particular, we evaluate the magnitude $m_{80\,\mathrm{percent}}$ at which the loss of objects is significant. $m_{80\,\mathrm{percent}}$ is defined in such a way that for $m < m_{80\,\mathrm{percent}}$, more than 80 per cent of PNe are recovered.

Table 3. Photometric properties of 11 sample galaxies.

Name NGC	Band	μ_S (mag arcsec^{-2})	R_S (arcsec)	n	μ_B (mag arcsec^{-2})	R_{eB} (arcsec)	μ_0 (mag arcsec^{-2})	h (arcsec)	$\langle \epsilon \rangle$	$\langle a_4 \cdot 100/a \rangle$ (per cent)	Reference
(1)	(2)	(3)	(4)	(5)	(6)	(7)	(8)	(9)	(10)	(11)	(12)
821	B	23.0 ± 0.1	39.8 ± 2.0	4.7 ± 0.2	22.0 ± 0.1	20 ± 2	22.4 ± 0.2	29 ± 1	0.38 ± 0.01	0.70 ± 0.1	(1),(2)
3377	B	22.6 ± 0.6	54 ± 4	5.2 ± 0.3	21.5 ± 0.2	26 ± 3	22.1 ± 0.4	40 ± 3	0.50 ± 0.01	0.9 ± 0.9	(1),(2),(3)
3608	B	25.28 ± 0.09	157 ± 10	7.0 ± 0.1	21.9 ± 0.1	19 ± 1	22.5 ± 0.1	53 ± 3	0.19 ± 0.02	-0.15 ± 0.09	(2),(3)
4374	V	23.1 ± 0.2	142 ± 16	8.0 ± 0.6	20.62 ± 0.05	37 ± 1	22.4 ± 0.08	123 ± 3	0.13 ± 0.02	-0.4 ± 0.1	(4)
4564	B	22.1 ± 0.1	33.8 ± 2	3.1 ± 0.2	21.42 ± 0.05	13.3 ± 0.5	20.33 ± 0.02	12.90 ± 0.08	0.39 ± 0.11	0.7 ± 0.9	(1)
5846	V	29 ± 1	2903 ± 192	12 ± 2	22.52 ± 0.04	68 ± 2	24.26 ± 0.07	379 ± 16	0.07 ± 0.05	0.0 ± 0.1	(5)
1023	B	21.4 ± 0.1	60 ± 2	3.9 ± 0.2	20.6 ± 0.1	31 ± 3	21.2 ± 0.1	62 ± 1	0.39 ± 0.05	$0.54 \pm 0.1^{(*)}$	(6)
1344	V	21.5 ± 0.1	50 ± 2	4.1 ± 0.1	21.27 ± 0.07	42 ± 2	21.9 ± 0.5	34 ± 3	0.31 ± 0.03	0.1 ± 0.2	(7)
3379	B	22.1 ± 0.1	47.0 ± 0.2	4.7 ± 0.2	22.25 ± 0.08	57 ± 1	17.2 ± 0.5	0.1 ± 0.5	0.09 ± 0.02	0.2 ± 0.1	(8),(9)
4494	V	21.63 ± 0.07	49 ± 1	3.3 ± 0.1	21.74 ± 0.06	49 ± 2	22.1 ± 0.5	30 ± 7	0.14 ± 0.01	0.2 ± 0.2	(10)
4697	B	20.60 ± 0.04	66 ± 1	3.53 ± 0.06	20.97 ± 0.04	74 ± 1	20.1 ± 0.3	26 ± 3	0.42 ± 0.04	1.4 ± 0.2	(2),(11)

Notes. Col. 1: galaxy name. Galaxies in *sample A* are listed in the upper part of the table. The lower part of the table contains the *sample B* galaxies except NGC 5128. Col. 2: photometric band. Col. 3: surface brightness at R_S. Col. 4: scale radius R_S determined from the Sérsic fit. Col. 5: Sérsic index. Col. 6: bulge brightness at R_{eB} for the $R^{1/4}$ + exponential disc fit. Col. 7: bulge effective radius for the $R^{1/4}$ + exponential disc fit. Col. 8: central surface brightness of the exponential disc for the $R^{1/4}$ + exponential disc fit. Col. 9: scale radius of the exponential disc component fit. Col. 10: weighted mean value for ellipticity in the range 2 FWHM$_{seeing}$ $< R <$ 1.5 R_e. Col. 11: weighted mean value for the a_4 parameter in the range 2 FWHM$_{seeing}$ $< R <$ 1.5 R_e. Positive values correspond to discy isophotes, and negative values to boxy isophotes.

$^{(*)}$From Emsellem et al. (2007). In that paper the error on a_4 is not given, therefore we assumed an arbitrary error of 0.1. Col. 12: reference for the photometric data sets: (1) Goudfrooij et al. (1994); (2) Lauer et al. (2005); (3) Jedrzejewski (1987); (4) Kormendy et al. (2009); (5) Kronawitter et al. (2000); (6) Noordermeer et al. (2008); (7) Sikkema et al. (2007); (8) Capaccioli et al. (1990); (9) Gebhardt et al. (2000); (10) Napolitano et al. (2009); (11) De Lorenzi et al. (2009).

(iii) Now we consider the real, observed images and insert a set of artificial point-like sources in them with a distribution in magnitude given by the observed PNLF, but brighter than $m_{80\,\mathrm{percent}}$. In this way, we are sure (at a 80 per cent confidence level) that our artificial sources would not be undetected because of the background noise (sky plus CCD readout noise).

(iv) We detect the artificial sources in the real images again, and since we know their positions, we can compute the radial completeness factor c_{R}, i.e. the inverse of the fraction of simulated objects recovered at different distances from the galaxy centre.[3] Since we inserted only sources with $m < m_{80\,\mathrm{percent}}$, the loss of objects is attributed only to the galaxy continuum and the stellar trails contamination rather than the sky background or detector noises.

(v) Finally, we group the observed PNe in elliptical annuli, oriented along the galaxy photometric major axis. We compute N_c/A, the number of PNe brighter than $m_{80\,\mathrm{percent}}$ in each annulus (corrected for the radial completeness factor c_{R} evaluated at the annuli centres), divided by the area A of the annulus. We then compute the logarithmic PNe number density $\tilde{\rho}_{\mathrm{PNe}}(R) = -2.5\log_{10}(N_c/A)$.

In Fig. 2, we show the comparison between the major axis stellar surface brightness profile and $\tilde{\rho}_{\mathrm{PNe}}(R)$ for galaxies in *samples A* and *B*.[4] $\tilde{\rho}_{\mathrm{PNe}}(R)$ is shifted by an arbitrary constant (different for each galaxy) to match the stellar profile.

For NGC 1344 and 4697, which are not part of the PNS data set, we could not evaluate the completeness correction with simulated sources because the reduced images were not available. This mostly affects the innermost regions of NGC 4697, in which the inner PNe density profile in Fig. 2 falls slightly below the stellar surface brightness profile.

The conclusion we can derive from this comparison is that the stellar surface brightness and PNe counts agree well for the galaxies where the two sets of data overlap in radius. In the cases where the stellar surface brightness measurements are not extended enough in radius to ensure an overlap with the PNe data, the PNe number density still follows the extrapolation of the surface brightness fits at larger radii.

4 PNE KINEMATICS

In this section, we analyse the kinematics of the sample galaxies using their PNe radial velocities and compare them to long-slit absorption-line kinematics.

In Section 4.1, we define the 'folded catalogue', which we will use in Sections 4.2, 4.3 and 4.4 to measure the global velocity and velocity dispersion fields of the PNe system and their associated errors. In Section 4.5, we extract velocity and velocity dispersion radial profiles from the PNe data and compare them to stellar profiles, to test the consistency of the two sources of kinematic information.

This analysis is done only for galaxies in samples A and B for which sufficient data are available.

4.1 Folded catalogue

To decrease the statistical noise resulting from a low detection number, we assume that the galaxy is point symmetric in phase space. Therefore, each point in phase space, (x, y, v), has a *mirror* counterpart ($-x$, $-y$, $-$v). Here, x and y give the positions of the PNe on the sky, and are centred on the galaxy with y aligned along the galaxy photometric major axis, and v gives the radial velocities of the PNe corrected for the galaxy's systemic velocity (therefore v = 0 at $x = 0$, $y = 0$). By the union of the original data set and the mirrored one, we *virtually* double the number of data points. This technique has often been adopted in the past (e.g. Arnaboldi et al. 1998; Peng, Ford & Freeman 2004). Hereafter, the term 'folded catalogue' refers to the PNe catalogue obtained by the union of the original one and the mirrored counterpart, and we use this one to map the two-dimensional kinematics of the PNe system. The reliability of the point symmetry assumption is tested a posteriori by repeating the calculations using only the original catalogue and comparing the two results. We note that in almost all cases the computed quantities based on the original and folded PNe samples agree well; only in the case of NGC 4374, the rotation field shows asymmetries of the order of 25 km s^{-1} (Section 5.1.4).

4.2 Construction of smoothed two-dimensional velocity and velocity dispersion fields

The computation of the two-dimensional velocity and velocity dispersion fields from the folded catalogue was done using an adaptive kernel smoothing technique, which improves on the method described in Peng et al. (2004). For comparison, two examples of unsmoothed velocity fields are shown in Appendix B.

As stated in Section 3, we use only PNe whose velocities are within 3σ of the mean velocity of their neighbours. Generally, the 3σ outliers we rejected are few, and they make no difference to the output velocity and velocity dispersion fields. The only exceptions are the two galaxies, NGC 3377 and NGC 3608, in which small variations in the resulting two-dimensional fields are seen when outliers are included. However, the outliers in these two cases were more than 5σ away from the galaxy systemic velocity, and therefore we are confident that their exclusion is justified.

At every position (x_P, y_P) on the sky, we computed the velocity and velocity dispersion by

$$\tilde{V}(x_P, y_P) = \frac{\sum_i \mathrm{v}_i w_{i,P}}{\sum_i w_{i,P}} \tag{1}$$

$$\begin{aligned}\tilde{\sigma}(x_P, y_P) &= \left\langle V^2 \right\rangle - \langle V \rangle^2 - \Delta V^2 \Big)^{1/2} \\ &= \left(\frac{\sum_i \mathrm{v}_i^2 w_{i,P}}{\sum_i w_{i,P}} - \tilde{V}(x_P, y_P)^2 - \Delta V^2 \right)^{1/2}\end{aligned} \tag{2}$$

where v_i is the ith PN velocity and ΔV^2 is the measurement error ($\sim$20 km s^{-1}), which is a combination of instrumental error related to the PNS ($\sim$17 km s^{-1}; Merrett et al. 2006) and the accuracy in determining the planetary nebula position (a few km s^{-1}); $w_{i,P}$ is the distance-dependent weight for the ith PN, defined using the Gaussian kernel:

$$w_{i,P} = \exp \frac{-D_i^2}{2k(x_P, y_P)^2}, \tag{3}$$

where k is the kernel amplitude and $D_i = \sqrt{(x_i - x_P)^2 + (y_i - y_P)^2}$ is the distance of the ith PN from (x_P, y_P).

Errors on $\tilde{V}$ and $\tilde{\sigma}$ are obtained using Monte Carlo simulations, which will be discussed in Section 4.3.

The weighting procedure depends on the distance D from (x_P, y_P) and on the amplitude k of the kernel. The latter is a measure of the spatial resolution at which we would like to investigate the

[3] Distance from the centre is computed taking into account the mean galaxy ellipticity: $R^2 = X^2/(1-e)^2 + Y^2$, where Y is aligned along the major axis.
[4] NGC 5128 is not included because of the lack of an extended surface brightness radial profile.

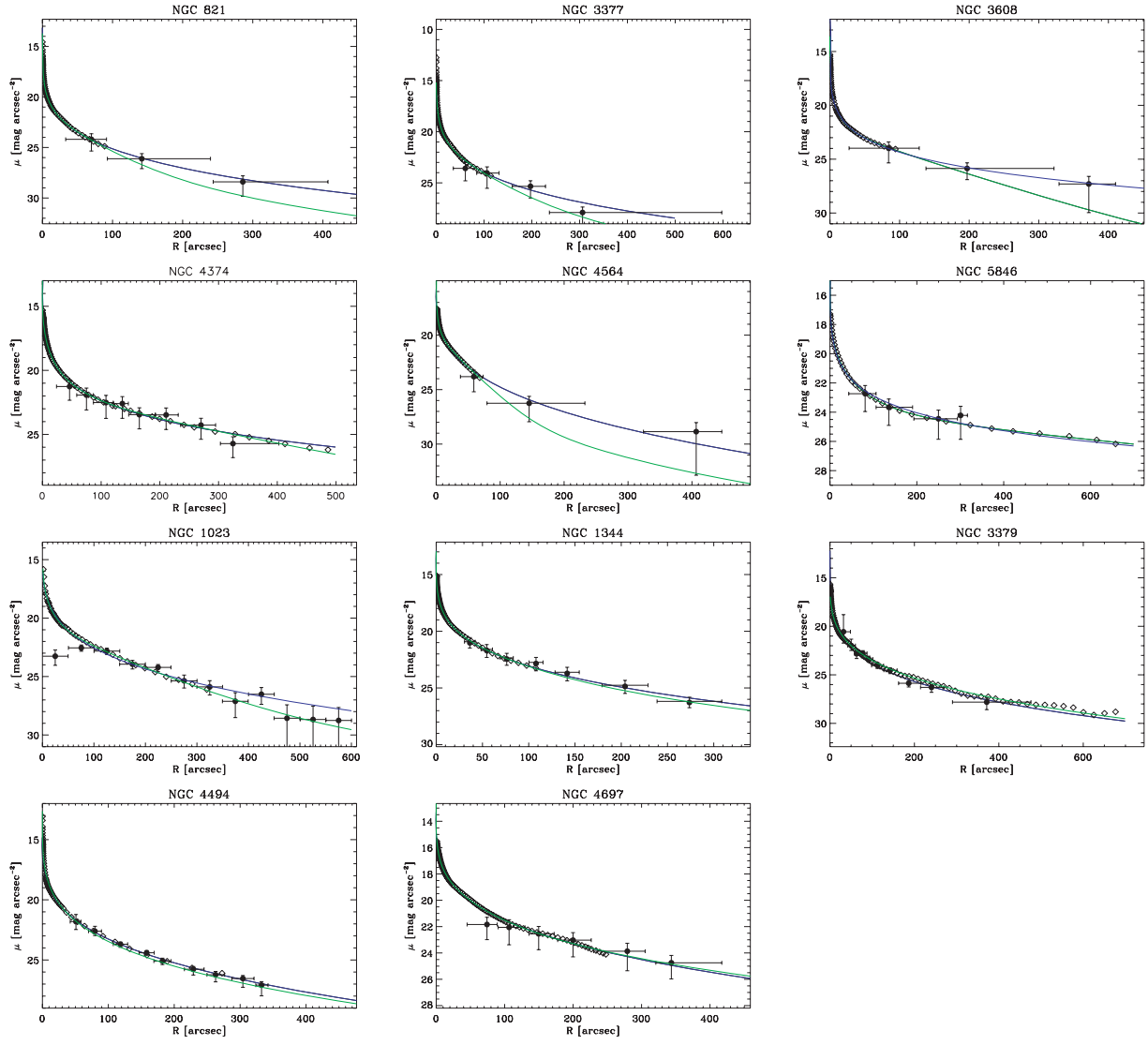

Figure 2. Surface density profiles of PNe and stars. Open diamonds: surface brightness of the stellar component as a function of semimajor axis, according to the references in Table 3. Solid lines: extrapolation of the stellar surface brightness profile with the blue line representing the Sérsic law and the green line representing the $R^{1/4}$ plus exponential decomposition. Filled circles with error bars: scaled logarithmic PNe number density (see text for details).

kinematics. Large values of k will lead to smoother profiles of the velocity and velocity dispersion fields, highlighting the general trend but suppressing kinematic structures at small scales. Conversely, smaller values of k will allow a better spatial resolution, with the risk of amplifying the noise pattern due to the low number of PNe and the measurement errors. The optimal k must therefore be chosen in order to find the best compromise between spatial resolution and noise smoothing. It can be different at each point in the observed field, since it depends on the number density of points, the velocity gradient and the velocity dispersion we want to resolve.

To determine k, we proceeded as follows. At each position on the fields, we define k to be linearly dependent on the distance R_M of the Mth closest PN. We arbitrarily chose $M = 20$ but tested in a range $10 < M < 60$ finding no significant differences in the final results, even for those galaxies with a relatively low number of PNe.

$$k(x, y) = AR_M(x, y) + B = A\sqrt{(x - x_M)^2 + (y - y_M)^2} + B, \quad (4)$$

where x_M, y_M are the coordinates of the Mth closest PN to (x, y). Our definition of R_M can also be used to define the local PNe number density $\rho(x, y)$:

$$\rho(x, y) = \frac{M}{\pi R_M^2} \quad (5)$$

which can be used to relate k to the local PNe density ρ, by combining equations (4) and (5):

$$k(x, y) = A\sqrt{\frac{M}{\pi\rho}} + B. \quad (6)$$

The way k is defined through equation (4) (and its equivalent equation 6) allows it to be smaller in the innermost regions where the spatial density is bigger and larger in the outer regions, where the PNe density is smaller.

In order to select the most appropriate constants A and B, we built simulated sets of PNe (with the number density resembling the observed one) with radial velocities distributed according to a

Table 4. Typical parameters and typical errors for the smoothed, two-dimensional velocity and velocity dispersion fields.

Name	A	B (arcsec)	$\langle V \rangle$ (km s^{-1})	$\langle \Delta\sigma \rangle$ (km s^{-1})
(1)	(2)	(3)	(4)	(5)
NGC 0821	0.24	10.68	30	20
NGC 3377	0.57	−0.08	25	20
NGC 3608	0.08	33.56	40	30
NGC 4374	0.97	22.72	25	20
NGC 4564	0.24	10.68	20	20
NGC 5846	0.00	60.00	50	30

Notes. Cols 2–3: values of A and B used in the kernel smoothing procedure (see equation 4) as determined from the simulations. Cols 4–5: typical error on the two-dimensional velocity and velocity dispersion fields as determined from Monte Carlo simulations (see Section 4.3 for details).

chosen velocity gradient and velocity dispersion, which mimic the observations. The artificial sets were processed with the adaptive kernel procedure using different values of A and B until the simulated input velocity field was recovered. Therefore, for a given density, velocity gradient and velocity dispersion, we have the most reliable values for A and B to use which give the best compromise between kinematic resolution and smoothing (see Table 4).

We show in Fig. 3 the smoothed two-dimensional velocity and velocity fields for galaxies in *sample A* derived with this technique. The two-dimensional fields of the *sample B* galaxies are presented in Appendix B.

4.3 Errors in the velocity and velocity dispersion fields

Errors on the derived smoothed velocity and velocity dispersion fields are computed by means of Monte Carlo simulations.

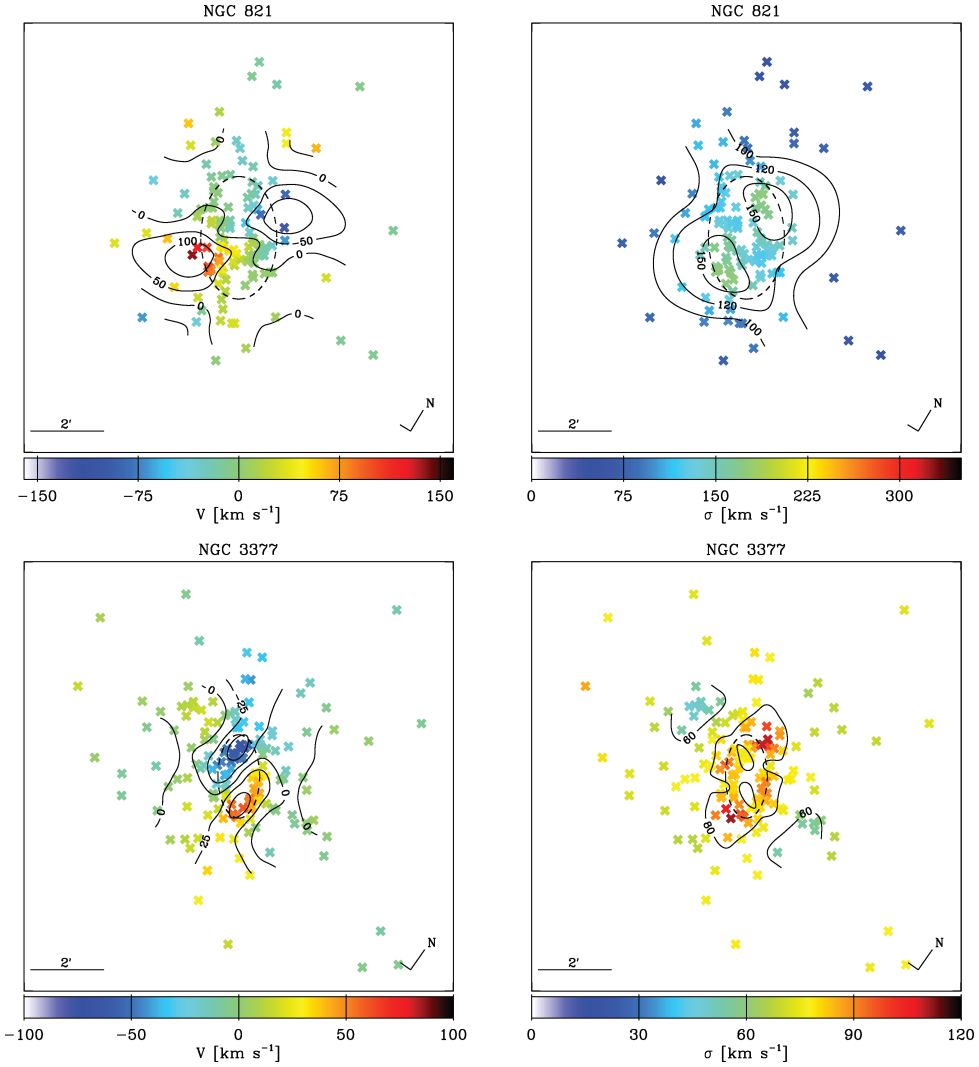

Figure 3. Smoothed two-dimensional velocity (left-hand panels) and velocity dispersion (right-hand panels) fields of galaxies in *sample A* from PNe data. Spatial scale and orientation are given in the panels. The photometric major axis as given in Table 1 is aligned along the vertical axis. Crosses represent the locations of the PNe, while the colours represent the values of the smoothed velocity (or velocity dispersion) field at those points. The colour scale is given at the bottom of each panel. The dashed ellipses are located at 2 effective radii, which are listed in Table 1. Two-dimensional fields of the *sample B* galaxies are presented in Appendix A.

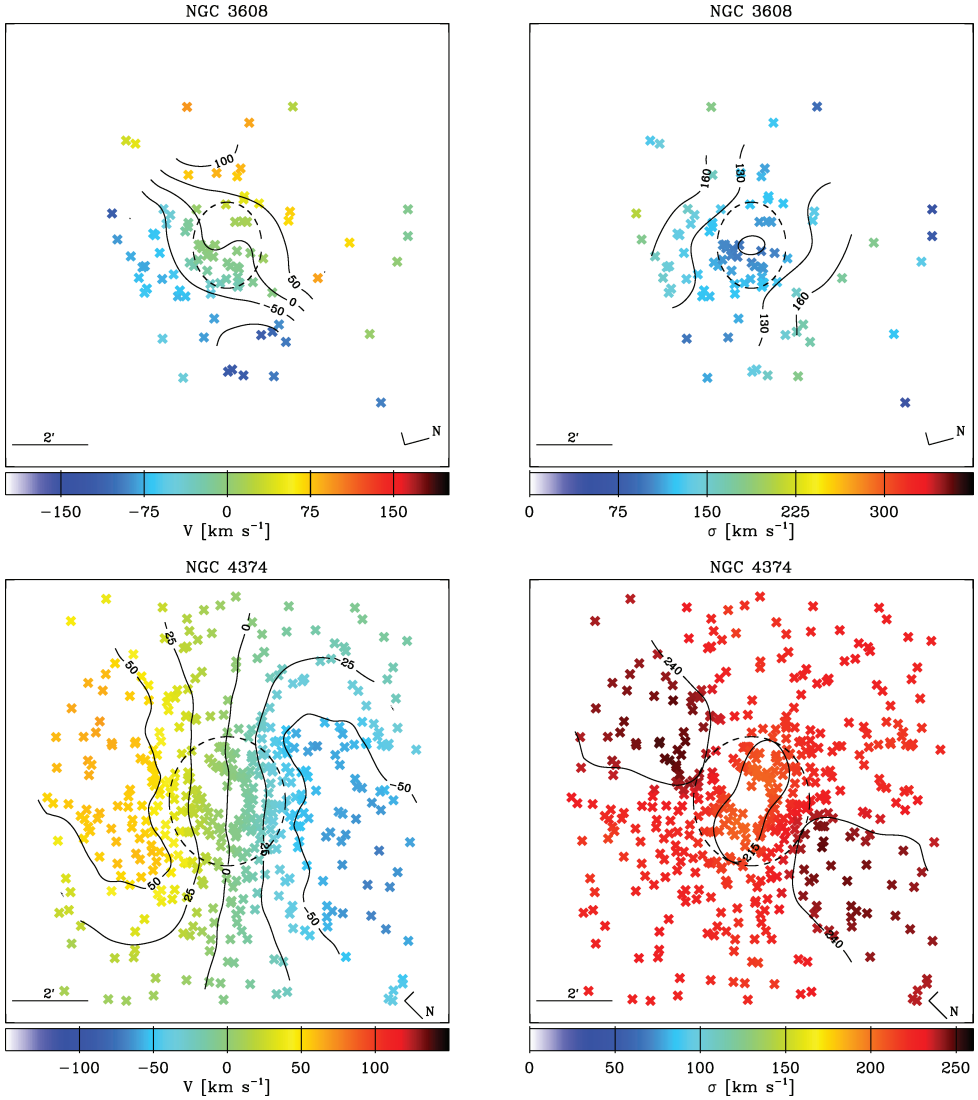

Figure 3 – *continued*

For each galaxy, we built 100 data sets of PNe with simulated radial velocities at the same positions as in the observed (folded) data set, to mimic the observations. The radial velocity for each simulated object was calculated from the observed two-dimensional smoothed velocity field by the addition of a random value. The random value must resemble the observed velocity dispersions and associated measurement errors, and therefore it was chosen randomly from a Gaussian distribution centred at 0 and with dispersion equal to

$$\sigma = \overline{\tilde{\sigma}^2 + \Delta V^2}, \quad (7)$$

where $\tilde{\sigma}$ is the velocity dispersion measured at that position and V is the velocity error.

These simulated data sets were processed with the same reduction script and parameters as the observed ones. The statistics of the simulated velocity and velocity dispersion fields give us the error associated with any position in the observed fields. Average values are given in Table 4.

Two-dimensional error fields are not shown, but errors derived from them will be shown in the plots of the kinematics extracted along the kinematic major axis (Section 4.3.1) and along the photometric major and minor axes (Section 4.5.2).

These simulations are used also to investigate two main aspects: (i) if the measured rotation is significant and (ii) if the misalignment between kinematic ($PA_{\rm KIN}$) and photometric ($PA_{\rm PHOT}$) major axes or the twisting of the velocity fields are significant.

4.3.1 *Testing the rotation*

We extracted the velocity curve $V_{\rm major}$ along the kinematic major axis of the PNe system from the smoothed two-dimensional velocity field. To find its direction, we fitted the PNe velocities with a simple rotation model:

$$V_{\rm PN}(\phi_{\rm PN}) = V_{\rm max} \cos(\phi_{\rm PN} - PA_{\rm KIN}), \quad (8)$$

where $\phi_{\rm PN}$ is the position angle of the PN on the sky, the constant $V_{\rm max}$ measures the amplitude of rotation and $PA_{\rm KIN}$ is the position of the kinematic major axis. Angles are measured on the sky plane, starting from north going counterclockwise.

Then, we created 100 simulated data sets of PNe at the same positions as the observed ones, with velocity equal to zero plus a random error. The random value was generated as in Section 4.3,

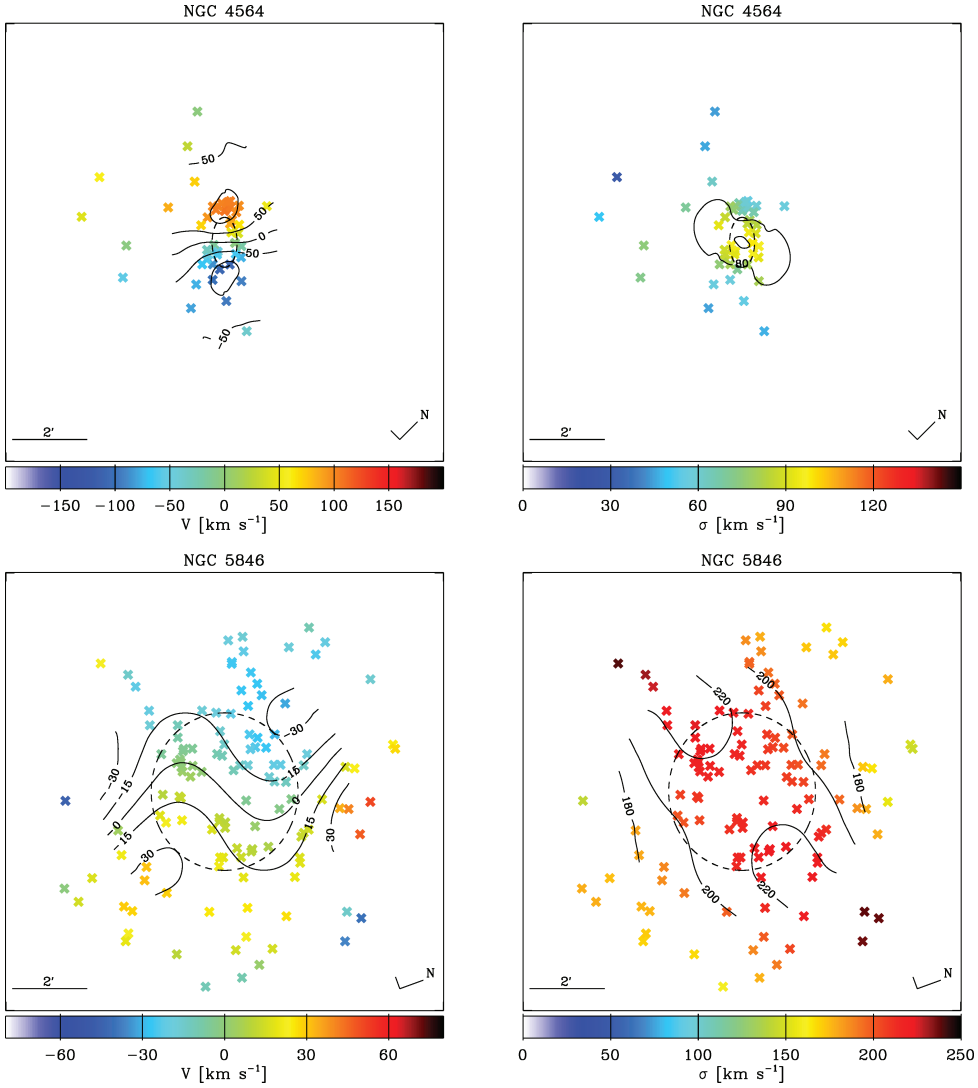

Figure 3 – *continued*

from a Gaussian distribution with mean zero and dispersion depending on the observed velocity dispersion and the measurement error (see equation 7).

We built the two-dimensional velocity field from the simulated catalogues using the same procedures and the same parameters adopted for the real catalogues, and extracted the simulated rotation curve along the direction of the kinematic major axis.

Since the simulated catalogues were artificially generated to have their PNe velocities consistent with 0 km s^{-1}, the rotation we observed on the simulated two-dimensional fields is only an artefact of the noise, as specified by the limited number of data points, the measurement errors and the intrinsic velocity dispersion of the galaxy.

By looking at the distribution of the 100 simulated rotation curves, we determined the region in position–velocity space where the rotation is consistent with 0 km s^{-1} at the 1σ level. In Fig. 4, we show the velocity radial profiles measured along the kinematic major axis of the observed two-dimensional field together with the 1σ confidence level of zero rotation.

The general result is that the PNe rotation we measure is real (with the exception of NGC 5846). The typical 1σ range in which the velocity is consistent with zero is around 20–30 km s^{-1}, depending mostly on the number of detections and the velocity dispersion value.

4.3.2 *Testing misalignment and twisting*

In this section, we investigate how precisely we are able to identify the kinematic major axis of the PNe system (and thereby ascertain whether the misalignment with the photometric axis is consistent with zero or not). We also investigate the reliability of distortions in the velocity field, which may be interpreted as an effect of triaxiality.

To do that, we measured the kinematic position angle of all the simulated fields computed in Section 4.3. The standard deviation of these values gives us an estimate of the error in the kinematic major axis determination. These errors typically range between 10° and 25°, depending on the number of PNe, and on the amount of rotation and velocity dispersion: errors are smaller in galaxies with larger number of PNe and higher V/σ (see also Napolitano et al. 2001). Results for $PA_{\rm KIN}$ and errors are given in Table 5, as well as the misalignment between kinematic and photometric major axes. The

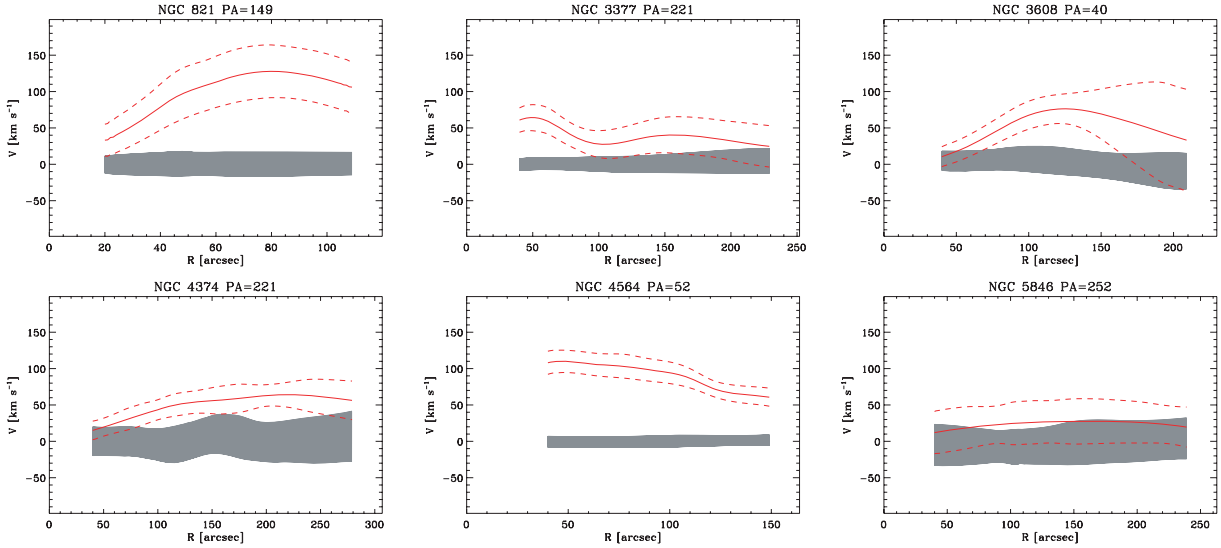

Figure 4. Red line: radial profile of observed mean velocity for the PNe system extracted along the kinematic major axis of the two-dimensional field of Fig. 3. Red dashed lines: 1σ error on the observed mean velocity. The grey area spans the region for which the rotation is consistent with 0 (within 1σ level), as measured from 100 simulated data sets with zero intrinsic rotation (see Section 4.3.1 for details).

Table 5. Kinematic position angles and misalignments.

Name (NGC) (1)	$PA_{\rm KIN}$ (○) (2)	$\lvert PA\rvert_{\rm PNe}$ (○) (3)	Twist? (4)	$PA_{\rm KIN}^{\rm STARS}$ (○) (5)	$\lvert PA\rvert_{\rm STARS}$ (○) (6)
0821	149 ± 25	56 ± 25	No	31	6
3377	221 ± 20	6 ± 18	Yes	226	11
3608	40 ± 29	35 ± 29	No	−95	10
4374	221 ± 18	86 ± 18	No	141	6
4564	52 ± 10	5 ± 10	No	49	2
5846	237 ± 86	13 ± 86	No	306	56
1023	93 ± 10	6 ± 10	No	89	2
1344	197 ± 27	32 ± 27	No	–	–
3379	-71 ± 40	39 ± 40	No	−108	2
4494	180 ± 17	0 ± 17	No	–	–
4697	254 ± 14	4 ± 14	No	–	–
5128	252 ± 6	37 ± 6	No	–	–

Notes. Col. 1: galaxy name. Galaxies of *Sample A* are listed at the top of the table, galaxies of *Sample B* at the bottom. Col. 2: kinematic position angle of the PNe system (receding side), measured from north towards east. Col. 3: absolute difference between $PA_{\rm KIN}$ and $PA_{\rm PHOT} \pm 180$. $PA_{\rm PHOT}$ is given in Table 1. In the case of NGC 5846, the measured rotation is consistent with 0 km s^{-1}; therefore the error on $PA_{\rm KIN}$ is very large and the measurement of $PA_{\rm KIN}$ itself is not useful. Col. 4: twisting of the PNe kinematic major axis, if present. Col. 5: kinematic position angle of the stars (receding side), measured from two-dimensional velocity maps, if available (Cappellari et al. 2007). Col. 6: absolute difference between $PA_{\rm KIN}^{\rm STARS}$ and $PA_{\rm PHOT} \pm 180$.

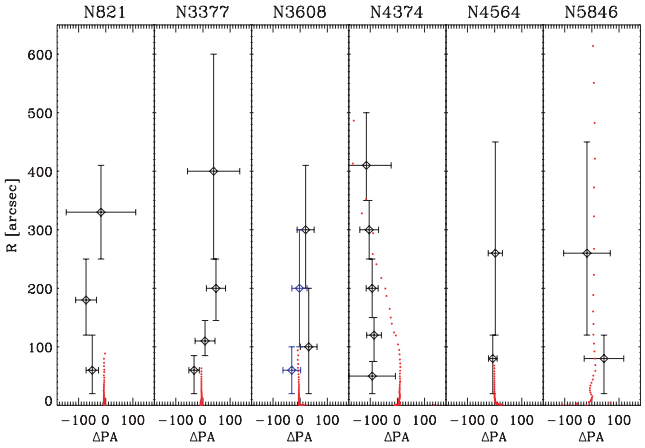

Figure 5. Radial dependence of the misalignment between the photometric and kinematic major axes (as derived from the PNe kinematics) $PA = PA_{\rm PHOT} - PA_{\rm KIN}(\pm 180^\circ)$ for galaxies in *sample A* (black open diamonds). $PA_{\rm PHOT}$ is the constant position angle given in Table 1. Blue open diamonds in the NGC 3608 panel represent the kinematic position angles calculated considering only the PNe on the north side of the galaxy. This subsample is defined and discussed in Section 5.1.3. Significant misalignment is observed in NGC 821 and 4374, while a twist in the direction of rotation is observed in NGC 3377. For NGC 3608 and 5846, no definitive conclusions can be derived within the errors. Red dots show $PA_{\rm PHOT} - PA(R)$, where $PA(R)$ is the photometric major axis radial profile from the referenced papers listed in Table 3.

kinematic and photometric major axes are aligned in NGC 3377 (on average) and NGC 4564, but misaligned in NGC 821, NGC 3608 (marginally) and NGC 4374.

The kinematic major axis $PA_{\rm KIN}$ might also not be constant with radius. To test that, for each galaxy we divided the PNe data set into elliptical annuli (the ellipticity of each annulus is the galaxy's mean ellipticity, as given in Table 3) and calculated the position angle at each radial position using equation (8) and Monte Carlo simulations to compute the errors. This is shown in Figs 5 and 6 for galaxies of *Samples A* and *B*, respectively.

A significant twist is observed in NGC 3377. In the inner region ($R < 80$ arcsec) the kinematic position angle (on the receding side) is $PA_{\rm KIN} = 248 \pm 20$, while in the outer regions it decreases linearly to a value of $PA_{\rm KIN} = 167 \pm 20$ at $R = 200$ arcsec. In the last measured bin, the rotation is very low (see Section 5.1.2) and therefore errors in $PA_{\rm KIN}$ are too large to derive definitive conclusions. For other galaxies, the twist is consistent with 0 within the errors.

Together with the kinematical twisting, Figs 5 and 6 also show the difference between kinematic and photometric major axis, using $PA_{\rm PHOT}$ as zero-point. An interesting case is NGC 4374: the mean

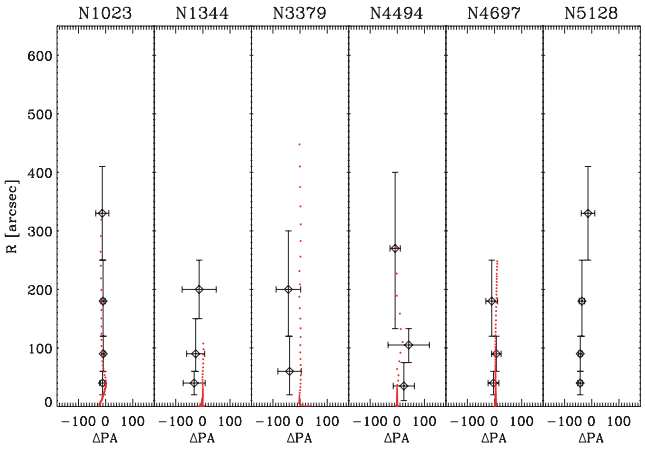

Figure 6. Same as Fig. 5 but for galaxies in *Sample B*.

PA_{KIN} is misaligned by 86° with respect to PA_{PHOT} (see discussion in Section 5.1.4) and the photometric position angle radial profile changes by 100°, reaching PA_{KIN} in the halo regions.

4.4 Results for the velocity and velocity dispersion fields

Smoothed two-dimensional velocity and velocity dispersion fields are shown in Fig. 3 and Appendix B for the galaxies in *samples A* and *B*. They will be used in the computation of the λ_R (proxy for angular momentum per unit mass) (Section 6.3), the outer $\langle V/\sigma \rangle$ ratio (Section 6.2) and in the comparison with stellar kinematics (Section 4.5.2).

A general result emerging from the inspection of the velocity fields in Fig. 3 and the quantitative analysis in Fig. 4 is that rotation is present in all *sample A* galaxies, except in NGC 5846 in which the rotation is consistent with 0 (see Section 4.3.1).

In the galaxies with significant rotation, the kinematic major axis may or may not be aligned with the photometric major axis, within the error bars (see Table 5). Both are aligned in NGC 3377 (on average) and NGC 4564, but misaligned in NGC 821, NGC 3608 (marginally) and NGC 4374. In the *sample B* galaxies, misalignment is seen in Cen A (NGC 5128) and (marginally) in NGC 1344 and 3379. Individual cases will be discussed separately in Section 5.

Twisting of the kinematic major axis is significant only in NGC 3377 (Fig. 5).

4.5 Comparison with stellar kinematics

An important aspect of our analysis is to check whether the PNe kinematics are in agreement with the stellar absorption-line kinematics. To do that, we retrieved major and minor (where available) stellar kinematic data from the literature, and compared it to the PNe kinematics extracted along the same axis.

4.5.1 Long-slit kinematics

Stellar kinematics from long-slit or integral-field spectroscopy are available in the literature for the majority of the galaxies. We give the list of references for each galaxy in Section 5. For two galaxies in *sample A* (NGC 3377 and 4374), we obtained new deep long-slit observations. Also the E1 galaxy NGC 4494, which is part of the PNS galaxy sample, was observed during this run. Its PNe kinematics and properties together with a new dynamical analysis are discussed in a separate paper (Napolitano et al. 2009).

Appendix C gives the kinematic data derived from the long-slit spectra.

4.5.2 PNe radial profiles and comparison with stellar kinematics

Radial kinematic profiles have been extracted from the PNe data in two different ways.

The first method uses the interpolated smoothed two-dimensional fields and their errors presented in Sections 4.2 and 4.3. The second method selects only those PNe within an angular section aligned along a desired position angle (the same for which the stellar kinematics are observed). Usually, the range of angles is between 30° and 60°, depending on the number of PNe. Then the selected PNe are folded to positive radii (i.e. the receding side of the system) and grouped into radial bins containing the same number of PNe. The number of objects N_{BIN} per bin ranges from 10 to 30, to reach a compromise between the number of bins and a statistically significant number of PNe in each bin. In each bin the weighted mean velocity V_{BIN} and velocity dispersion σ_{BIN} are computed; weights are computed from the measurement errors on the PNe velocities. The derived values of V_{BIN} and σ_{BIN} change by less than 10 km s^{-1} if instead all weights are equal, or if the weights from Hargreaves et al. (1994) are used. Errors are computed with the usual formulae $\Delta V_{BIN} = \sigma_{BIN}/\sqrt{N_{BIN}}$ and $\Delta\sigma_{BIN} = \sigma_{BIN}/\sqrt{2(N_{BIN}-1)}$.

Both methods have the advantage that we can extract the radial profile along any direction we desire, and the disadvantage that it might be contaminated by PNe far away from the direction we are interested, by the use of a large kernel smoothing parameter in the first method or a large angular range in the second. Especially if a nearly edge-on disc is present, both techniques could therefore lead to systematically low rotation and systematically high dispersions on the major axis, caused by the dilution from off-axis velocities. However, simple simulations show that this effect is smaller than the error bars in the measurement, and in any case leads to an underestimate of the significance of rotation in Fig. 4.

In Fig. 7, we compare the (folded) velocity and velocity dispersion radial profiles of stars and PNe. Values are shown in Table 6. In general, the stellar and PNe kinematics agree well, with NGC 821 as the most uncertain case. A more detailed description is given in Section 5.

5 NOTES ON INDIVIDUAL GALAXIES

5.1 Sample A

5.1.1 NGC 821

NGC 821 is a field elliptical galaxy. It is classified as an E6 in the RC3 and NED catalogues, but we measured a mean ellipticity of 0.4. The PNe system of NGC 821 was studied for the first time by Romanowsky et al. (2003, 104 PNe). The declining radial profile of the velocity dispersion observed from the combination of stellar and PNe data was interpreted as a signature of low dark matter concentration in this galaxy halo, lower than the prediction by cosmological simulations. Recently, Forestell & Gebhardt (2008) extended the stellar kinematic measurements to ∼100 arcsec, claiming a discrepancy between stellar and PNe kinematics (the velocity dispersions measured with PNe are lower than the ones measured with absorption lines). Using three-integral models they derived a dark matter content that is slightly higher than

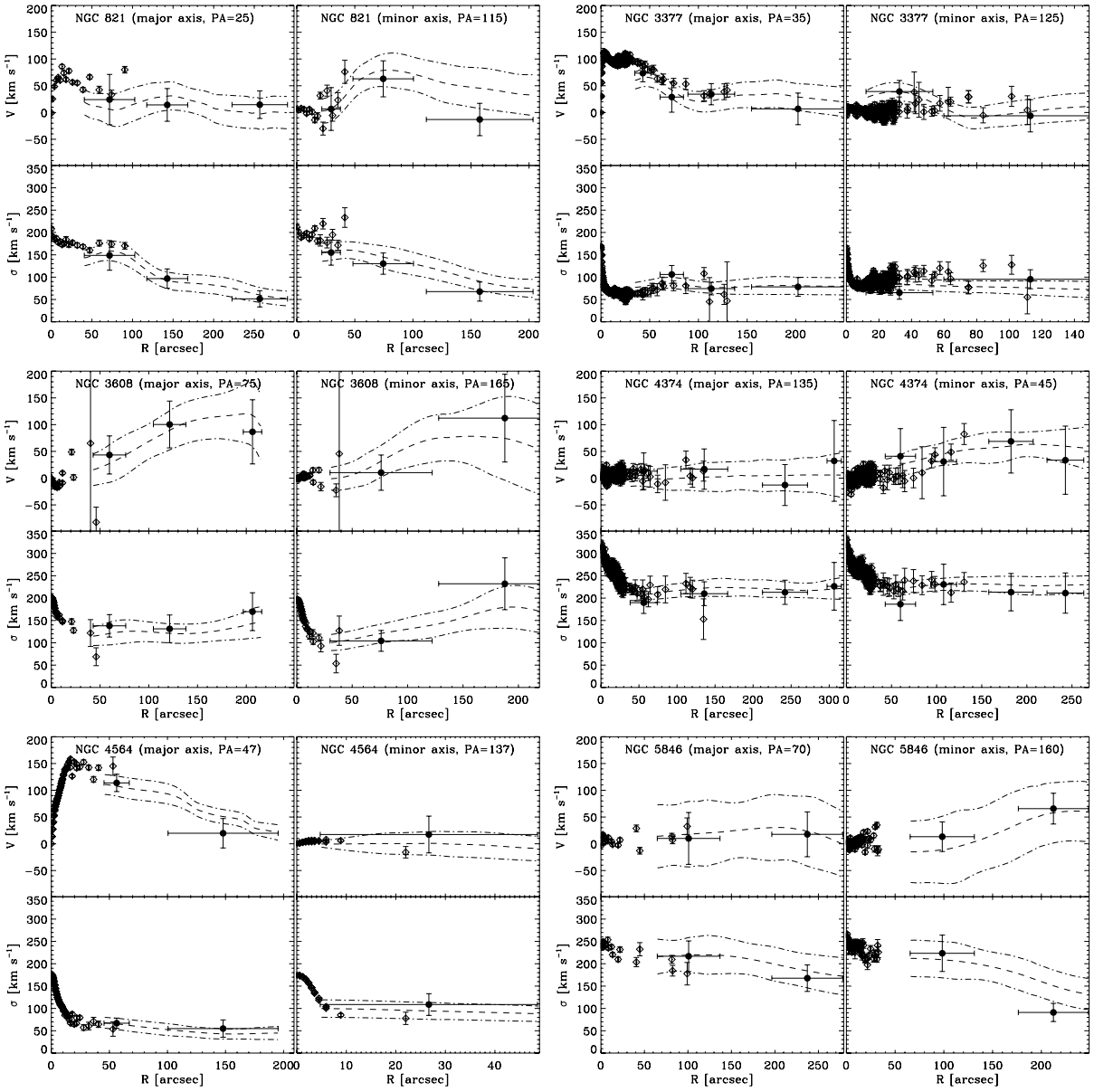

Figure 7. Comparison between long-slit stellar and PNe kinematics. Each galaxy is represented by a subfigure consisting of radial velocity (upper panels) and velocity dispersion profiles (lower panels) extracted along the photometric major (left-hand panels) and minor axes (right-hand panels). The position angles given are from Table 1. Open diamonds represent the stellar kinematics while the filled circles represent the PNe kinematics extracted along a cone aligned with the major or minor axis. The dashed lines represent the kinematics extracted along the major or minor axis from the two-dimensional field and the dot–dashed lines represent the related error at the 1σ level calculated from Monte Carlo simulations (see text for details). References for the absorption-line kinematics: NGC 821, Forestell & Gebhardt (2008); NGC 3377, our VLS/FORS2 data (see Appendix C); NGC 3608, Halliday et al. (2001); NGC 4374, our VLS/FORS2 data (see Appendix C); NGC 4564, Halliday et al. (2001); NGC 5846, Kronawitter et al. (2000, major axis) and Emsellem et al. (2004, minor axis). Electronic tables with the kinematic data plotted in this figure are available in the online version of this paper. References for the absorption-line kinematics: NGC 1023, Debattista et al. (2002, major axis) and Simien & Prugniel (1997, minor axis); NGC 1344, Teodorescu et al. (2005); NGC 3379, Statler & Smecker-Hane (1999); NGC 4494 our VLS/FORS2 data (see Appendix C); NGC 4697, Dejonghe et al. (1996, major axis) and Binney et al. (1990, minor axis); NGC 5128, Hui et al. (1995, major axis), minor axis not available.

determined by Romanowsky et al. (2003), but still lower than predicted by cosmological simulations.

In this paper, we have obtained a new PNS catalogue with 125 detections. To compare their spatial distribution with the stellar surface density profile, we used ground-based photometric data in the *V* band measured by Goudfrooij et al. (1994), combined with the *HST* measurements (F555W, shifted artificially by −0.06 mag to match the ground-based data) given by Lauer et al. (2005). The extrapolation of the Sérsic fit to the surface brightness profile out to ≈300 arcsec agrees well within the error bars with the number density radial profile of the PNe (Fig. 2).

The smoothed PNe two-dimensional velocity field produced in Section 4.2 using the folded PNe sample shows a rotation of ∼120 km s^{-1}, with a misalignment of 56 ± 25° between the

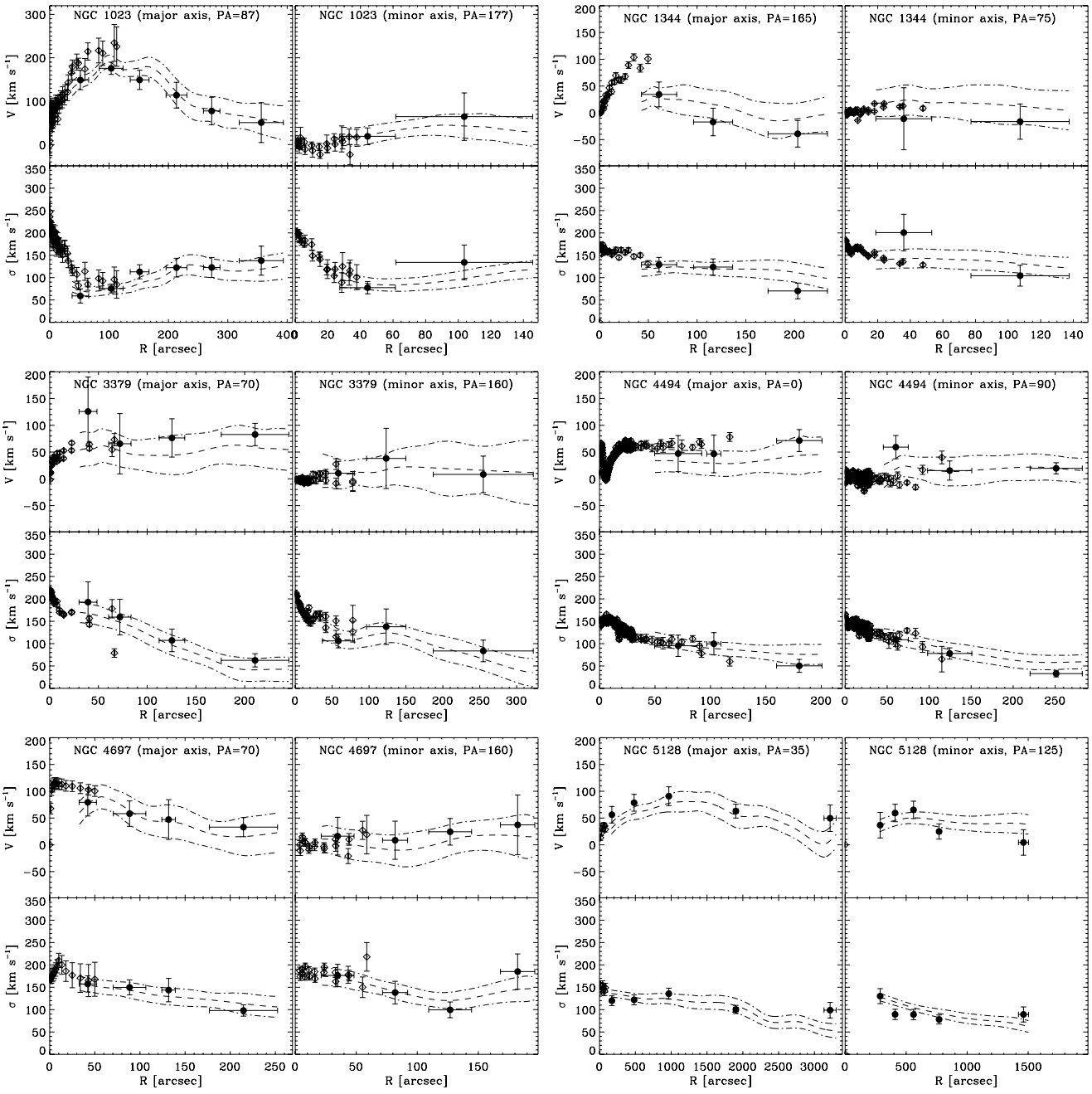

Figure 7 – *continued*

photometric major axis ($PA_{\rm PHOT} = 25$, from RC3) and the PNe kinematic major axis ($PA_{\rm KIN} = -31$, direction of the approaching side). The misalignment between $PA_{\rm PHOT}$ and $PA_{\rm KIN}$ is confirmed also if we use the unfolded PNe sample. This test excludes the possibility that the observed rotation is produced by a few background sources erroneously identified as PNe, which skew the velocity distribution.

The comparison between PNe and stellar absorption-line kinematics is shown in Fig. 7. Long-slit data are from Forestell & Gebhardt (2008), which agree with the integral-field stellar kinematics from Emsellem et al. (2004). The PNe velocities at ∼70 arcsec may be systematically slightly lower than the absorption-line points but the two data sets still appear consistent within the error bars of the PNe points and the scatter of the absorption-line data.

Along the photometric major axis, the stellar component suggests a plateau in the rotation curve with $V \simeq 60$ km s^{-1} for $R < 90$ arcsec, while the PNe system shows a lower value of ∼15–20 ± 40 km s^{-1} for $R > 120$ arcsec. Along the photometric minor axis, the scatter in the stellar kinematics is quite large, and it is difficult to make a clear comparison. Nevertheless, we see an increase of the stellar rotation in the region 20–50 arcsec in good agreement with the PNe data. The galaxy thus exhibits both major and minor axis rotation, and so is most likely triaxial. In particular, the outer regions of NGC 821 ($R > 50$ arcsec) have the positive side of rotation aligned

Table 6. Kinematic data used in Fig. 7.

Name (NGC) (1)	*PA* (◦) (2)	*R* (arcsec) (3)	*V* (km s^{-1}) (4)	*V* (km s^{-1}) (5)	$\sigma\Delta$ (km s^{-1}) (6)	σ (km s^{-1}) (7)	Flag (8)
821	25	0.00	−1.1	1.7	208.2	4.4	1
821	25	1.41	25.4	1.4	191.7	3.0	1
821	25	3.76	48.5	1.6	185.1	4.2	1
821	25	6.11	60.1	1.9	187.0	4.7	1
821	25	8.46	65.7	1.7	177.8	3.9	1
821	25	10.81	60.2	2.8	179.9	4.2	1
821	25	13.16	85.9	3.8	172.8	4.4	1
821	25	15.51	73.8	3.8	175.3	5.3	1
821	25	18.09	61.7	3.4	184.2	6.4	1
..							
5846	160	212.40	65.7	28.8	91.0	20.3	0

Notes. This is a sample: the complete table is published as Supporting Information in the online version of this article. Col. 1: galaxy NGC number. Col. 2: observed position angle, according to Fig. 7. Col. 3: distance from the centre. Col. 4: radial velocity. Col. 5: error on radial velocity. Col. 6: velocity dispersion. Col. 7: error on velocity dispersion. Col. 8: data source. 1 = from absorption-line kinematics; 0 = from PNe kinematics.

with $PA = 149 \pm 25$ (see Fig. 3 and Table 5), while the inner regions have the positive side of rotation aligned with $PA = 31$ (Cappellari et al. 2007, but see also fig. 4 in Emsellem et al. 2004), indicating a misalignment of 118◦ between inner and outer regions.

The fact that PNe and absorption-line kinematics show different misalignments with $PA_{\rm PHOT}$, 56◦ and 6◦, respectively (Table 5), could be because these two quantities are computed in different radial intervals: the PNe misalignment is computed for $R \geq 30$–40 arcsec, while the absorption-line misalignment is computed for $R < 20$ arcsec [from Spectrographic Areal Unit for Research on Optical Nebulae (SAURON) kinematics]. There is a (small) region of overlap between the PNe kinematics and the long-slit data in Fig. 7, in which there is no evidence that the PNe and absorption-line data disagree. Both sets of data may trace different regions of the same velocity field, if the kinematics major axis changes rapidly from the centre outwards.

The combined velocity dispersion profile along both axes shows a strong decrease, reaching $\sigma \simeq 50$ km s^{-1} at 250 arcsec.

5.1.2 NGC 3377

NGC 3377 is an E5 galaxy in the Leo I group. This galaxy has been studied on numerous occasions. Mass models have been obtained over different radial ranges, from the very inner regions to measure the supermassive black hole mass (e.g. Magorrian et al. 1998; Gebhardt et al. 2003), out to $\sim 1\,R_{\rm e}$ to determine the mass-to-light ratio, orbital structure and dynamical properties (e.g. Cappellari et al. 2006; van der Marel & van Dokkum 2007). The large number of PNe obtained with the PNS (154 detections) derived in the present paper allows us to extend the kinematic information out to $\sim 5\,R_{\rm e}$.

We used ground-based photometric data in the *B* band measured by Goudfrooij et al. (1994) and Jedrzejewski (1987), combined with the *HST* measurements given by Lauer et al. (2005) (F555W, shifted artificially by −0.08 mag to match the ground-based data). In the small overlapping region ($60 < R < 100$ arcsec), the PNe counts follow the stellar surface brightness within the error bars. In the region $100 < R < 200$ arcsec, the PNe counts follow the Sérsic fit extrapolation of the stellar surface brightness. The last PNe data point at 300 arcsec has too large error bars to derive conclusions.

The PNe system shows a twist of the kinematic major axis, from $PA_{\rm KIN} = 248 \pm 20$ at $R = 60$ arcsec up to $PA_{\rm KIN} = 167 \pm 20$ at $R = 200$ arcsec. The stellar surface brightness is not extended enough to check whether or not this twisting is reproduced also in the photometry.

Our deep stellar long-slit kinematics obtained with Focal Reducer/low dispersion Spectrograph (FORS)/VLT (see Appendix C) show a good agreement within errors with the PNe velocity and velocity dispersion extracted along both major and minor axes. Along the major axis, this galaxy shows a very steep central rotation gradient within 5 arcsec together with a central velocity dispersion $\sigma = 170$ km s^{-1} most likely due to the contribution of the central black hole (Gebhardt et al. 2003). The stellar radial velocity reaches a maximum value $V \approx 115$ km s^{-1} within 40 arcsec and then it goes down to $\sim$0 km s^{-1} at 210 arcsec. On the contrary, the velocity dispersion increases from $\approx$60 km s^{-1} at 40 arcsec to $\approx$100 km s^{-1} at 100 arcsec, and then it goes down again to 80 km s^{-1}. This turnover in the velocity dispersion is observed in both the stars and the PNe. Therefore, it appears that despite its classification as an E5, NGC 3377 shows disc-like kinematics in its inner $\sim$70 arcsec (i.e. high value of the maximum rotation velocity, low values of the velocity dispersion).

5.1.3 NGC 3608

NGC 3608 is an E2 galaxy in the Leo II group. The mass models of NGC 3608 constructed so far are confined to the inner regions and are based on stellar long-slit (van der Marel 1991; Magorrian et al. 1998; Gebhardt et al. 2003) or two-dimensional integral-field (Cappellari et al. 2007) kinematics.

Radial velocities for 87 PNe were derived in the present paper. It has a close companion, NGC 3607, about 6 arcmin to the south, whose systemic velocity ($\sim$935 km s^{-1}, from RC3) makes the two PNe systems overlap in phase space. In our PNe analysis, we did not consider the objects closer to NGC 3607 than NGC 3608. This probably still leaves some contaminants in the PNe catalogue: in fact, there is an overdensity of detections on the side of NGC 3608 closer to its companion (see Fig. 1).

We used ground-based photometry by Jedrzejewski (1987) in *B* band and *HST* photometry by Lauer et al. (2005) (F555W, artificially shifted by 0.92 mag to match the ground-based data). Unfortunately, no spatial range exists where the stellar surface brightness and PNe data overlap, so a direct comparison is not possible. If we extrapolate the Sérsic fit of the luminous profile, we find a good agreement with the PNe number density (much better than the $R^{1/4}$ + exponential disc fit extrapolation).

The PNe velocity field is quite noisy in the outer region and the PNe major kinematic axis (PA = 40 ± 29◦) is misaligned with the photometric one (PA = 75). Both effects are probably caused by the low number of detections and the possible contamination by the companion galaxy.

Stellar kinematics (PA = 81◦ and $PA = -9$◦) are taken from Halliday et al. (2001). Again, the stars and PNe do not overlap in radial range, so a direct comparison between the kinematics of two systems is not possible. Along the major axis, the stellar kinematics reveal a kinematically decoupled core (already reported by Halliday et al. 2001). Extrapolation of the stellar rotation at 50 arcsec matches the PNe data well, which show an increase of the rotation to $\approx$100 km s^{-1} at $\sim$ 150–200 arcsec. Rotation is also visible along

the minor axis, but the scatter and error bars are too large to derive general conclusions. The velocity dispersion along the major axis decreases from the central 200 km s^{-1} to ≈100 km s^{-1} at ≈ 40–50 arcsec, and then shows an increase to 170 km s^{-1} at $R = 200$ arcsec.

As pointed out before, the PNe sample of NGC 3608 might be contaminated by the presence of PNe belonging to NGC 3607. In order to quantify the contamination effect, we exclude all PNe on the NGC 3607 side (i.e. the southern side). The remaining catalogue contains therefore only 30 PNe on the northern side of NGC 3608, to which we apply the point-symmetric reflection as in Section 4.1. We will refer to this folded, northern-side catalogue as the 'N-sample'. This is a conservative approach as it will eliminate most of the contaminants, but it will also eliminate many PNe of NGC 3608, and the results may suffer from low number statistics.

In Figs 8 and 9, we present the two-dimensional velocity and velocity dispersion fields, and the comparison with stellar kinematics extracted along the major and minor axes using the 'N-sample'. The two-dimensional kinematics of the 'N-sample' are different from those of the original PNe sample; the new velocity field is characterized by more regular rotation, and the new velocity dispersion contours have a different orientation.

The new velocity field has a kinematic position angle of 44 ± 33 for $R < 100$ arcsec and of 72 ± 29 for $R > 100$ arcsec, with an average $PA_{\rm KIN} = 75 \pm 22$. Major and minor axis rotation curves are characterized by steeper gradients: they reach the maximum of the rotation $V_{\rm max}^{\rm major} = 130$ km s^{-1} at 70 arcsec and $V_{\rm max}^{\rm minor} = 140$ km s^{-1} at 60 arcsec before dropping rapidly to ∼ −50 km s^{-1} after 200 arcsec. The radial velocity dispersion profile along the major axis is systematically lower for the 'N-sample'.

Thus, the outer-halo kinematics of NGC 3608 depend strongly on the adopted PNe sample. We therefore consider the results from the 'N-sample' as a separate case, referring to them as NGC 3608N for the rest of the paper.

5.1.4 NGC 4374

NGC 4374 (M84) is a well-studied, bright E1 galaxy in the Virgo cluster. Mass models have been constructed by Kronawitter et al. (2000) and Cappellari et al. (2007) using stellar kinematics within 1 $R_{\rm e}$. With our deep long-slit observations and 457 PNe radial velocity measurements obtained in this paper, we are able to extend the kinematic information out to 6 $R_{\rm e}$.

We used the extended ground-based photometry given by Kormendy et al. (2009), which shows a very good agreement between stellar surface brightness and PNe number density. The data show large variations in the position angle of the photometric major axis. Beyond $R = 80$ arcsec, the photometric position angle increases from 120° to 180°. The shift in position angle may be an effect of the interaction with the nearby galaxy NGC 4406.

The two-dimensional velocity field of NGC 4374 indicates that the kinematic rotation axis ($PA_{\rm KIN} = 221$) is almost orthogonal to the photometric one ($PA_{\rm PHOT} = 135$). Simulations carried out in Section 4.3 clearly indicate that the rotation along that axis is significant (see Fig. 4). The misalignment between kinematic and photometric major axes is seen also in the stellar absorption-line kinematics, which agree well with the PNe data.

The mean velocity field obtained with the 'unfolded' PNe catalogue (Fig. 10) differs from the one calculated with the 'folded' catalogue. In particular, we noted an asymmetry: the receding side reaches ∼ +50 km s^{-1}, while the approaching side reaches ∼ −80 km s^{-1}. This asymmetry in the velocity field is confirmed also in the stellar kinematics, as shown in Fig. 11.

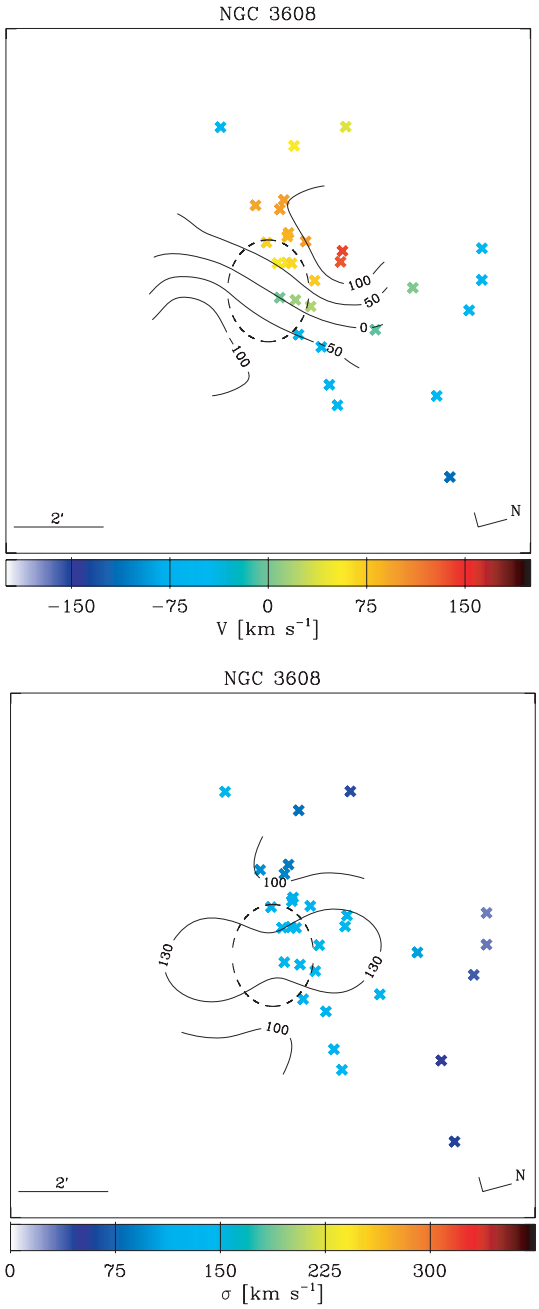

Figure 8. Two-dimensional velocity (upper panel) and velocity dispersion (lower panel) fields of NGC 3608 obtained using the 'N-sample'. Labels, scales and symbols are as in Fig. 3.

The 'unfolded' and 'folded' velocity dispersion fields do not differ significantly from each other. They both show almost constant velocity dispersion, with small fluctuations consistent with measurement errors.

The distortion of the velocity field in NGC 4374 is unlikely to be caused by contamination from PNe belonging to NGC 4406 because the two galaxies have very different systemic velocities. It could possibly be related to the presence of a diffuse intracluster light component in this part of the Virgo cluster (Arnaboldi et al. 1996), or to a current interaction of NGC 4374 with NGC 4406. The angular separation between NGC 4406 and 4374 is ∼17 arcmin ∼87 kpc (at a distance of 17.6 Mpc). NGC 4406 is on the

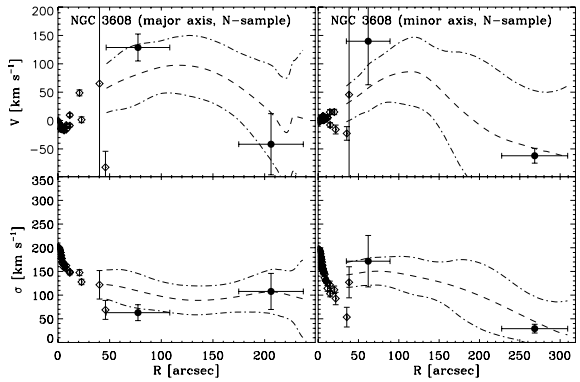

Figure 9. Same as in Fig. 7, but using the NGC 3608 'N-sample'.

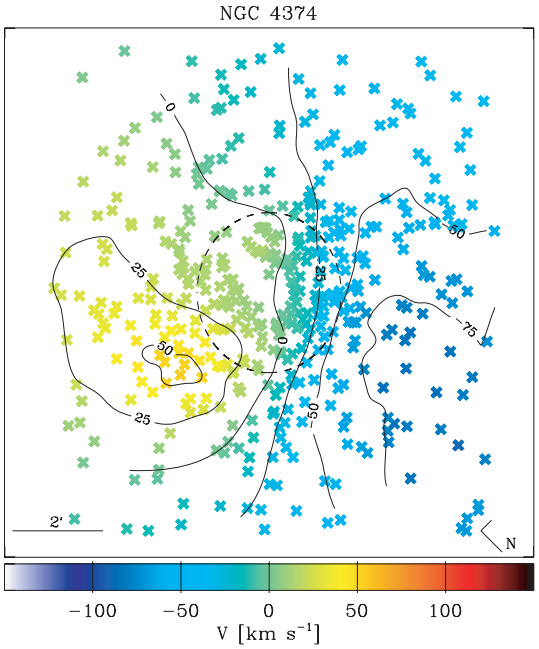

Figure 10. Two-dimensional velocity field of NGC 4374 obtained using the adaptive kernel smoothing procedure (Section 4.2) without imposing point symmetry on the PNe data set.

approaching (NE) side of NGC 4374 with a systemic velocity ∼1300 km s^{-1} lower than NGC 4374, and it is closer by about 1.1 Mpc (see Table 1).

We can exclude that the observed asymmetry is caused by background Lyα galaxies at redshift $z \sim 3.1$ because they are too few to generate such a major distortion of the velocity field. In fact, according to Ciardullo et al. (2002) we would expect ∼2 Lyα contaminants for our field of view (9×9 arcmin^2), redshift range ($z \sim 0.0087$) and completeness magnitude (28 mag).

5.1.5 NGC 4564

NGC 4564 is an E4 galaxy in the Virgo cluster. The number of detections in our data (49 PNe, with 38 outside 2 R_e) is quite low, and a direct comparison of their radial distribution with the stellar surface brightness (Goudfrooij et al. 1994) suffers from small number statistics. The radial range where both data sets overlap is

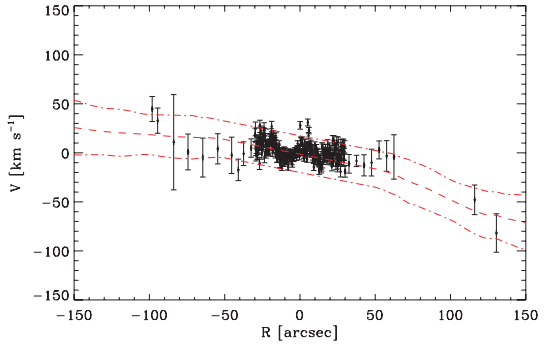

Figure 11. Comparison between the stellar kinematics and the PNe kinematics from the 'unfolded' data set of NGC 4374. Black symbols: stellar kinematics extracted along the photometric minor axis, as shown in Fig. 7 but without folding the two galaxy sides. Dashed red line: PNe kinematics extracted along the same axis of the stars, using the 'unfolded' PNe sample. Red dot–dashed lines: error boundaries computed with Monte Carlo simulations.

small, but there is a good agreement within error bars with the extrapolation of the Sérsic fit to the stellar data.

The two-dimensional velocity field shows a steep central velocity gradient parallel to the photometric major axis. The velocity dispersion field has a central peak of ∼90 km s^{-1} (∼50 arcsec) and then it drops down.

Although the major axis stellar kinematics (Halliday et al. 2001) are not extended enough to have a large overlap with the PNe kinematics extracted along the major axis, the extrapolation of the stellar rotation curve agrees well with the PNe kinematics. The combined major axis rotation curve reaches a plateau (∼140 km s^{-1} at 20 arcsec) and then declines from 50 arcsec to ∼0 km s^{-1} at 180 arcsec. The velocity dispersion decreases from the central 180 km s^{-1} to ∼70 km s^{-1} at $R = 20$ arcsec and then declines slowly to ≈30 km s^{-1} at $R = 150$–200 arcsec. The NGC 4564 major axis rotation curve resembles that of an S0 galaxy rather than that of an elliptical galaxy.

5.1.6 NGC 5846

The E0 galaxy NGC 5846 is the brightest member and the central galaxy in the NGC 5846 group. Mass modelling of NGC 5846 has been performed by van der Marel (1991), Kronawitter et al. (2000), Cappellari et al. (2007), all using stellar kinematics within 1 effective radius. With the PNe measurements (124 detections) obtained with our PNS instrument, we are able to extend the kinematic information of NGC 5846 out to 6 R_e according to Table 1. A separate paper with detailed dynamical models combining stellar kinematics, PNe data and X-ray observations is in preparation (Das et al., in preparation).

Stellar photometric data in V band are taken from Kronawitter et al. (2000). PNe number density and stellar photometry agree well within the error bars.

The two-dimensional velocity field does not show significant rotation. The apparent rotation of ∼ 30 km s^{-1} along $PA = 57°$ seems to be consistent with 0 within the measurement errors (see Fig. 4).

Long-slit stellar data along the major (Kronawitter et al. 2000) and minor (Emsellem et al. 2004) axes are also consistent with no rotation, even if their radial coverage is not sufficient to ensure a proper comparison with PNe kinematics (Fig. 7).

The velocity dispersion along the major axis shows a slightly declining profile, from the central $\sim$250 km s^{-1} down to $\sim$170 km s^{-1} at 250 arcsec.

5.2 Sample B

5.2.1 NGC 1023

NGC 1023 is an S0 galaxy, the brightest member in the eponymous group. Noordermeer et al. (2008) studied the kinematic data of 204 PNe in the S0 galaxy NGC 1023, obtained with the PNS. The combined velocity curve from stellar and PNe data shows a maximum value of $\sim$240 km s^{-1} at 110 arcsec followed by a remarkable decline to $\sim$50 km s^{-1} at 360 arcsec. The peak in the radial velocity of NGC 1023 occurs approximately at the same position as the minimum in the velocity dispersion. Outside 110 arcsec, the galaxy is dominated by a more pressure-supported component, and the velocity dispersion increases up to 140 km s^{-1}.

This was interpreted as a signature of the complex evolutionary history of the galaxy: the inner regions with high rotation and low velocity dispersion indicate a quiescent disc formation process, while the outer parts with declining rotation and higher velocity dispersion indicate heating from a merger or strong interaction with the companion galaxy.

Fig. 2 shows a good agreement between the stellar surface brightness and PNe number density within the relatively large errors. The PNe densities are different from the original values presented in Noordermeer et al. (2008) because the completeness correction was not performed there.

The two-dimensional PNe velocity and velocity dispersion fields are derived using the PNe catalogue of Noordermeer et al. (2008) and indicate rapid rotation in the central $\approx$100 arcsec followed by a decline towards larger radii (Section A).

Approximate agreement is found between absorption-line and PNe kinematics (Fig. 7) within the error bars. The small discrepancy in the rotation curve may be caused by the high inclination of the galaxy disc ($\sim$72° according to Noordermeer et al. 2008). Stellar kinematics are taken from Debattista, Corsini & Aguerri (2002) for the major axis and Simien & Prugniel (1997) for the minor axis.

5.2.2 NGC 1344 (NGC 1340)

NGC 1344 is an E5 elliptical galaxy in the Fornax cluster. We use the stellar long-slit kinematics and the radial velocities of the 195 PNe in NGC 1344 from Teodorescu et al. (2005), who estimated a dark matter halo of $3.8 \times 10^{11}\,\mathrm{M}_\odot$ within 160 arcsec (3.5 R_e) by combining the two data sets. The PNe number density profile agrees well with the stellar surface brightness (Sikkema et al. 2007; see Fig. 2).

The PNe velocity field (see Appendix A) reaches $\sim$40 km s^{-1} and shows a misalignment of $32 \pm 27^\circ$ with respect to the photometric major axis. The absorption-line kinematics taken from Teodorescu et al. (2005) extend to 60 arcsec along the major axis. The rotation velocity reaches a maximum of $\sim$100 km s^{-1} at 60 arcsec. The PNe velocities, which are measured outside this region, show essentially no rotation (already reported in Teodorescu et al. 2005). The spatial overlap between the two systems is too small to ascertain the cause of this steep decrease in rotation. Along the minor axis both components show no rotation. The velocity dispersion profile declines from a central value of $\sim$180 to $\sim$90 km s^{-1} at 200 arcsec.

5.2.3 NGC 3379

NGC 3379 (M105) is an E1 galaxy in the Leo I group, close in projection (7 arcmin) to NGC 3384. The PNe system of NGC 3379 has been widely studied in the literature. Radial velocities are presented by Ciardullo, Jacoby & Dejonghe (1993, 29 PNe), Romanowsky et al. (2003, a preliminary sample of 109 PNe from the PNS), Sluis & Williams (2006, 54 PNe) and Douglas et al. (2007, the final sample of 191 PNe from the PNS). Also, the dynamical structure of NGC 3379 has been studied by several authors, using models derived from stellar kinematics (Kronawitter et al. 2000; Cappellari et al. 2007) or from the combination of stellar and PNe data (Romanowsky et al. 2003; Samurović & Danziger 2005; Douglas et al. 2007). The PNe kinematics at large radii show a steep decline in the velocity dispersion, which was previously interpreted as evidence for a lower content of dark matter than predicted by standard cosmological simulations.

In a recent paper, De Lorenzi et al. (2009) presented a new approach to the analysis of NGC 3379 using an N-particle model (NMAGIC; De Lorenzi et al. 2007), combining stellar and PNe kinematics. They generalized previous works by relaxing the assumption of spherical symmetry and demonstrated that, due to the strong degeneracy between radial anisotropy, intrinsic shape of the galaxy and mass distribution, the data do allow moderately massive dark matter haloes.

The stellar surface brightness and PNe number density show good agreement (see Fig. 2, confirming the analysis of Douglas et al. 2007).

In this paper we use the 191 PNe radial velocities published by Douglas et al. (2007). The smoothed two-dimensional fields are shown in Appendix A. Our smoothing technique is different from that used previously, but the general features of the kinematics derived from the two methods are consistent (in particular, the misalignment found between the photometric and kinematic major axes).

Absorption-line kinematics along the major and minor axes (Statler & Smecker-Hane 1999) agree well with the PNe data, as already shown in Romanowsky et al. (2003) and Douglas et al. (2007). The combined velocity dispersion profile decreases to $\sim$60 km s^{-1} at $\sim$210 arcsec.

5.2.4 NGC 4494

NGC 4494 is an E1 galaxy in the NGC 4565 group. Together with NGC 821 and 3379, it is the third galaxy studied in Romanowsky et al. (2003) in which the remarkable decline of the velocity dispersion radial profile was interpreted in terms of a low content of dark matter. A new detailed analysis is performed by Napolitano et al. (2008), using a catalogue with almost three times the number of detections obtained with the new PNS pipeline version described in Douglas et al. (2007). Napolitano et al. (2009) also present deep long-slit data (see Fig. C1) and new deep photometric data.

The two-dimensional fields presented in Appendix A are obtained using a different technique compared to that used in Napolitano et al. (2009). The main difference between the two velocity fields is the presence of a kinematic substructure rotating $\sim$30° off the major axis. Nevertheless, the small amplitude of this rotation ($\sim$25 km s^{-1}) is consistent with zero, if we take into account the measurement errors and the errors determined by Monte Carlo simulations ($\sim$30 km s^{-1}), as described in Section 4.3.

Absorption-line and PNe kinematics show a good agreement, except at $\sim$60 arcsec along the minor axis where the velocity

dispersion measured from the PNe is higher than that measured from the stars (see also Napolitano et al. 2009).

5.2.5 NGC 4697

NGC 4697 is an E6 galaxy in the direction of Virgo. This galaxy has 535 PNe detections by Méndez et al. (2001) and Méndez, Teodorescu & Kudritzki (2008). They constructed a spherical mass model using isotropic velocity dispersions and did not require a dark matter halo. In this data set, Sambhus et al. (2006) observed the presence of two distinct subpopulations of PNe with different luminosity functions, spatial distributions and radial velocities. The second population was particularly prominent in the brightest PNe. Therefore, De Lorenzi et al. (2008) used only a subsample of 351 PNe out of the Mendez catalogue for their new set of dynamical models, which also incorporates kinematic constraints from long-slit data. They found that a wide range of halo mass distributions were consistent with the kinematic data for the galaxy, including some with a dark matter content in agreement with cosmological merger simulations.

For this galaxy, we could not correct the PNe data for the radial incompleteness because of the lack of original images (see Fig. 2). This may explain why the PNe number density profile falls below the stellar surface brightness (Goudfrooij et al. 1994; De Lorenzi et al. 2008) in the inner regions.

We present the velocity and velocity dispersion fields of NGC 4697 in Appendix A using the subsample defined by De Lorenzi et al. (2008). A clear rotation is visible along the photometric major axis, with a peak of $\sim$90 km s^{-1} around $\sim 1\ R_{\rm e}$ and a declining profile thereafter.

Absorption-line kinematics along the major (Dejonghe et al. 1996) and minor (Binney, Davies & Illingworth 1990) axes show good agreement with the PNe kinematics.

5.2.6 NGC 5128

NGC 5128 (Centaurus A) is a nearby merger remnant classified S0pec galaxy, in the NGC 5128 group. NGC 5128 is the early-type galaxy with the largest number of PNe detections. It was first studied by Hui et al. (1995), using radial velocities of 433 PNe out to $\sim$22 kpc, and then by Peng et al. (2004), using radial velocities of 780 PNe out to $\sim$80 kpc. They found a total mass enclosed within 80 kpc of 5–6 $\times$ 10^{11} M$_{\odot}$, depending on the particular model assumed for the dark matter halo.

The more recent analysis of Woodley et al. (2007) included the radial velocities of 320 globular clusters. They obtained a mass of 1.0 $\times$ 10^{12} M$_{\odot}$ (using only PNe within 90 kpc) and 1.3 $\times$ 10^{12} M$_{\odot}$ (using only globular clusters).

In Section A, we show the two-dimensional velocity and velocity dispersion fields of NGC 5128, which are very similar to the ones presented by Peng et al. (2004). The long-slit data (Hui et al. 1995) cover only the central region of the galaxy.

5.3 Sample C

5.3.1 NGC 1316

NGC 1316 (Fornax A) is a bright S0 galaxy in the Fornax cluster. Arnaboldi et al. (1998) measured the positions and radial velocities of 43 PNe in this galaxy, computing an enclosed mass of 2.9 $\times$ 10^{11} M$_{\odot}$ within 16 kpc. Kinematic data (PNe and stellar long-slit) used in our work are taken from their paper. The relatively low number of PNe and their sparse distribution did not allow us to construct a reliable two-dimensional velocity field with our adaptive Gaussian kernel smoothing procedure. Also, the comparison with the stellar surface brightness suffers from low number statistics. In addition, the stellar long-slit data (Arnaboldi et al. 1998) do not overlap sufficiently in radius with the PNe kinematics to make a comparison. The combined velocity dispersion radial profile is relatively flat for $R > R_{\rm e}$ (see Section 6.4).

5.3.2 NGC 1399

NGC 1399 is an E1 galaxy in the centre of Fornax cluster. This galaxy has been modelled in detail by Saglia et al. (2000) using kinematic measurements from their stellar long-slit data, and globular cluster (Kissler-Patig et al. 1998) and PNe (Arnaboldi et al. 1994) radial velocities out to 100 arcsec. They found a total mass of 1.2–2.5 $\times$ 10^{12} M$_{\odot}$, consistent with the results obtained from X-ray determinations (Ikebe et al. 1996). A more detailed analysis of the PN sample was presented in Napolitano, Arnaboldi & Capaccioli (2002). They found that the PN dispersion profile, depending on the definition of outliers, is consistent with staying approximately flat at 200 km s^{-1} but also with increasing to 400 km s^{-1} outside $\sim 3R_{\rm e}$ as the globular cluster profile.

The small number of PNe (37 detections) is too low to derive reliable two-dimensional smoothed fields with our procedure. Moreover, there is no overlap between stellar and PNe data; therefore a comparison between the PNe distribution and stellar surface brightness or between PNe and stellar long-slit kinematics is not possible.

The combined velocity dispersion declines from $\sim$370 at the centre to $\sim$200 km s^{-1} at 170 arcsec ($\sim 5\,R_{\rm e}$) (Saglia et al. 2000).

5.3.3 NGC 3384 (NGC 3371)

NGC 3384 is an S0 galaxy in the Leo I group, close in projection (7 arcmin) to NGC 3379. The two galaxies have comparable systemic velocities, which makes the two PNe systems' radial velocities overlap.

Mass models of this galaxy are mostly based on stellar kinematics and are confined to the innermost regions (e.g. Gebhardt et al. 2003; Cappellari et al. 2007). There are no large catalogues of PNe radial velocities for this galaxy: Tremblay, Merritt & Williams (1995, 63 PNe), Douglas et al. (2007, 23 PNe) and Sluis & Williams (2006, 50 PNe). For the analysis in this paper, we use the catalogue of Tremblay et al. (1995). A cross-check between the Douglas et al. and Sluis & Williams catalogues is done in Douglas et al. (2007). In Tremblay et al. (1995), PNe positions are not published, therefore a cross-check with that catalogue is not possible.

The relatively low number of PNe and their sparse distribution did not allow us to construct a reliable two-dimensional velocity field or a reliable number density profile. The major axis stellar long-slit data (Fisher 1997) did not significantly overlap in radius with the PNe kinematics. This did not allow a comparison between the two data sets, but the combined velocity dispersion profile is shown in Fig. 15.

5.3.4 NGC 4406

NGC 4406 (M86) is an E3 galaxy in the Virgo cluster, near in projection to NGC 4374. Surface brightness fluctuations (Table 1) place this galaxy at a distance of 1.1 $\pm$ 1.4 Mpc closer than NGC 4374. The X-ray emitting hot gas envelopes of both galaxies appear to be interacting (E. Churazov, private communication).

NGC 4406 has a radial velocity of about $-250\,\mathrm{km\,s^{-1}}$ and is falling towards M87 from behind. The catalogue of PNe radial velocities (Arnaboldi et al. 1996) consists only of 16 detections, but this has been sufficient to constrain the velocity dispersion profile out to 11 kpc ($\sim 1.5\,R_\mathrm{e}$).

The relatively low number of PNe and their sparse distribution did not allow us to construct a reliable two-dimensional velocity field. Also, the comparison with the stellar surface brightness suffers from low number statistics.

The stellar long-slit data (Bender et al. 1994) do not overlap sufficiently with the PNe kinematics for a comparison. The combined velocity dispersion ranges between 200 and 250 $\mathrm{km\,s^{-1}}$ in the central $\sim 0.5\,R_\mathrm{e}$, and then declines to 96 $\mathrm{km\,s^{-1}}$ at 142 arcsec.

6 SAMPLE PROPERTIES: RESULTS AND DISCUSSION

In this section, we analyse the general properties of the whole galaxy sample (Table 1), combining the information from stars and PNe. In particular, we look for correlations between kinematic properties (such as the V/σ ratio and the velocity dispersion radial profile), photometric properties (such as the total luminosity, UV emission or the shape of the isophotes) and the ratio of PNe number to luminosity (α parameter). All quantities determined for this purpose in the following sections will be presented in Table 7.

6.1 The α parameter

One important aspect of the comparison between PNe and the stellar surface brightness is the evaluation of the α parameter (Jacoby 1980), which specifies the number of PNe associated with the amount of light emitted by the stellar population.

For the galaxies in the PNS data base, we compute more specifically $\alpha_{B,1.0}$, the ratio between the number of PNe down to 1 mag fainter than the PNLF bright cut-off, m^*, and the total stellar luminosity in the B band, L_B, expressed in solar units, as follows.

(i) We determine the number N_c^{TOT} of PNe brighter than $m_{80\,\mathrm{percent}}$ accounting for completeness correction factors c_R at different radii from the galaxy centre. $m_{80\,\mathrm{percent}}$ and c_R were defined in Section 3.2.

(ii) We integrate the fitted Sérsic stellar surface brightness profile in the B band over the radial range in which the PNe have been detected, giving us $L_B(R_\mathrm{PNe})$. For NGC 4374 and 5846, where the V-band profiles are available instead, we convert the result into the B band using the total extinction-corrected colour $(B-V_0)_T$ as reported in the RC3 catalogue: $(B-V_0)_T = 0.94$ for NGC 4374 and $(B-V_0)_T = 0.96$ for NGC 5846.

(iii) We compute $\alpha_{B,m^*-m_{80\,\mathrm{percent}}}$ as the ratio $N_c^{\mathrm{TOT}}/L_B(R_\mathrm{PNe})$. Uncertainties in the radial extent of the PNe detection range, in the Sérsic fit extrapolation and in the completeness corrections give us an error estimate for α.

(iv) Finally, we scale the measured $\alpha_{B,m^*-m_{80\,\mathrm{percent}}}$ to $\alpha_{B,1.0}$ by integrating over the PNLF. We have

$$\alpha_{B,1.0} = \alpha_{B,m^*-m_{80\,\mathrm{percent}}} \frac{\int_{m^*}^{m^*+1} F(m^*, m')\mathrm{d}m'}{\int_{m^*}^{m_{80\,\mathrm{percent}}} F(m^*, m')\mathrm{d}m'} \quad (9)$$

where $F(m^*, m')$ is the analytic expression of the PNLF (Ciardullo et al. 1989b), which depends only on the cut-off magnitude m^* observed in our galaxies.

For galaxies not included in our PNS data base, we use the $\alpha_{B,1.0}$ as listed by Buzzoni, Arnaboldi & Corradi (2006).

It is known that α is related to the UV emission in galaxies (Buzzoni et al. 2006). We therefore compare the $\alpha_{B,1.0}$ values to the UV excess of the sample galaxies. The latter is measured using the total FUV (1344–1786 Å) magnitude from the GALEX data base (where available) and the extinction-corrected total V magnitude from the RC3 catalogue. GALEX FUV magnitudes are corrected for extinction using the relation $A_\mathrm{FUV} = 8.376\,E(B-V)$ as in Wyder et al. (2005). Values for the colour excess $E(B-V)$ are taken from the NED data base. The $\alpha_{B,1.0}$ parameters and the $FUV-V$ colours are listed in Table 7. In Fig. 12, we plot $\alpha_{B,1.0}$ against the GALEX $FUV-V$ colours. The figure shows a clear anti-correlation: galaxies with a larger UV excess, which are the massive ellipticals, also have a smaller number of PNe per unit luminosity, $\alpha_{B,1.0}$.

Using stellar population models, Buzzoni et al. (2006) interpreted this trend as a consequence of the mean post-AGB (PAGB) core mass being smaller in massive ellipticals, which is a result of a higher rate of mass loss. If the mean PAGB core mass falls below $M_\mathrm{core} \leq 0.52\,\mathrm{M}_\odot$, one may expect a larger fraction of horizontal-branch (HB) stars to follow the AGB-*manqué* channel, i.e. the stars move directly on to the high-temperature white dwarf cooling sequence after leaving the HB, thus missing the AGB and PN phases entirely (Greggio & Renzini 1990). A larger fraction of AGB-*manqué* stars is consistent both with a lower value of $\alpha_{B,1.0}$ and with a strongly enhanced galaxy UV emission, as is observed for the more massive elliptical galaxies in the current PNe sample.

6.2 The average $V\sigma$ ratio for stellar and PNe systems

The average value of the ratio V/σ in a galaxy has traditionally been used to describe the relative importance of rotation and anisotropy for dynamical equilibrium and the shape. Usually, it has been calculated from long-slit kinematics using the formula

$$V/\sigma = V_\mathrm{max}/\sigma_0, \quad (10)$$

where V_max is the maximum value of the observed radial velocity and σ_0 is the average value of the velocity dispersion within $0.5\,R_\mathrm{e}$ (e.g. Bender et al. 1994).

Binney (2005) revisited the calculation of the average V/σ, adapting it for two-dimensional data. The new formulation is in terms of the sky-averaged values of V^2 and σ^2, weighted by the surface density. For SAURON integral-field data, this was approximated by Cappellari et al. (2007):

$$(V/\sigma)_\mathrm{stars} = \sqrt{\frac{\langle V^2\rangle}{\langle\sigma^2\rangle}} = \sqrt{\frac{\sum_i F_i V_i^2}{\sum_i F_i \sigma_i^2}}, \quad (11)$$

where the sum extends over the data points in the two-dimensional field, on isophotes up to $1\,R_\mathrm{e}$, depending on the radial extent of the data. V_i and σ_i are the velocity and velocity dispersion of the data point, and F_i is the flux associated with it.

'Classical' measurements V_max/σ_0 (equation 10) can be rescaled to the new 'two-dimensional' values by multiplying by 0.57 (Cappellari et al. 2007).

(i) *Stellar* V/σ.

Stellar $(V/\sigma)_\mathrm{stars}$ are taken from the SAURON survey (from Cappellari et al. 2007), where available. For the remaining sample galaxies in Table 1, we compute V_max/σ_0 from long-slit data using equation (10), and rescale to the two-dimensional values by multiplying with 0.57. Errors are taken to be 0.03 for SAURON values, or are computed using error propagation (on equation 10) and are also rescaled by 0.57.

Table 7. Measured parameters for the sample galaxies.

Name (NGC) (1)	$\sigma_{\rm LAST}$ (km s^{-1}) (2)	$\sigma_{1.0}$ (km s^{-1}) (3)	$\sigma_{5.0}$ (km s^{-1}) (4)	$\frac{\sigma_{\rm MIN}}{\sigma_{1.0}}$ (5)	$V_{\rm rms,LAST}$ (km s^{-1}) (6)	$V_{\rm rms,1.0}$ (km s^{-1}) (7)	$V_{\rm rms,5.0}$ (km s^{-1}) (8)	$\frac{V_{\rm rms,MIN}}{V_{\rm rms,1.0}}$ (9)	$V/\sigma_{\rm PNe}$ (10)	$V/\sigma_{\rm STARS}$ (mag, mag) (11)	m^*, $m_{80\,\rm percent}$ ($10^{-9}\,L_{B,\odot}$) (12)	$\alpha_{B,1.0}$ (mag) (13)	(FUV-V) (14)	M_*/L_B (15)	M_* ($10^{10}\,{\rm M}_\odot$) (16)
821	51 ± 18	167	76	0.31	56 ± 18	181	66	0.31	0.31 ± 0.02	0.26 ± 0.03	27.4, 28.6	$11. \pm 4.$	9.1± 0.2	$7.1^{+1.9}_{-2.0}$	14.7 ± 4.0
1023	119 ± 29	110	79	0.54	123 ± 29	209	147	0.59	1.18 ± 0.03	0.34 ± 0.03	25.8, 27.3	2.6 ± 1.5	7.6± 0.1	–	–
1316	152 ± 31	152	152	1.00	179 ± 31	184	179	0.97	0.42 ± 0.13	0.50 ± 0.12	-, -	$0.79 \pm 0.12^{(a)}$	7.2± 0.2	$3.9^{+0.8}_{-1.1}$	54.4 ± 13.2
1344	109 ± 23	148	109	0.73	133 ± 23	173	142	0.77	0.20 ± 0.02	0.33 ± 0.12	-, -	$4.45 \pm 0.2^{(a)}$	7.6± 0.1	–	–
1399	198 ± 47	240	198	0.83	213 ± 47	243	213	0.88	0.64 ± 0.23	0.06 ± 0.03	-, -	$1.25 \pm 0.2^{(a)}$	5.9± 0.1	$10.4^{+3.3}_{-2.7}$	48.1 ± 13.7
3377	77 ± 21	67	77	0.75	64 ± 21	110	64	0.58	0.37 ± 0.03	0.49 ± 0.03	25.2, 27.0	$6. \pm 5.$	–	–	–
3379	46 ± 21	153	69	0.30	46 ± 21	162	77	0.29	0.18 ± 0.02	0.14 ± 0.03	25.5, 26.5	24 ± 10	–	$8.4^{+2.8}_{-2.4}$	13.9 ± 4.3
3384	72 ± 20	63	72	0.93	146 ± 20	162	157	0.80	1.20 ± 0.20	0.44 ± 0.03	-, -	$9.5 \pm 2.5^{(b)}$	–	$3.2^{+0.6}_{-0.6}$	3.7 ± 0.7
3608	169 ± 43	130	169	0.99	191 ± 43	141	191	0.98	0.45 ± 0.03	0.05 ± 0.03	27.1, 28.0	2.1 ± 1.1	7.6± 0.1	–	–
3608N	107 ± 33	102	107	0.55	134 ± 33	134	134	1.00	0.65 ± 0.06	0.05 ± 0.03	27.2, 28.0	1.7 ± 0.8	7.6± 0.1	–	–
4374	207 ± 33	215	207	0.96	208 ± 33	216	208	0.96	0.16 ± 0.01	0.03 ± 0.03	26.9, 28.0	5.0 ± 1.0	7.5± 0.1	–	–
4406	96 ± 26	147	96	0.65	219 ± 26	219	219	1.00	0.80 ± 0.17	0.09 ± 0.04	-, -	$3.2 \pm 0.5^{(c)}$	7.2± 0.1	$8.1^{+2.4}_{-2.2}$	52.4 ± 14.9
4494	46 ± 15	106	63	0.44	44 ± 15	122	66	0.36	0.18 ± 0.02	0.25 ± 0.02	26.0, 27.0	$10. \pm 3.$	–	–	–
4564	56 ± 15	70	58	0.79	58 ± 15	163	93	0.36	1.02 ± 0.08	0.58 ± 0.03	26.3, 27.8	1.6 ± 1.5	6.9± 0.1	–	–
4697	92 ± 20	154	92	0.60	106 ± 20	180	106	0.59	0.32 ± 0.02	0.41 ± 0.14	-, -	$3.8 \pm 0.3^{(a)}$	7.9± 0.1	$6.7^{+2.3}_{-1.7}$	15.0 ± 4.5
5128	69 ± 69	132	89	0.52	118 ± 25	147	133	0.80	0.48 ± 0.02	0.13 ± 0.11	-, -	$12.5 \pm 0.6^{(a)}$	–	–	–
5846	170 ± 30	210	170	0.81	174 ± 30	219	174	0.79	0.12 ± 0.01	0.03 ± 0.03	27.3, 28.3	1.01 ± 0.17	6.7± 0.1	$11.1^{+3.7}_{-3.2}$	52 ± 16

Notes. Col. 1: galaxy name. NGC 3608N refers to the results obtained using half of the PNe sample, as explained in Section 5.1.3. Col. 2: outermost value of the velocity dispersion as given by the fit. Col. 3: velocity dispersion at $1R_{\rm e}$, as given by the fit. Col. 4: velocity dispersion at $5R_{\rm e}$, as given by the fit. Col. 5: minimum value of the velocity dispersion as given by the fit, scaled by $\sigma_{1.0}$ (from Col. 3). Col. 6: outermost value of $V_{\rm rms}$ as given by the fit. Col. 7: $V_{\rm rms}$ at $1R_{\rm e}$, as given by the fit. Col. 8: $V_{\rm rms}$ at $5R_{\rm e}$, as given by the fit. Col. 9: minimum value of $V_{\rm rms}$ as given by the fit, scaled by $\sigma_{1.0}$ (from Col. 7). Col. 10: average value of V/σ for the PNe component. For the data from two-dimensional field, equation (11) was used. For the data from major axis kinematics, equation (10) was used and values have been multiplied by 0.57 to rescale them to the two-dimensional case, as done by Cappellari et al. (2007). Col. 11: average value of V/σ for the stellar component, calculated with equation (10) on long-slit data and corrected by the factor of 0.57, or using the value reported by Cappellari et al. (2007) if available. Col. 12: bright cut-off magnitude and $m_{80\,\rm percent}$ computed for the galaxies in Fig. 2. Col. 13: the $\alpha_{B,1.0}$ parameter computed using the PNS data. Values marked by $^{(a)}$are from Buzzoni et al. (2006), $^{(b)}$from Ciardullo, Jacoby & Ford (1989a) and $^{(c)}$from Jacoby, Ciardullo & Ford (1990). Total V-band photometry for NGC 4374 and 5846 has been converted into B band using $(B-V) = 0.94$ for NGC 4374 and $(B-V) = 0.96$ for NGC 5846 (values taken from RC3). Col. 14: difference between the extinction-corrected magnitudes in the FUV (from GALEX) and V band (from RC3). The symbol '−' means that the galaxy is not present in the GALEX data base. Col. 15: mass-to-light ratio from single stellar population models listed in Napolitano et al. (2005). The symbol '-' means that the measurement is not available. Col. 16: total stellar mass computed from the mass-to-light ratio (Col. 15), B_T and distance from Table 1.

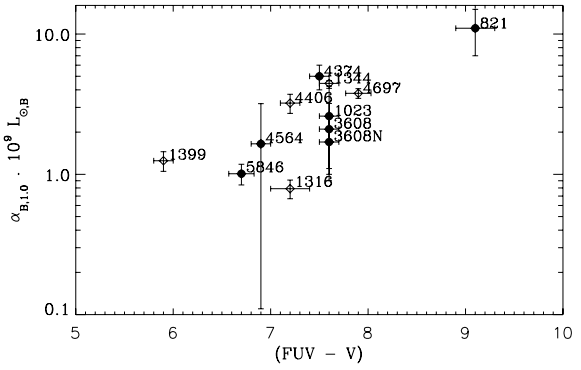

Figure 12. Correlation between the $\alpha_{B,1.0}$ parameter and $FUV - V$ colour, measured from total extinction-corrected magnitudes FUV (from GALEX) and V (from RC3). Filled circles: sample galaxies for which α is calculated from our PNS data, according to the prescription given in Section 6.1. Open diamonds: sample galaxies for which α values are taken from Buzzoni et al. (2006).

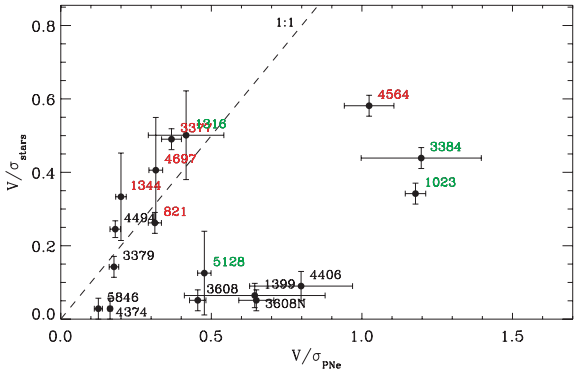

Figure 13. Comparison between the two-dimensional averaged values of the V/σ ratio for the stellar and PNe systems. The 1:1 relation is shown by a dashed line. Black labels refer to round ellipticals ($\leq$E3), red labels refer to flattened ($\geq$ E4) ellipticals and green labels refer to S0 galaxies.

(ii) *PNe* V/σ.

We compute V/σ for the PNe system using the smoothed two-dimensional fields (calculated in Section 4.2), summing over the positions of the detected PNe:

$$(V/\sigma)_{\rm PNe} = \sqrt{\frac{\langle V^2\rangle}{\langle\sigma^2\rangle}} = \frac{\sqrt{\sum_P \frac{1}{c_{\rm R}}\tilde{V}(x_P, y_P)^2}}{\sum_P \frac{1}{c_{\rm R}}\tilde{\sigma}(x_P, y_P)^2}. \quad (12)$$

This implicitly incorporates the weighting by the local stellar surface density, which was shown earlier to be proportional to the PNe number density if the completeness correction factor $c_{\rm R}$ (interpolated for x_p, y_p) is taken into account: equation (12) weights every region according to the completeness-corrected number of PNe in the region (see Section 3.2). Note that equation (12) is an average over the whole PNe field, and therefore probes a much larger region of the galaxy than the value for the stars, which was confined to within 1 $R_{\rm e}$.

For a few galaxies, the number of PNe detections is too small for a reliable determination of the two-dimensional velocity fields. For these galaxies, we use the PNe mean velocities and velocity dispersions in bins along the major axis as given in the respective paper from which the data were taken. We then take the maximum of these mean velocities and the average of all the velocity dispersion values to obtain a major-axis V/σ value analogous to the classical formula given in equation (10), but not confined to within 0.5 $R_{\rm e}$. These values are then rescaled to the two-dimensional case by multiplying by 0.57.

In Fig. 13, we compare these stellar and PNe V/σ, providing information on how the dynamics of a galaxy change from the inner to the outer region. From this figure, we can see that many galaxies (nearly 50 per cent) have $(V/\sigma)_{\rm PNe} > V/\sigma$, while for the rest, the two values are similar. Fig. 13 also shows the differences between the distributions of flattened ($\geq$E4) ellipticals (red), round ($\leq$E3) ellipticals (black) and S0s (green). This shows the following.

(i) Three of the galaxies (NGC 1023, NGC 3384 and NGC 4564) have large inner V/σ and even larger $(V/\sigma)_{\rm PNe}$ in the halo. The first two are S0 galaxies while the third exhibits S0-like properties (see Section 5.1.5). In these systems, the (V/σ) rises from the centre to the disc-dominated region, like in the discy elliptical galaxies studied by Rix et al. (1999).

(ii) For flattened (NGC 821, NGC 1344, NGC 3377 and NGC 4697) and rotating round galaxies (NGC 3379 and NGC 4494) in the sample, the inner and outer values for V/σ are equal to within the errors.

(iii) Galaxies with a small V/σ in the inner parts may have either small (NGC 4374 and 5846) or larger (best exemplified by NGC 5128 and with larger uncertainties, NGC 1399 and 3608) V/σ in the outer parts.

6.3 The $\lambda_{\rm R}$ radial profile for stellar and PNe systems

In Emsellem et al. (2007), a kinematic classification scheme for galaxies is proposed based on the $\lambda_{\rm R}$ profile, which measures the importance of rotation as a function of radius and is related to the angular momentum per unit of mass within R:

$$\lambda_{\rm R} = \frac{\sum(R_i F_i |V_i|}{\sum(R_i F_i \sqrt{V_i^2 + \sigma_i^2}}, \quad (13)$$

where the sum includes data points within R. Based on the $\lambda_{\rm R}$ profile within $\sim 1R_{\rm e}$, galaxies can be divided into two main groups (Emsellem et al. 2007).

(i) Galaxies with $\lambda_{\rm R} > 0.1$ are defined as *fast rotators*. These have a small misalignment between the photometric and kinematic major axes, and have rising $\lambda_{\rm R}$ profiles.

(ii) Galaxies with $\lambda_{\rm R} < 0.1$ are defined as *slow rotators*. They exhibit a range of misalignments between the photometric and kinematic major axes and have flat or decreasing $\lambda_{\rm R}$ profiles.

To extend their analysis to the outer haloes of elliptical galaxies (beyond several $R_{\rm e}$), we calculate the $\lambda_{\rm R}$ profiles using the PNe kinematics for the sample galaxies. For galaxies in which the two-dimensional field is available, we use equation (13) to sum over the velocity and velocity dispersion field values at the positions of the PNe, using the factor $1/c_{\rm R}$ as the weight instead of the flux values F_i. This incorporates the weighting by the stellar surface density as discussed in the case of equation (12). For galaxies in which the kinematics are available only along the major axis, we use equation (13) where the sum is meant to be extended only along the major axis, F_i are extracted from the extrapolation of the stellar surface brightness and the 0.57 correction is applied. In Fig. 14, we show the profiles derived using the stellar kinematics (which we used to separate between fast and slow rotators, to be consistent with previous works) and the PNe kinematics. To simplify matters,

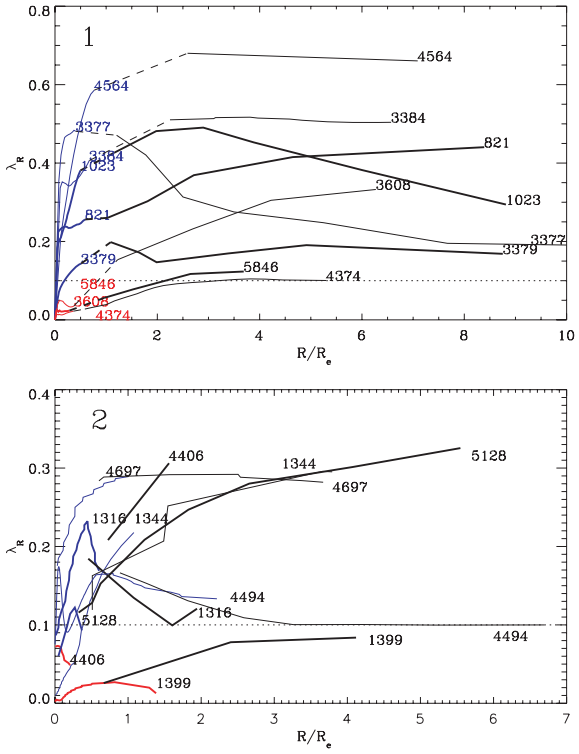

Figure 14. Panel 1: radial λ_R profiles for galaxies common to our sample and the SAURON sample. Panel 2: radial λ_R profiles for galaxies in our sample, which are not in the SAURON sample. Red and blue solid lines: λ_R profiles computed from the stellar kinematics for slow and fast rotators, respectively (those in Panel 1 were kindly provided by Eric Emsellem). Black solid lines: λ_R profiles extracted from the PNe kinematics. Dashed black lines in Panel 1 connect the last SAURON data point with the first PNe data point, to guide the eye on the plot. These lines were not plotted in Panel 2 to avoid overcrowding. The dotted line ($\lambda_R = 0.1$) separates fast and slow rotator regions. In both panels, some radial λ_R profiles are shown with thicker lines for clarity.

Fig. 14 is divided into two panels separating galaxies for which the stellar λ_R is available from the SAURON data, from the remaining galaxies in our sample. Several results emerge from this figure, reflecting the changes in both the rotation and velocity dispersion profiles.

(i) In some galaxies, there is a marked change in the behaviour of λ_R at radii larger than 1 or 2 effective radii compared to that in the central regions. In the case of NGC 1023, NGC 1316, NGC 3377 and NGC 4494, after the initial increase of λ_R (as observed in the majority of fast rotators within $1R_e$) the profiles drop, and they reach the 'slow rotator' region (NGC 1316 and 4494) or arrive close to it (NGC 1023, NGC 3377). According to Krajnović et al. (2008), the majority of fast rotators have structures with disc-like kinematics, which are responsible for the high values of λ_R. In these four fast rotators, the observed outer decrease in λ_R may imply that the light associated with the disc structure fades towards larger radii.

(ii) In the galaxies of the sample, which are slow rotators according to the SAURON classification, the λ_R profiles grow slowly to values of 0.1–0.3, thus entering the 'fast rotator' regime (NGC 3608, NGC 5846 and partially for NGC 4374). A larger increase is visible in NGC 4406, but the small number of PNe for this galaxy makes its λ_R uncertain. The outward rise of λ_R for NGC 1399 is slower; this galaxy remains below the 'slow rotator' demarcation line.

(iii) The remaining galaxies in the sample are 'fast rotators' throughout the radial range probed. The λ_R profile either rises or stays almost flat throughout.

The large radial extent of the PNe data enables us to follow the rotation properties of elliptical galaxies out into the halo, providing new constraints on the processes involved in the formation of these galaxies (see Section 6.6).

Although the kinematics of the stars within R_e as measured by SAURON (and most traditional long-slit studies) reflect half of the total stellar luminosity and mass, the same is not true for the total stellar angular momentum. As discussed in Appendix D, these stars may represent only ∼10 per cent of the galaxy's angular momentum, and an adequate global rotational picture of the galaxy requires observations to $\sim 5\,R_e$.

6.4 The shape of the velocity dispersion and V_{rms} radial profiles

In order to obtain a general overview of the shapes of the velocity dispersion profiles σ (R) for our sample galaxies, we first parametrized the major axis profiles with suitable functions. There is no universally valid function for all the observed profiles, so we experimented with various *ad hoc* functions and selected the one that best matched the observations for each galaxy. The fitted velocity dispersion profiles were then scaled by the effective radius (values from Table 1) and normalized to the value of the velocity dispersion at $1.0R_e$. We did not use the central velocity dispersion value for the normalization [i.e. $\sigma(R = 0)$] because it might be artificially boosted by the presence of a central supermassive black hole or an unresolved central velocity gradient. We performed a similar parametrization for the rotation profiles to compute the V_{rms} velocity profiles, where $V^2_{rms} = \sigma^2 + V^2$.

According to the normalized V_{rms} profiles shown in Fig. 15, galaxies fall into two main groups. The larger part of the sample shows a slightly decreasing profile from the centre outwards. The second group of galaxies (NGC 821, NGC 3377, NGC 3379, NGC 4564, NGC 4494, NGC 4697) show strongly decreasing V_{rms} profiles. NGC 1023 appears to be anomalous in that its V_{rms} increases initially before falling steeply. This reflects the strong rotation in the disc of the galaxy combined with a steep central drop in the velocity dispersion profile (Fig. 7; see also Noordermeer et al. 2008). For NGC 3608, the apparent increase in the V_{rms} profile is doubtful because of the possible contamination of PNe from NGC 3607 and the large errors associated with the velocity and velocity dispersion measurements (Fig. 7); the radial profile of NGC 3608N (see Section 5.1.3) does not show anomalies, and belongs to the first group.

A greater variety of trends are visible in the velocity dispersion profiles, reflecting a larger variance in the individual contributions of ordered and random motions to the V_{rms}, e.g. due to the strong disc component in galaxies such as NGC 3377. There are galaxies in which the velocity dispersion remains high (i.e. the drop in velocity dispersion is less than 50 per cent of the normalization value); those, which exhibit a big drop (i.e. the last value of dispersion is less than 50 per cent of the central value) and those that show an increase towards large radii, as in the case of NGC 1023, NGC 3377 and NGC 3608. In NGC 3608, the observed increase is again doubtful. In the case of NGC 4406, the massive drop is based on the results

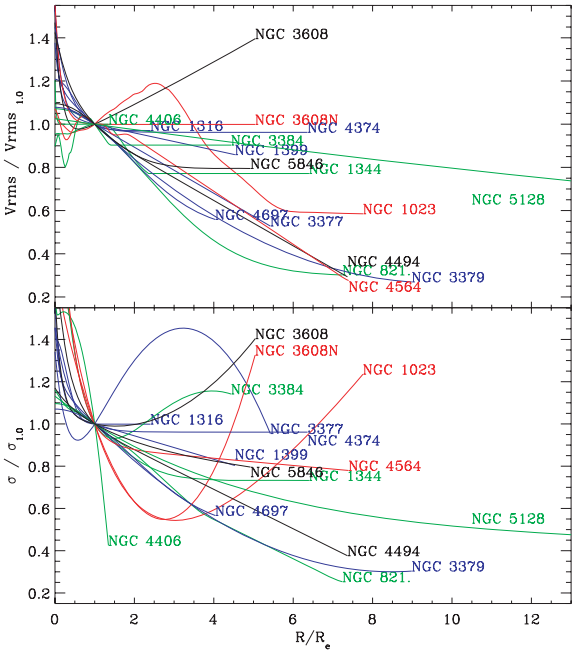

Figure 15. Comparison between radial profiles of $V_{\rm rms}$ (top panel) and velocity dispersion (bottom panel) of the sample galaxies, obtained by combining the stellar and PNe kinematics along the major axis. Profiles have been scaled to the effective radius and normalized to their value at $1.0R_{\rm e}$. Colours are chosen in order to highlight the contrast between lines and thus better distinguish different profiles.

derived from a small number of PNe velocities, which show an associated increase in rotation velocity.

6.5 Correlations between kinematic, photometric and morphological properties of the sample galaxies

In this section, we study the relations between some physical properties of early-type galaxies and their kinematic properties at large radii.

In the left-hand panels of Fig. 16, we show how the outermost values of $V_{\rm rms}$($V_{\rm rms,LAST}$, measured from the ad hoc fitted profiles of Fig. 15) are related to the galaxy's X-ray luminosity, total B-band luminosity, mean isophotal shape parameter $\langle a_4\rangle$, mean $(V/\sigma)_{\rm PNe}$ measured from the PNe data and $\alpha_{B,1.0}$ parameter. In the right-hand panels of Fig 16, we show similar plots, using the minimum value of $V_{\rm rms}$ normalized by the value at $1.0R_{\rm e}$, $V_{\rm rms,MIN}/V_{\rm rms,1.0}$ in place of $V_{\rm rms,LAST}$.

Similarly, Fig. 17 shows corresponding plots with the last values of the velocity dispersion ($\sigma_{\rm LAST}$, measured from the ad hoc fitted profiles of Fig. 15) and $\sigma_{\rm MIN}/\sigma_{1.0}$, the minimum value of velocity dispersion normalized by the velocity dispersion at $1.0R_{\rm e}$.

The outermost values of $V_{\rm rms}$ and velocity dispersion characterize their typical values in the galaxy halo and therefore also the galaxy mass, while the ratios between their minima and their values at $1.0R_{\rm e}$ give a measure of how much these profiles fall towards the outer radii.

We note that using the values of $V_{\rm rms}$ and velocity dispersion at a fixed radius of 5 $R_{\rm e}$ in these figures, instead of their outermost values, gives very similar results. Also, plotting the physical parameters against the logarithmic gradient of $V_{\rm rms}$ or velocity dispersion between $1R_{\rm e}$ and $5R_{\rm e}$ results in similar trends as shown in the right-hand parts of Figs 16 and 17. For reference, the $V_{\rm rms}(5R_{\rm e})$ and $\sigma(5R_{\rm e})$ interpolated from the parametric fits are given in Table 7.

From Figs 16 and 17, we note that more luminous galaxies tend to have larger values of $V_{\rm rms,LAST}$ and $\sigma_{\rm LAST}$. This is not surprising given that luminosity, $V_{\rm rms}$ and velocity dispersion are known to be related to the galaxy mass. What is new here is that we are exploring a larger radial range, probing the relation for the galaxy halo. We note also that galaxies with higher $V_{\rm rms,LAST}$ and $\sigma_{\rm LAST}$ tend to have only boxy profiles ($a_4 < 0$), while galaxies with low values of $V_{\rm rms,LAST}$ and $\sigma_{\rm LAST}$ have a wider range of shapes ($-1 < a_4 < 2$). This is also a reflection of the known trend for massive ellipticals to be more boxy in shape (e.g. Bender et al. 1989). Napolitano et al. (2005) have also found the a_4 and other galaxy parameters (luminosity, stellar mass and central surface brightness profile) to correlate with the mass-to-light ratio gradients, showing that there might be a link between the galaxy structural parameters and the total mass of the galaxies.

In addition, galaxies which have the highest peaks in the $\lambda_{\rm R}$ parameter (NGC 1023, NGC 3384 and NGC 4564; see Fig. 14) have fainter B magnitudes and higher values of mean $(V/\sigma)_{\rm PNe}$. Moreover, galaxies with higher $V_{\rm rms,LAST}$ and $\sigma_{\rm LAST}$ have smaller $\alpha_{B,1.0}$ values (i.e. less PNe per unit luminosity). As discussed in Section 6.1, this is probably a consequence of massive early-type systems harbouring a larger proportion of stars on the HB that do not enter the PN stage. The correlation between $\alpha_{B,1.0}$ and σ was already explored by Buzzoni et al. (2006), using the central velocity dispersion measurements.

We see in the right-hand panels of Figs 16 and 17 that these relations still hold if we replace $V_{\rm rms,LAST}$ with the normalized minimum of $V_{\rm rms}$ (i.e. $V_{\rm rms,MIN}/V_{\rm rms,1.0}$) and if we replace $\sigma_{\rm LAST}$ with the normalized minimum velocity dispersion (i.e. $\sigma_{\rm MIN}/\sigma_{1.0}$), even if the scatter is larger.[5] This is a consequence of more massive galaxies having preferentially larger values of $V_{\rm rms,LAST}$, $\sigma_{\rm LAST}$ and flatter profiles of $V_{\rm rms}$ and velocity dispersion.

In Fig. 18, we plot the total stellar mass M_* computed for a subsample of galaxies as a function of $V_{\rm rms,LAST}$, $V_{\rm rms,MIN}/V_{\rm rms,1.0}$, $\sigma_{\rm LAST}$, $\sigma_{\rm MIN}/\sigma_{1.0}$ and the $\alpha_{B,1.0}$ parameter. The stellar mass is computed using the total B luminosity from Table 1 and the mass-to-light ratio in the B band listed in Napolitano et al. (2005) (where available). As expected from Figs 16 and 17, M_* correlates with the α parameter, $V_{\rm rms,LAST}$, and with $\sigma_{\rm LAST}$, although with larger scatter.

The general message we learn from Figs 16–18 is that galaxies with higher $V_{\rm rms,LAST}$, and higher $\sigma_{\rm LAST}$ and flatter profiles (i.e. higher $V_{\rm rms,MIN}/V_{\rm rms,1.0}$ and higher $\sigma_{\rm MIN}/\sigma_{1.0}$) tend to be the more luminous, more massive galaxies, are more pressure supported at large radii (i.e. $V/\sigma_{\rm PNe} \leq 1$), with boxy isophotes (i.e. $a_4 < 0$), and tend to form less PNe. These results extend the picture described by Bender et al. (1989) based on stellar kinematics within 1 $R_{\rm e}$ and of Buzzoni et al. (2006), to larger radii.

In Figs 16 and 17, we also differentiate between fast rotators, fast rotators with a declining $\lambda_{\rm R}$ profile in the halo, slow rotators and slow rotators with $\lambda_{\rm R} > 0.1$ in the halo. On average, fast rotators fall on the left-hand side of the plots (i.e. they have lower values of $V_{\rm rms,LAST}$, $\sigma_{\rm LAST}$ and more declining profiles) while slow rotators fall on the right-hand side of the plots (i.e. they have higher values of $V_{\rm rms,LAST}$, $\sigma_{\rm LAST}$ and flatter profiles). This is a reflection in the halo kinematics that fast (slow) rotators are on average less (more)

[5] Normalization at $0.1R_{\rm e}$ or $0.5R_{\rm e}$ gives similar results.

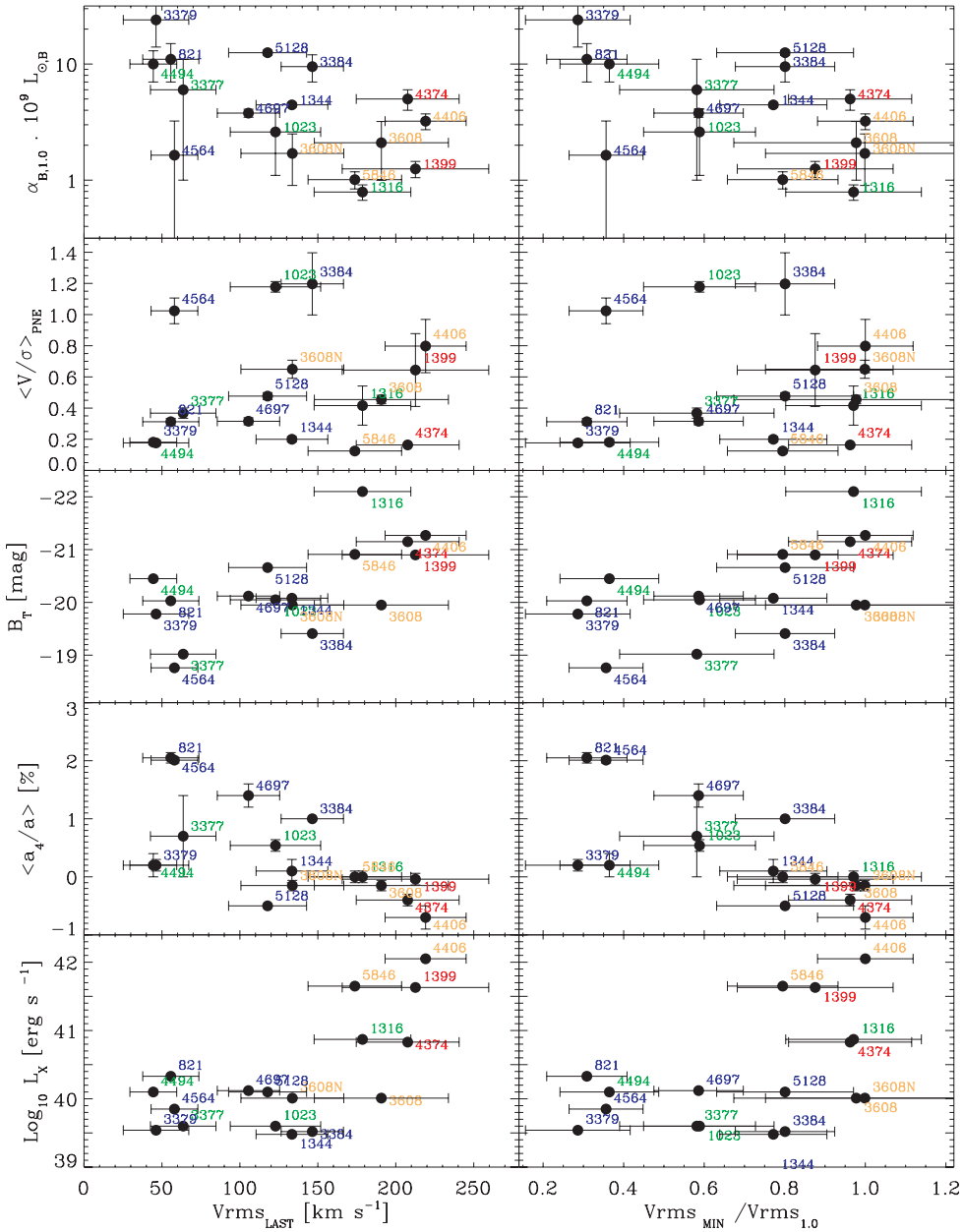

Figure 16. Halo kinematics versus other physical parameters. Left-hand panels: $V_{\rm rms,LAST}$ values for the sample galaxies plotted versus total X-ray luminosity, a_4 shape coefficient, total extinction-corrected B magnitude, mean $(V/\sigma)_{\rm PNe}$ and $\alpha_{B,1.0}$. Blue: fast rotators; green: fast rotators with a declining λ_R; red: slow rotators; orange: slow rotators with $\lambda_R > 0.1$ in the outer parts. For galaxies not listed in Table 3, the a_4 is taken from Bender et al. (1989) for NGC 4406, from Goudfrooij et al. (1994) for NGC 1399 and from Napolitano et al. (2005) and references therein for the others. Right-hand panels: same as the left-hand panels, but for the normalized minimum of $V_{\rm rms}$.

massive and have more discy (boxy) isophotes (Emsellem et al. 2007).

It is also interesting that slow rotators with $\lambda_R > 0.1$ in the outer haloes on average are located between fast and slow rotators in Figs 16 and 17, as if they represent a link between the two classes.

6.6 Comparison with galaxy formation models

The results presented in Sections 4 and 6 on the outer-halo kinematics of our sample galaxies provide new constraints for models of elliptical galaxy formation. Most of the merger simulation papers to date compare their remnants to data within an effective radius or so, but there are a few predictions for the kinematics at larger radii.

Line-of-sight velocity fields for binary disc merger remnants are published in Jesseit et al. (2007). The progenitor galaxies in these simulations include pure stellar discs as well as discs containing 10 per cent of their mass in gas. Some 3:1 mergers with gas lead to remnants showing velocity fields with rapid rotation (e.g. their remnant 31GS19), with a peak velocity at 2–3 R_e, similar to the case of NGC 1023. Strong misalignments such as observed in NGC 821 are more characteristic of the 1:1 merger remnants (both dry and gas-rich, e.g. 11C10/11S8), which also include slowly rotating remnants with radially increasing rotational support (e.g. 11C6). Their models also include one which shows a ring-like depression of the velocity dispersion at $R \simeq 0.5R_e$ associated with a corresponding increase in h_4 (11S2), somewhat similar to the case of

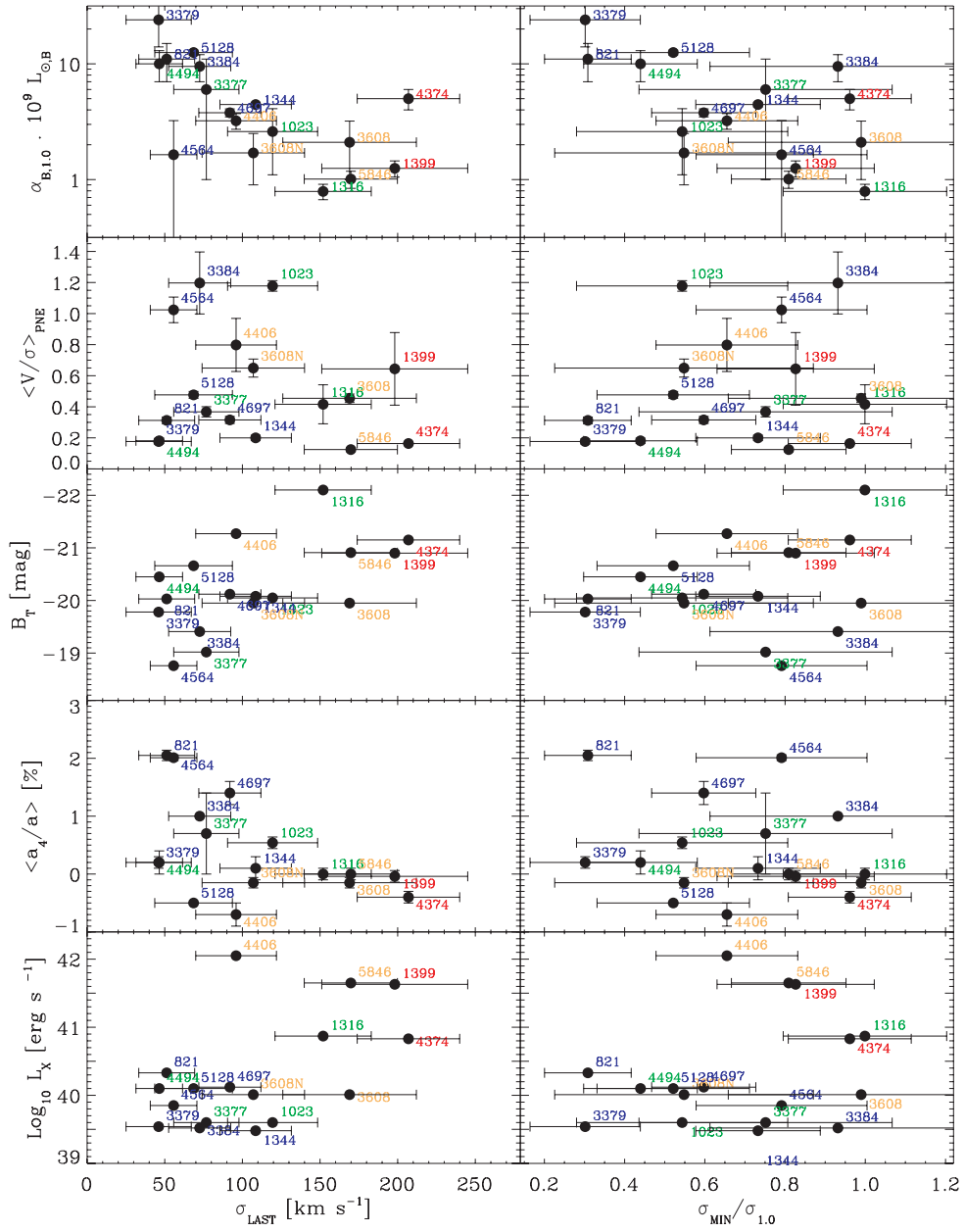

Figure 17. Same as Fig. 16, but for $\sigma_{\rm LAST}$ (left-hand panels) and $\sigma_{\rm MIN}/\sigma_{1.0}$ (right-hand panels).

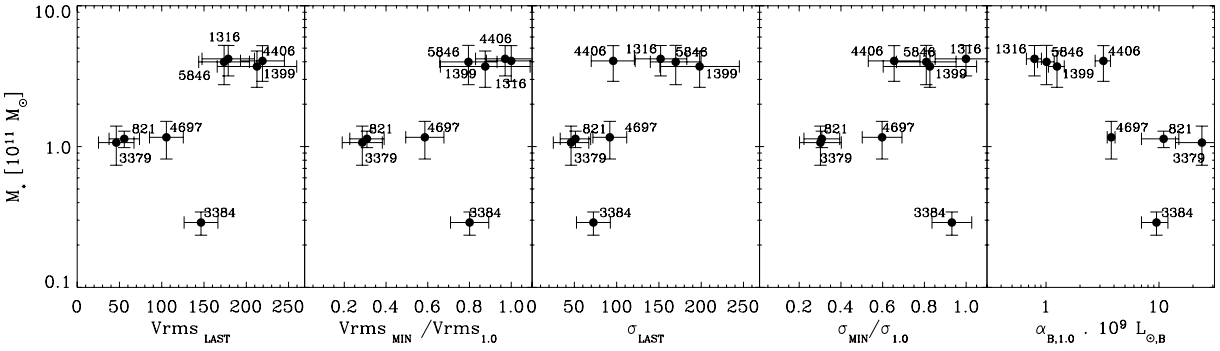

Figure 18. Correlation between total stellar mass and $V_{\rm rms}$, $V_{\rm rms}/V_{\rm rms,1.0}$, $\sigma_{\rm LAST}$, $\sigma_{\rm MIN}/\sigma_{1.0}$ and the α parameter.

NGC 3379 (see De Lorenzi et al. 2008b). Its velocity dispersion profile decreases by a factor of ∼2 from the centre out to $\sim 1.5R_e$. This model originated from a merger of two disc galaxies with spin axis perpendicular to the orbital plane. Overall, the projected kinematics of the merger remnants analysed by Jesseit et al. (2007) show a variety of features seen also in our data. A more careful comparison including several diagnostics (V/σ values, λ_R-profiles, velocity fields, dispersion profiles) would clearly be profitable.

Mean rotation and velocity dispersion profiles are shown by Naab et al. (2006) for a 3:1 merger remnant from the same set of simulations, out to $4R_e$. The kinematics of this object are characterized by rapid rotation and a falling dispersion profile (by a factor of ∼1.5), leading to a major axis V/σ profile increasing to $V/\sigma \simeq 2$ at 2–4 R_e. Only the S0 galaxies and NGC 4564 in Fig. 13 reach these values. By contrast, the M_* galaxies formed in a cosmological setting (described in Naab et al. 2007) rotate more slowly and are characterized by $V/\sigma \lesssim 0.5$ with similar values in the halo and the central parts (disregarding the counter-rotating core seen in one of the remnants). This is more typical for the slowly rotating galaxies in Figs 13 and 14.

The kinematics of the luminous haloes of isolated galaxies are investigated by Abadi et al. (2006). The outer haloes of these systems are predominantly made of stars accreted during previous merger events. These haloes have near-spherical triaxial density distributions, strongly increasing radial anisotropy and correspondingly falling line-of-sight velocity dispersion profiles (by more than a factor of 2 out to 0.1 times their virial radius). Our data probe only partially into these haloes, but it is possible that some of the strongly falling dispersion profiles in Fig. 15 are related to such accreted haloes. On the other hand, the galaxies in our sample with slowly falling dispersion profiles or those with twisting (NGC 3377) or misaligned rotation (NGC 821) may not be easily reconciled with these models.

Oñorbe et al. (2007) studied the properties of elliptical-like galaxies generated in self-consistent hydrodynamical simulations. These galaxies resemble the characteristics of slow rotators, i.e. are massive spheroidal systems without extended disc components and very low (cold) gas content. Their velocity dispersion profiles (normalized at $1R_e$) are generally flat or slightly declining, with values of $\sigma_{MIN}/\sigma_{1.0}$ larger than 0.7 out to $6R_e$. These values are consistent with what we observe for the haloes of slow rotators (see Fig. 17). Galaxies in our sample with more steeply declining velocity dispersion profiles are generally fast rotators, which are not included in the Oñorbe et al. (2007) simulations.

In summary, we expect that more detailed comparisons between data as presented in this paper and the halo kinematics predicted by galaxy formation models will shed new light on the merger formation histories of elliptical galaxies.

7 SUMMARY

We explored the outer-halo kinematics and properties of early-type galaxies using the PNe data available for a sample of 16 objects. Out of the sample, six new catalogues with positions, radial velocities and magnitudes of PNe are presented for the first time (*sample A*, namely NGC 821, NGC 3377, NGC 3608, NGC 4374, NGC 4564 and NGC 5846).

We compared the radial distribution of PNe with the stellar surface brightness profiles, for all galaxies in *sample A*, and for galaxies in *sample B*, which have extended photometry available from the literature (NGC 1023, NGC 1344, NGC 3379, NGC 4494 and NGC 4697). We found the following.

(i) The PNe number density profile follows the stellar surface brightness profile in all the galaxies in which we have a spatial overlap between the stellar light and the PNe counts.

(ii) In the galaxies in which we do not have a spatial overlap, the PNe counts follow the extrapolation of the stellar surface brightness profile.

(iii) For the galaxies with a FUV magnitude measured with GALEX, we confirmed results from previous studies that the total number of PNe per unit luminosity ($\alpha_{B,1.0}$ parameter) is related to the UV colour excess (i.e. galaxies with higher UV emission tend to have fewer PNe).

We then determined smoothed two-dimensional velocity and velocity dispersion fields using an adaptive Gaussian kernel, for the galaxies in *sample A* and in *sample B* (namely NGC 1023, NGC 1344, NGC 3379, NGC 4494, NGC 4697 and NGC 5128). We compared the PNe kinematics with absorption-line kinematics available in the literature. For NGC 3377, NGC 4374 and NGC 4494, new long-slit data were presented. The kinematic analysis showed the following.

(i) Rotation of the PNe system is observed in the majority of the studied galaxies.

(ii) There is a good agreement between the absorption-line and PNe kinematics along the major and minor axes.

We combined the PNe and absorption-line kinematics along the photometric major axis for all 16 galaxies in our sample, extracting the information from the two-dimensional fields where available. This allowed us to probe their kinematics much further out than with the use of stellar kinematics alone (usually limited to the innermost 1–2 R_e). This gave the following results.

(i) In several fast-rotator galaxies, kinematic twists and misalignments are observed at large radii, which are not seen in the SAURON data within R_e (NGC 821, NGC 3377 and, marginally, NGC 3379).

(ii) The average V/σ of the stellar component (which probes the kinematics in the inner 0.5–1 R_e) is equal to or lower than the average value computed for the PNe (which probes the kinematics for $R > 2R_e$). This indicates that for a fraction of galaxies, the kinematics become increasingly supported by rotation in the outer parts.

(iii) The radial profiles of the λ_R parameter (related to the angular momentum per unit mass) show a more complex radial dependence when their values in the halo region are taken into account. While the majority of fast rotators remain so in their haloes, the λ_R profiles of slow rotators grow slowly to values of 0.1–0.3, therefore requiring a slight modification to the classification scheme proposed by Emsellem et al. (2007) (NGC 3608, NGC 4374 and NGC 5846). Some fast rotators, however (NGC 1316, NGC 1023, NGC 3377 and NGC 4494), have λ_R profiles that strongly decrease outwards, probably due to the presence of disc-like structures that dominate the kinematics within 1–3 R_e and then fade.

(iv) The normalized V_{rms} profiles show that our sample galaxies fall into two main groups; the first group (NGC 1316, NGC 1344, NGC 1399, NGC 3384, NGC 4374, NGC 4406, NGC 5128 and NGC 5846) shows a slightly declining profile from the centre outwards and the second group (NGC 821, NGC 3377, NGC 3379, NGC 4494, NGC 4564 and NGC 4697) shows a strongly declining V_{rms} profile. An exceptional case is NGC 1023, where V_{rms} increases until $2.5R_e$, before falling steeply.

(v) The radial profiles of the velocity dispersion show a variety of shapes. There are nearly flat profiles, in which the velocity dispersion falls only by a few per cent from the central values; strongly

declining profiles, in which we observe a drop of a factor of 2 in the velocity dispersion towards outer radii; and a few anomalous galaxies, which exhibit rising profiles, again related to the presence of a stellar disc.

(vi) More luminous galaxies (brighter total B magnitude and X-ray luminosity) tend to have flatter $V_{\rm rms}$ and flatter velocity dispersion profiles and larger values of $V_{\rm rms}$ and dispersion measured at the outermost observed point. This is related to the fact that more massive galaxies have nearly flat dispersion profiles, and generally higher values for the outer velocity dispersion. Moreover, there is evidence that more massive and luminous galaxies have on average a lower number of PNe per unit luminosity (smaller α) than less massive galaxies.

(vii) Slow rotators have on average flatter $V_{\rm rms}$ and flatter velocity dispersion profiles and larger values of $V_{\rm rms,LAST}$ and $\sigma_{\rm LAST}$. Conversely, fast rotators have on average more steeply declining $V_{\rm rms}$ and velocity dispersion profiles, with lower values of $V_{\rm rms,LAST}$ and $\sigma_{\rm LAST}$.

(viii) Galaxies with high values of $\sigma_{\rm LAST}$ or nearly flat velocity dispersion profiles (i.e. more massive galaxies) are preferentially boxy in shape ($a_4 < 0$) and have smaller values of V/σ. Galaxies with small values of $\sigma_{\rm LAST}$ or declining velocity dispersion profiles (i.e. less massive galaxies) have a larger range of shapes ($-1 < a_4 < 2$) and V/σ ratios.

These results show that a full picture of the kinematics and angular momenta of elliptical galaxies requires information about their outer velocity fields. When comparing to models of the formation of ellipticals, it is important to take into account the halo kinematics – the dynamical time-scales in the haloes are longer and therefore the imprint of the formation mechanisms is preserved more strongly.

ACKNOWLEDGMENTS

We would like to thank Eric Emsellem for providing the $\lambda_{\rm R}$ radial profiles of the SAURON data, John Kormendy for providing surface photometry of NGC 4374 prior to publication and Karl Gebhardt for useful discussion.

The minor axis absorption-line kinematics of NGC 5846 are based on data from the SAURON archive.

This research has made use of the NED, which is operated by the Jet Propulsion Laboratory, California Institute of Technology, under a contract with the National Aeronautics and Space Administration.

PD was supported by the DFG Cluster of Excellence 'Origin and Structure of the Universe'. FDL was supported by the DFG Schwerpunktprogram SPP 1177 'Witnesses of Cosmic History'. MRM was supported by an STFC Senior Fellowship. NRN has been funded by CORDIS within FP6 with a Marie Curie European Reintegration Grant, contr. n. MERG-FP6-CT-2005-014774, co-funded by INAF. AJR was supported by the National Science Foundation Grant AST-0507729, and by the FONDAP centre for Astrophysics CONICYT 15010003.

REFERENCES

Abadi M. G., Navarro J. F., Steinmetz M., 2006, MNRAS, 365, 747
Arnaboldi M., Freeman K. C., Saha P., Capaccioli M., Ford H., Grillmair C., Hui X., 1994, BAAS, 26, 941
Arnaboldi M. et al., 1996, ApJ, 472, 145
Arnaboldi M., Freeman K. C., Gerhard O., Matthias M., Kudritzki R. P., Méndez R. H., Capaccioli M., Ford H., 1998, ApJ, 507, 759
Baldry I. K., Balogh M. L., Bower R. G., Glazebrook K., Nichol R. C., Bamford S. P., Budavari T., 2006, MNRAS, 373, 469
Barnes J. E., Hernquist L., 1996, ApJ, 471, 115
Bender R., 1988, A&A, 193, L7
Bender R., Doebereiner S., Moellenhoff C., 1988, A&AS, 74, 385
Bender R., Surma P., Doebereiner S., Moellenhoff C., Madejsky R., 1989, A&A, 217, 35
Bender R., Saglia R. P., Gerhard O. E., 1994, MNRAS, 269, 785
Bertola F., Pizzella A., Persic M., Salucci P., 1993, ApJ, 416, L45
Binney J., 2005, MNRAS, 363, 937
Binney J. J., Davies R. L., Illingworth G. D., 1990, ApJ, 361, 78
Blakeslee J. P., Lucey J. R., Barris B. J., Hudson M. J., Tonry J. L., 2001, MNRAS, 327, 1004
Bournaud F., Jog C. J., Combes F., 2005, A&A, 437, 69
Burkert A., Naab T., Johansson P. H., Jesseit R., 2008, ApJ, 685, 897
Buzzoni A., Arnaboldi M., Corradi R. L. M., 2006, MNRAS, 368, 877
Capaccioli M., Held E. V., Lorenz H., Vietri M., 1990, AJ, 99, 1813
Cappellari M., Emsellem E., 2004, PASP, 116, 138
Cappellari M. et al., 2006, MNRAS, 366, 1126
Cappellari M. et al., 2007, MNRAS, 379, 418
Cattaneo A., Dekel A., Devriendt J., Guiderdoni B., Blaizot J., 2006, MNRAS, 370, 1651
Ciardullo R., Jacoby G. H., Ford H. C., 1989a, ApJ, 344, 715
Ciardullo R., Jacoby G. H., Ford H. C., Neill J. D., 1989b, ApJ, 339, 53
Ciardullo R., Jacoby G. H., Dejonghe H. B., 1993, ApJ, 414, 454
Ciardullo R., Feldmeier J. J., Krelove K., Jacoby G. H., Gronwall C., 2002, ApJ, 566, 784
Ciotti L., Lanzoni B., Volonteri M., 2007, ApJ, 658, 65
Cox T. J., Dutta S. N., Di Matteo T., Hernquist L., Hopkins P. F., Robertson B., Springel V., 2006, ApJ, 650, 791
David L. P., Jones C., Forman W., Vargas I. M., Nulsen P., 2006, ApJ, 653, 207
De Lorenzi F., Debattista V. P., Gerhard O., Sambhus N., 2007, MNRAS, 376, 71
De Lorenzi F., Gerhard O., Saglia R. P., Sambhus N., Debattista V. P., Pannella M., Méndez R. H., 2008, MNRAS, 385, 1729
De Lorenzi F. et al., 2009, MNRAS, in press (arXiv:0804.3350)
de Vaucouleurs G., de Vaucouleurs A., Corwin Jr. H. G., Buta R. J., Paturel G., Fouque P., 1991, Third Reference Catalogue of Bright Galaxies. RC3, Springer-Verlag, New York
Debattista V. P., Corsini E. M., Aguerri J. A. L., 2002, MNRAS, 332, 65
Dejonghe H., de Bruyne V., Vauterin P., Zeilinger W. W., 1996, A&A, 306, 363
Dekel A., Stoehr F., Mamon G. A., Cox T. J., Novak G. S., Primack J. R., 2005, Nat, 437, 707
Douglas N. G. et al., 2002, PASP, 114, 1234
Douglas N. G. et al., 2007, ApJ, 664, 257
Emsellem E. et al., 2004, MNRAS, 352, 721
Emsellem E. et al., 2007, MNRAS, 379, 401
Faber S. M. et al., 2007, ApJ, 665, 265
Fisher D., 1997, AJ, 113, 950
Forestell A., Gebhardt K., 2008, ApJ, submitted (arXiv:0803.3626)
Freedman W. L. et al., 2001, ApJ, 553, 47
Gebhardt K. et al., 2000, AJ, 119, 1157
Gebhardt K. et al., 2003, ApJ, 583, 92
Gerhard O. E., 1993, MNRAS, 265, 213
Gerhard O., Kronawitter A., Saglia R. P., Bender R., 2001, AJ, 121, 1936
Goudfrooij P., Hansen L., Jorgensen H. E., Norgaard-Nielsen H. U., de Jong T., van den Hoek L. B., 1994, A&AS, 104, 179
Greggio L., Renzini A., 1990, ApJ, 364, 35
Halliday C., Davies R. L., Kuntschner H., Birkinshaw M., Bender R., Saglia R. P., Baggley G., 2001, MNRAS, 326, 473
Hao C. N., Mao S., Deng Z. G., Xia X. Y., Wu H., 2006, MNRAS, 370, 1339
Hargreaves J. C., Gilmore G., Irwin M. J., Carter D., 1994, MNRAS, 269, 957
Hui X., Ford H. C., Freeman K. C., Dopita M. A., 1995, ApJ, 449, 592
Ikebe Y. et al., 1996, Nat, 379, 427

Jacoby G. H., 1980, ApJS, 42, 1
Jacoby G. H., Ciardullo R., Ford H. C., 1990, ApJ, 356, 332
Jedrzejewski R. I., 1987, MNRAS, 226, 747
Jensen J. B., Tonry J. L., Barris B. J., Thompson R. I., Liu M. C., Rieke M. J., Ajhar E. A., Blakeslee J. P., 2003, ApJ, 583, 712
Jesseit R., Naab T., Peletier R. F., Burkert A., 2007, MNRAS, 376, 997
Kang X., van den Bosch F. C., Pasquali A., 2007, MNRAS, 381, 389
Kissler-Patig M., Brodie J. P., Schroder L. L., Forbes D. A., Grillmair C. J., Huchra J. P., 1998, AJ, 115, 105
Kormendy J., Bender R., 1996, ApJ, 464, L119
Kormendy J., Djorgovski S., 1989, ARA&A, 27, 235
Kormendy J., Fisher D. B., Cornell M. E., Bender R., 2009, ApJS, in press (arXiv:0810.1681)
Krajnović D. et al., 2008, MNRAS, 390, 93
Kronawitter A., Saglia R. P., Gerhard O., Bender R., 2000, A&AS, 144, 53
Lauer T. R. et al., 2005, AJ, 129, 2138
Magorrian J. et al., 1998, AJ, 115, 2285
Méndez R. H., Riffeser A., Kudritzki R.-P., Matthias M., Freeman K. C., Arnaboldi M., Capaccioli M., Gerhard O. E., 2001, ApJ, 563, 135
Méndez R. H., Teodorescu A. M., Kudritzki R.-P., 2008, ApJS, 175, 522
Merrett H. R. et al., 2006, MNRAS, 369, 120
Merritt D., 1993, ApJ, 413, 79
Moré J. J., Garbow B. S., Hillstrom K. E., 1980, User Guide for MINPACK-1 (Argonne Nat. Lab. Rep. ANL-80-74; Argonne: Argonne National Laboratory)
Naab T., Burkert A., 2003, ApJ, 597, 893
Naab T., Burkert A., Hernquist L., 1999, ApJ, 523, L133
Naab T., Jesseit R., Burkert A., 2006, MNRAS, 372, 839
Naab T., Johansson P. H., Ostriker J. P., Efstathiou G., 2007, ApJ, 658, 710
Napolitano N. R., Arnaboldi M., Freeman K. C., Capaccioli M., 2001, A&A, 377, 784
Napolitano N. R., Arnaboldi M., Capaccioli M., 2002, A&A, 383, 791
Napolitano N. R. et al., 2005, MNRAS, 357, 691
Napolitano N. R. et al., 2009, MNRAS, in press (arXiv:0810.1291)
Noordermeer E. et al., 2008, MNRAS, 384, 943
Oñorbe J., Domínguez-Tenreiro R., Sáiz A., Serna A., 2007, MNRAS, 376, 39
Oosterloo T. A., Morganti R., Sadler E. M., Vergani D., Caldwell N., 2002, AJ, 123, 729
O'Sullivan E., Forbes D. A., Ponman T. J., 2001, MNRAS, 328, 461
Peletier R. F., Davies R. L., Illingworth G. D., Davis L. E., Cawson M., 1990, AJ, 100, 1091
Peng E. W., Ford H. C., Freeman K. C., 2004, ApJ, 602, 685
Pinkney J. et al., 2003, ApJ, 596, 903
Rix H.-W., Carollo C. M., Freeman K., 1999, ApJ, 513, L25
Romanowsky A. J., Douglas N. G., Arnaboldi M., Kuijken K., Merrifield M. R., Napolitano N. R., Capaccioli M., Freeman K. C., 2003, Sci, 301, 1696
Romeo A. D., Napolitano N. R., Covone G., Sommer-Larsen J., Antonuccio-Delogu V., Capaccioli M., 2008, MNRAS, 389, 13
Saglia R. P., Kronawitter A., Gerhard O., Bender R., 2000, AJ, 119, 153
Sambhus N., Gerhard O., Méndez R. H., 2006, AJ, 131, 837
Samurović S., Danziger I. J., 2005, MNRAS, 363, 769
Sánchez-Blázquez P. et al., 2006, MNRAS, 371, 703
Scarlata C. et al., 2007, ApJS, 172, 494
Sikkema G., Carter D., Peletier R. F., Balcells M., Del Burgo C., Valentijn E. A., 2007, A&A, 467, 1011
Simien F., Prugniel P., 1997, A&AS, 126, 519
Sluis A. P. N., Williams T. B., 2006, AJ, 131, 2089
Statler T. S., Smecker-Hane T., 1999, AJ, 117, 839
Teodorescu A. M., Méndez R. H., Saglia R. P., Riffeser A., Kudritzki R.-P., Gerhard O. E., Kleyna J., 2005, ApJ, 635, 290
Thomas J., Saglia R. P., Bender R., Thomas D., Gebhardt K., Magorrian J., Corsini E. M., Wegner G., 2007, MNRAS, 382, 657
Tonry J. L., Dressler A., Blakeslee J. P., Ajhar E. A., Fletcher A. B., Luppino G. A., Metzger M. R., Moore C. B., 2001, ApJ, 546, 681
Tremblay B., Merritt D., Williams T. B., 1995, ApJ, 443, L5
Treu T. et al., 2005, ApJ, 633, 174
Valdes F., Gupta R., Rose J. A., Singh H. P., Bell D. J., 2004, ApJS, 152, 251
van der Marel R. P., 1991, MNRAS, 253, 710
van der Marel R. P., van Dokkum P. G., 2007, ApJ, 668, 756
van Dokkum P. G. et al., 2004, ApJ, 611, 703
Weijmans A.-M., Krajnović D., van de Ven G., Oosterloo T. A., Morganti R., de Zeeuw P. T., 2008, MNRAS, 383, 1343
Weil M. L., Hernquist L., 1996, ApJ, 460, 101
Woodley K. A., Harris W. E., Beasley M. A., Peng E. W., Bridges T. J., Forbes D. A., Harris G. L. H., 2007, AJ, 134, 494
Wyder T. K. et al., 2005, ApJ, 619, L15

APPENDIX A: TWO-DIMENSIONAL VELOCITY AND VELOCITY DISPERSION FIELDS OF GALAXIES IN SAMPLE B

Different authors adopted their own procedures and criteria to create smoothed two-dimensional fields of the PNe, depending on the amount of available data. Here, for a homogeneous analysis, we determine the two-dimensional velocity and velocity dispersion fields for some of these galaxies, adopting the procedure described in Section 4.2. We do this only for the galaxies with a sufficient number of PNe (>80), namely NGC 1023, NGC 1344, NGC 3379, NGC 4494, NGC 4697 and NGC 5128 (i.e. *sample B*). Parameters used in the kernel smoothing procedure and typical errors obtained with Monte Carlo simulations are listed in Table A1. Results are shown in Fig. A1.

Table A1. Typical parameters and errors for the smoothed two-dimensional velocity and velocity dispersion fields of the galaxies in *Sample B*.

Name	A	B (arcsec)	$\langle V \rangle$ (km s^{-1})	$\langle \Delta\sigma \rangle$ (km s^{-1})
(1)	(2)	(3)	(4)	(5)
NGC 1023	0.48	1.36	30	20
NGC 1344	0.53	−2.50	30	20
NGC 3379	0.57	14.92	30	30
NGC 4494	0.48	11.36	30	20
NGC 4697	0.40	12.80	40	20
NGC 5128	0.08	18.56	15	15

Notes. Cols 2–3: values of A and B used in the kernel smoothing procedure (see equation 4) as determined from the simulations. Cols 4–5: typical error on the two-dimensional velocity and velocity dispersion fields as determined from Monte Carlo simulations (see Section 4.3 for details).

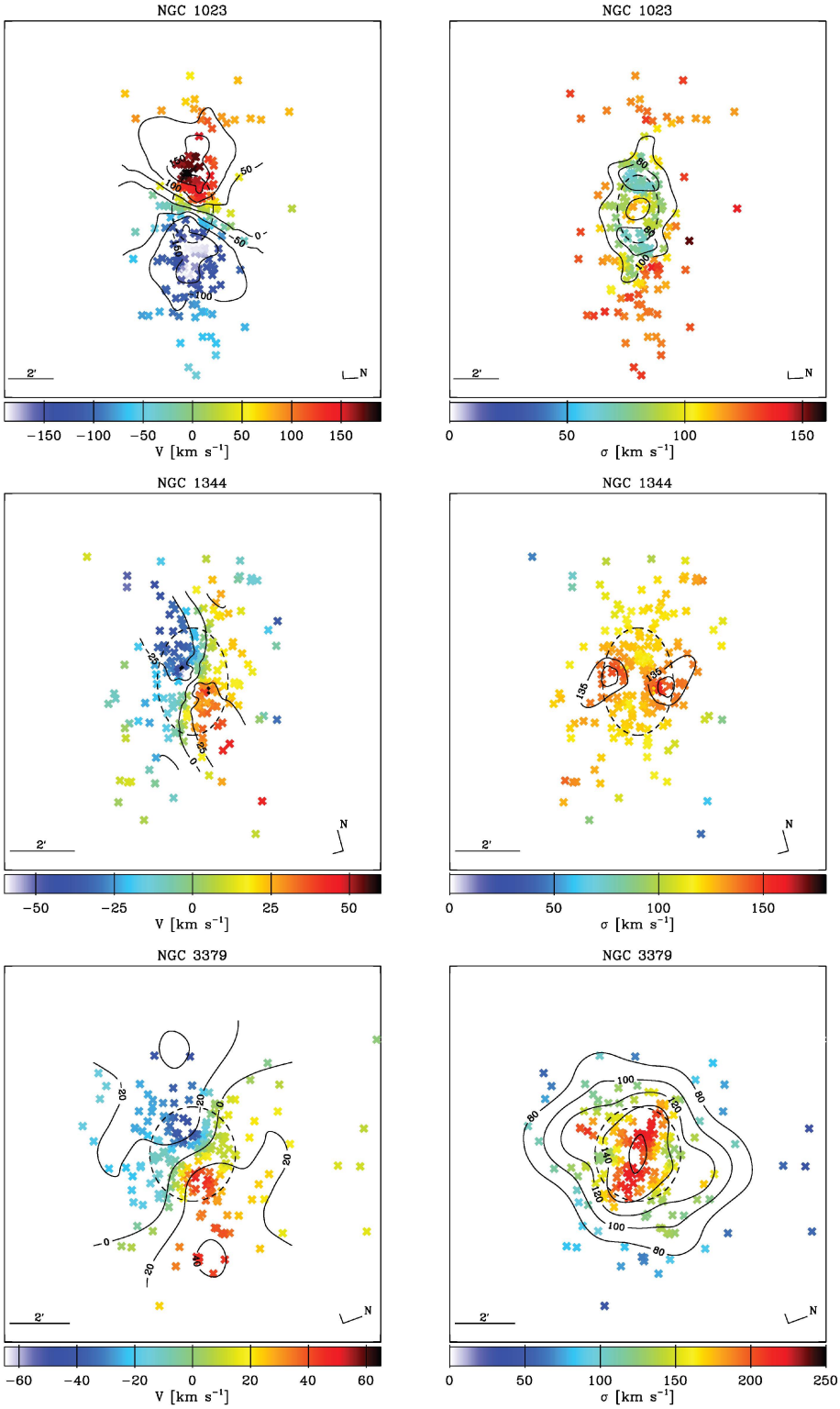

Figure A1. PNe-smoothed two-dimensional velocity and velocity dispersion fields for galaxies in *sample B*. Symbols, orientations and scales are as in Fig. 3.

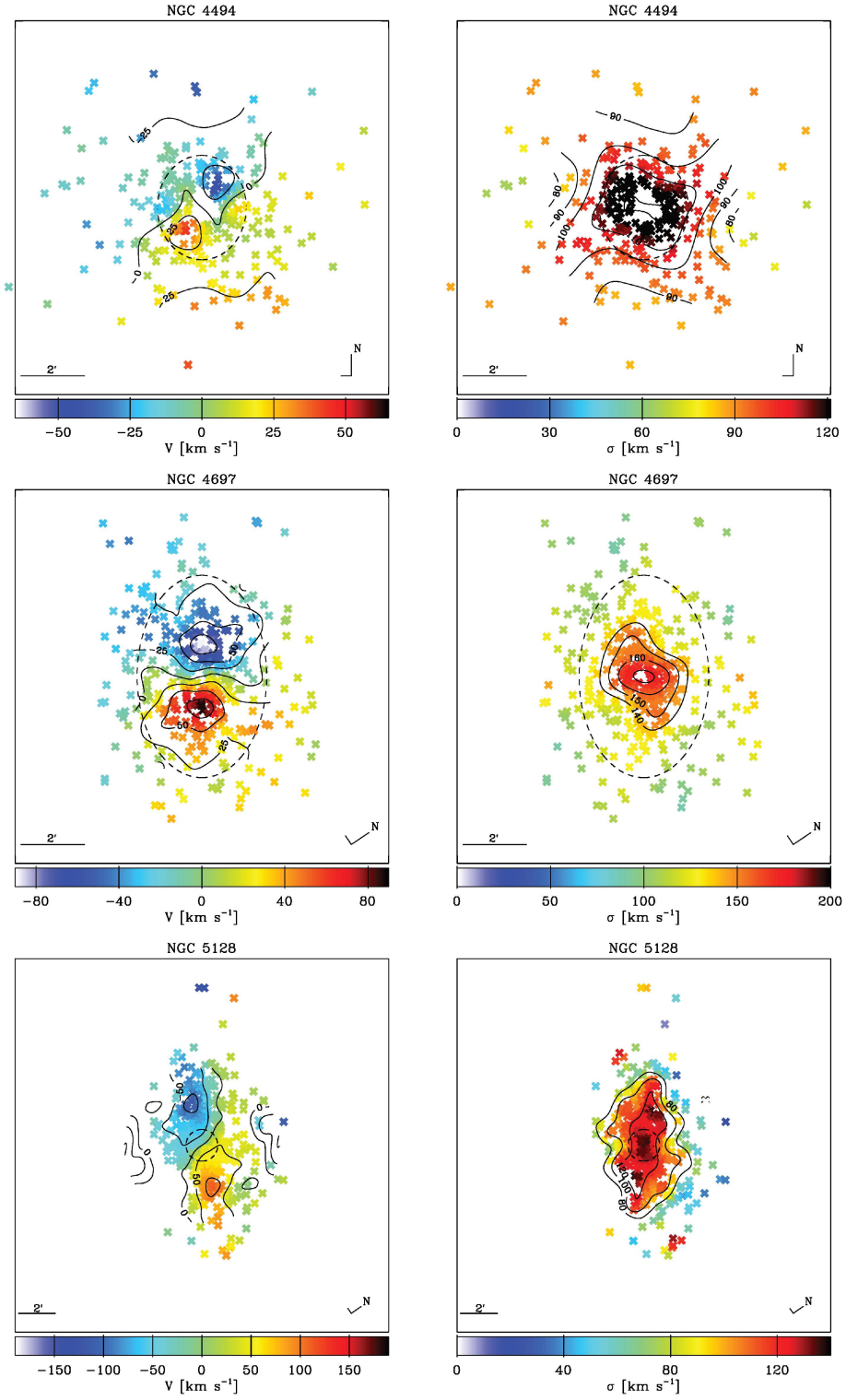

Figure A1 – *continued*

APPENDIX B: UNSMOOTHED VELOCITY FIELDS

The smoothing technique described in Section 4.2 is required to measure the mean velocity and the velocity dispersion along the line of sight of the PNe system. A single PN radial velocity measurement randomly deviates from the local mean velocity by an amount that depends on the local velocity dispersion. One can ask how the unsmoothed map of PNe radial velocity measurements compares with the smoothed two-dimensional velocity field.

In galaxies with high V/σ, we expect that the velocity map of individual PNe radial velocity measurements preserves the

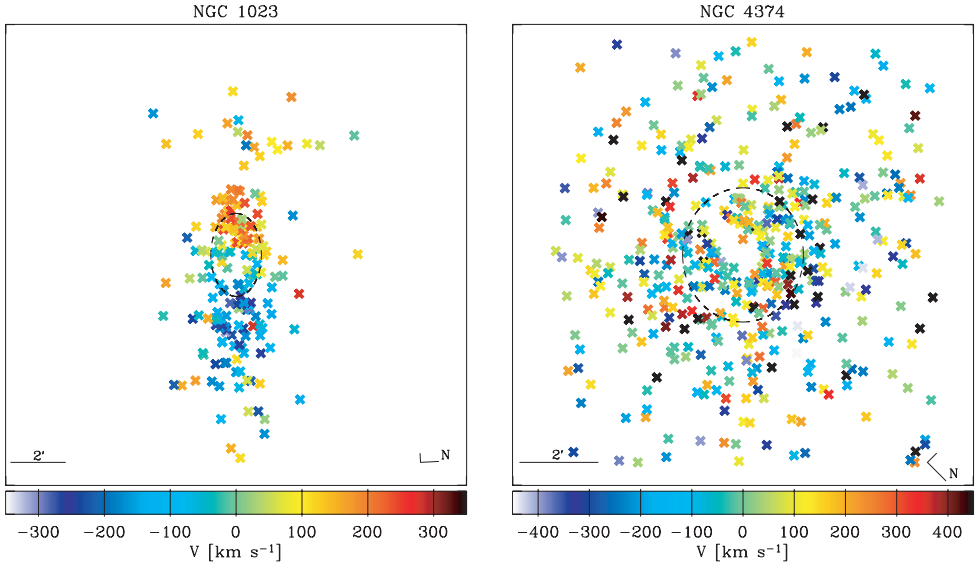

Figure B1. Two-dimensional velocity fields of the individual PNe radial velocity measurements for NGC 1023 (left-hand panel) and NGC 4374 (right-hand panel), without applying the adaptive kernel smoothing.

characteristics of the mean velocity field. On the contrary, in galaxies with low V/σ, we expect it to be chaotic and the mean rotation to be hidden in the scatter of the velocity dispersion, which dominates the kinematics. As examples, we show in Fig. B1 the two-dimensional maps of individual PNe radial velocities for NGC 1023 (a system dominated by rotation) and NGC 4374 (a system dominated by velocity dispersion).

APPENDIX C: LONG-SLIT KINEMATICS

Long-slit observations for NGC 3377, NGC 4374 and NGC 4494 were carried out with the VLT at the European Southern Observatory (ESO) in Paranal (Chile) from 2005 December to 2006 April (Proposal 76.B–0788A) in service mode under dark time conditions. The Unit Telescope 1 (Antu) was mounted with the FORS2,

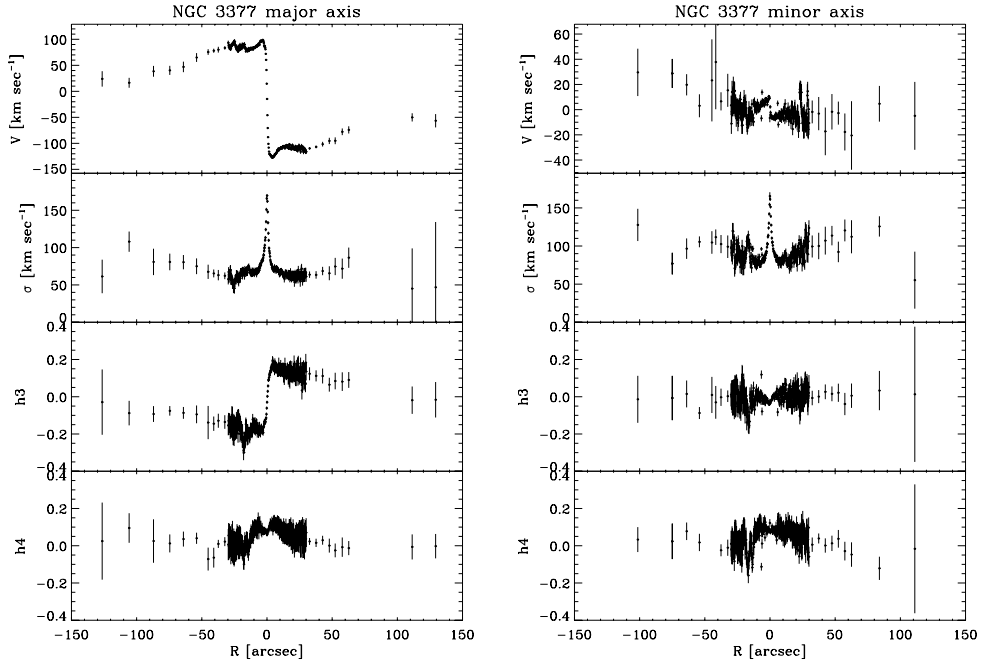

Figure C1. Radial velocities, velocity dispersions, h_3 and h_4 coefficients for NGC 3377 along the major and minor axes.

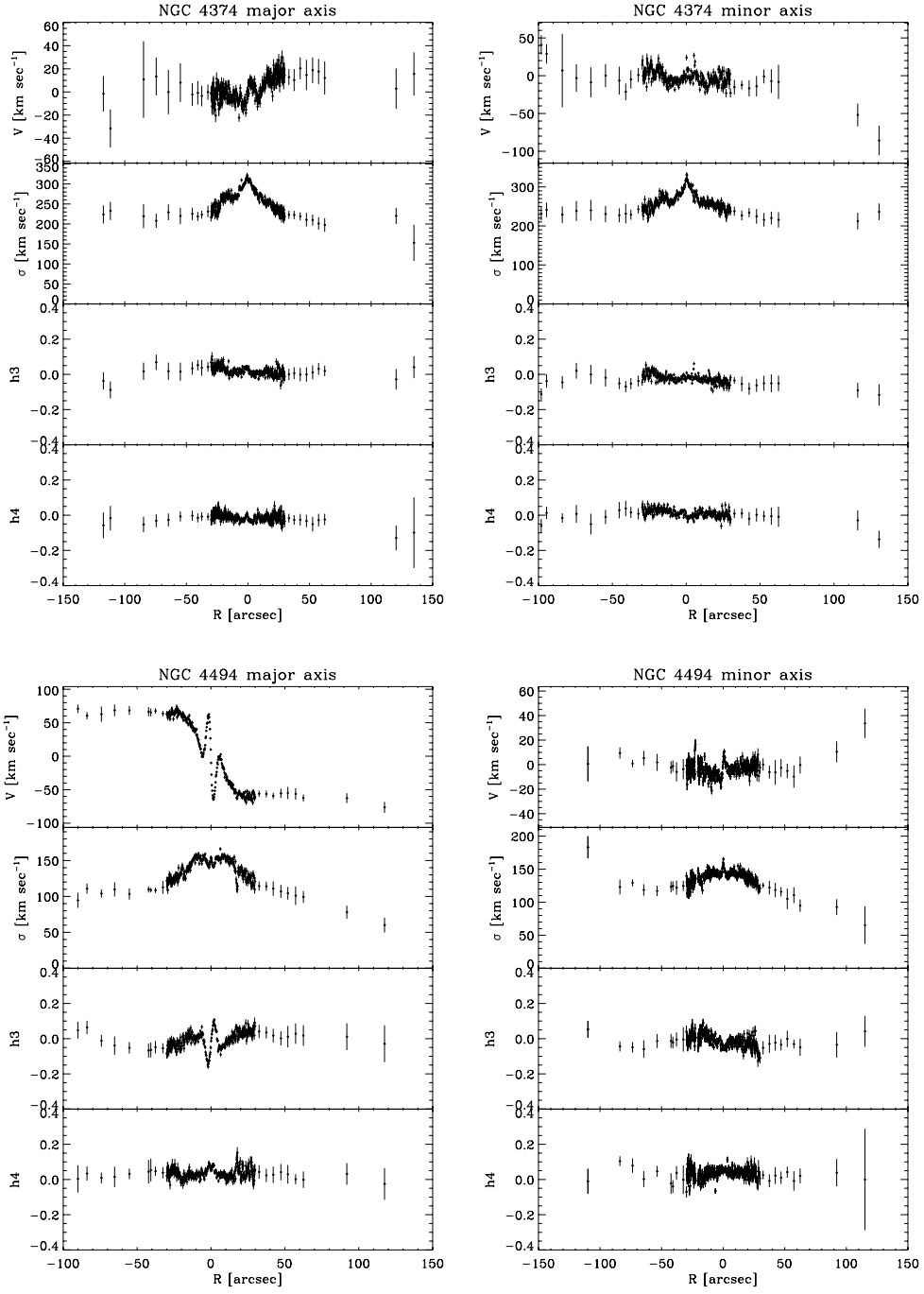

Figure C1 – *continued*

which was equipped with the 1400 V Grism and the 0.5 arcsec slit. Spectra were taken along both the major and minor axes. Basic data reduction was performed using standard ESO-MIDAS[6] and IRAF[7] routines. All the spectra were bias-subtracted, flat-field corrected by quartz lamp and twilight exposures, cleaned of cosmic rays, and wavelength calibrated. After calibration, the different spectra obtained for a given galaxy along the same position angle were co-added using the centre of the stellar-continuum radial profile as a reference. The contribution of the sky was determined at the two edges of the resulting frames where the galaxy light was negligible, and then subtracted. Spectra from adjacent rows had been binned together in order to ensure a signal-to-noise ratio of at least 25. The instrumental FWHM measured on the comparison spectra is $\approx$140 km s^{-1}.

The stellar kinematics (mean velocity, velocity dispersion, h_3 and h_4 Gauss–Hermite coefficients) were measured by means of the Penalized Pixel-Fitting method by Cappellari & Emsellem (2004); kinematic stellar templates were chosen from the Indo–US Coudé Feed Spectral Library (Valdes et al. 2004) and the MILES library

[6] MIDAS is developed and maintained by the ESO.

[7] IRAF is distributed by NOAO, which is operated by AURA, Inc., under contract with the National Science Foundation.

Table C1. Stellar kinematics for three sample galaxies.

Name (NGC) (1)	*PA* (◦) (2)	R (arcsec) (3)	V (km s^{-1}) (4)	V (km s^{-1}) (5)	$\sigma\Delta$ (km s^{-1}) (6)	σ (km s^{-1}) (7)	h_3 (8)	h_3 (9)	h_4 (10)	h_4 (11)
3377	35	−126.42	23.9	14.8	61.3	22.5	−0.029	0.175	0.025	0.207
3377	35	−105.75	16.4	9.6	108.0	13.6	−0.088	0.066	0.095	0.079
3377	35	−87.04	38.5	10.4	80.8	17.7	−0.093	0.043	0.025	0.117
3377	35	−74.55	40.3	8.8	80.8	11.2	−0.076	0.026	0.012	0.048
3377	35	−64.10	46.9	10.1	80.5	9.6	−0.087	0.032	0.036	0.040
3377	35	−54.00	65.0	8.5	75.0	10.6	−0.095	0.048	0.040	0.030
3377	35	−45.16	75.5	5.5	67.6	9.5	−0.139	0.089	−0.072	0.061
3377	35	−40.84	78.1	3.9	65.4	5.3	−0.145	0.039	−0.064	0.053
3377	35	−37.34	80.1	5.6	63.1	6.9	−0.129	0.038	0.010	0.022
..										
4374	45	130.47	−85.7	19.6	236.2	21.2	−0.116	0.061	−0.137	0.049

Notes. This is a sample: the complete table is published as Supporting Information in the online version of this article. Col. 1: NGC galaxy number. Col. 2: slit position angle. Col. 3: distance from the galaxy centre measured along the slit. Col. 4: radial velocity. Col. 5: error on radial velocity. Col. 6: velocity dispersion. Col. 7: error on velocity dispersion. Col. 8: h_3 Gaussian–Hermite coefficient. Col. 9: error on h_3 Col. 10: h_4 Gaussian–Hermite coefficient. Col. 11: error on h_4.

(Sánchez-Blázquez et al. 2006), and then convolved with a Gaussian function to match the instrumental FWHM. Spectral regions with known emission lines (Hβ, [O III]) were masked and not included in the fit.

In Fig. C1, we show the measured long-slit kinematics. Table C1 contains the measured absorption-line kinematics. The entire version of Table C1 is available as Supporting Information in the online version of this article.

APPENDIX D: ROTATION AND ANGULAR MOMENTUM CONSIDERATIONS

Since the angular momentum of a star is weighted by its galactocentric radius, the outer regions of a galaxy are particularly important for estimating the total angular momentum. One cannot in general observe the three-dimensional positions and velocities necessary to calculate the full angular momentum, so we will use a two-dimensional projected proxy. This proxy angular momentum can be simplified to a one-dimensional problem by adopting the approximation that the rotation is aligned with the photometric major axis, and its azimuthal dependence is related to the major-axis velocity by $V(\phi) = V_{\rm max}\cos(\phi)$ (cf. Krajnović et al. 2008).

The cumulative proxy angular momentum inside a radius R is then

$$LP(R) = \pi \int_0^R V_{\rm max}(R')\Sigma(R')R'^2 {\rm d}R', \quad \text{(D1)}$$

where the stellar surface density is $\Sigma(R)$. With the simplest assumptions that the galaxy light follows the $R^{1/4}$ law, and that the rotation velocity $V_{\rm max}$ and the stellar mass-to-light ratio are both constant with radius, one can calculate that 9 per cent of the total proxy angular momentum resides inside $R_{\rm e}$, and 50 per cent inside $5.4\,R_{\rm e}$. The latter 'angular momentum effective radius' ($\equiv R_{LP}$) is naturally larger if $V_{\rm max}$ increases with R or if the galaxy light is more extended (e.g. $R_{LP} = 12.1\ R_{\rm e}$ for the Sérsic index $n = 6$). It is smaller if $V_{\rm max}$ decreases or if the light is more compact (e.g. $R_{LP} = 2.4R_{\rm e}$ for $n = 2$).

These calculations show that probing well outside $R_{\rm e}$ is essential for characterizing the angular momentum of an elliptical galaxy. The dimensionless cumulative angular momentum-like parameter $\lambda_{\rm R}$ introduced by Emsellem et al. (2007) can also be shown to have the same limitation, so that the global angular momentum requires measurements to $\gtrsim 5\ R_{\rm e}$.

An alternative approach is to consider the radius of gyration, $R_{\rm g}$, as the rule-of-thumb target radius for measuring the angular momentum. $R_{\rm g}$ is defined as the radius where a point mass would have the same specific moment of inertia as the extended mass profile. Using the formula

$$R_{\rm g} \equiv \sqrt{\frac{I}{M}} = \left[\frac{\int_0^\infty \Sigma(R)R^3{\rm d}R}{\int_0^\infty \Sigma(R)R{\rm d}R\Delta}\right]^{1/2}, \quad \text{(D2)}$$

we find very similar radii to the R_{LP} calculations reported above, e.g., $R_{\rm g} = 2.1R_{\rm e}$, $4.7R_{\rm e}$, $10.1R_{\rm e}$ for Sérsic $n = 2$, 4, 6.

SUPPORTING INFORMATION

Additional Supporting Information may be found in the online version of this article:

Table 2. PNe catalogue for galaxies in *Sample A*.
Table 6. Kinematic data used in Fig. 7.
Table C1. Stellar kinematics for three sample galaxies.

Please note: Wiley-Blackwell are not responsible for the content or functionality of any supporting materials supplied by the authors. Any queries (other than missing material) should be directed to the corresponding author for the article.

This paper has been typeset from a TEX/LATEX file prepared by the author.